Simulating Microwave Morphology Dependent Resonances in Aqueous Dimers and Trimers

A Thesis Submitted to the Committee of Graduate Studies in Partial Fulfillment of the Requirements of the Degree of

Master of Science

in the Faculty of Arts and Science

TRENT UNIVERSITY

Peterborough, Ontario, Canada

Shima Nikkhah Fini

Materials Science M.Sc. Graduate Program

January 2024

Abstract

Simulating Microwave Morphology Dependent Resonances in Aqueous Dimers and Trimers

Shima Nikkhah Fini

Microwave resonances in isolated water-based spheres, dimers, and trimers are explored using simulations conducted with COMSOL Multiphysics. The study centers on morphology-dependent resonances (MDRs) and hotspot characteristics in cm-sized objects at microwave frequencies. Monomers subjected to microwave radiation exhibit four distinct resonant modes at specific sizes characterized by electric and magnetic field distributions which correspond to magnetic-dipolar, electric-dipolar, magnetic quadrupolar, and electric quadrupolar resonances, respectively. Dimer configurations reveal intriguing hotspot features, with axial hotspots emerging as a key resonant characteristic. The three fundamental dimer orientations dictate unique resonant behaviors, highlighting the sensitivity of hotspot intensity to orientation changes, but smooth and consistent trends during transitions between them. Investigations into trimer structures, as a more intricate geometry formed by interconnected dimers, reveal the subtle interactions of spheres in a trimer structure. Trimer hotspots largely reflect the sum of isolated dimer hotspot contributions, showcasing the energy conservation with no evidence of a newly formed hotpot. Our results, while arising as a consequence of the particularly high index of refraction of water at GHz frequencies, are generalizable to other length scales (such as nano-photonics), were materials with sufficiently high refractive index and transparency to be found.

Keywords: Microwave frequencies, Morphology-dependent resonance, COMSOL simulations, Electromagnetic physics, water-based objects.

Acknowledgements

I am deeply grateful to all those who have supported and guided me throughout my journey in the Materials Science program at Trent University. First and foremost, I would like to express my sincere gratitude to my supervisor, Dr. Aaron Slepkov. His expertise, guidance, and support have been instrumental in shaping the direction of my research. His insightful feedback and encouragement have consistently pushed me to strive for excellence.

I extend my heartfelt appreciation to the Materials Science program at Trent University for providing me with an enriching academic environment. The support I received has been invaluable in allowing me to focus on my research and academic pursuits.

I would like to extend a special thank you to my labmate, Yuchen Song, for his dedicated assistance throughout my research. His willingness to share his knowledge, collaborate, and offer guidance has been beneficial to my progress. I am also indebted to my family and friends for their unwavering encouragement, understanding, and support during the ups and downs of this academic journey. I am deeply thankful to everyone who has played a role in my academic and research endeavors.

Table of Contents

List of Figures

List of Abbreviations

AxTr	Axial Transverse
BC	Boundary condition
ED	Electric dipole
EM	Electromagnetic
EQ	Electric quadrupole
FDTD	Finite Difference Time Domain
FEM	Finite element method
MDR	Morphology-dependent resonance
MD	Magnetic dipole
MQ	Magnetic quadrupole
PDEs	Partial differential equations
PEC	Perfect electric conductor
PMC	Perfect magnetic conductor
SPP	Surface plasmon polariton
SPR	Surface plasmon resonance
RF	Radio Frequency
SBC	Scattering Boundary Condition
TrAx	Transverse Axial
TrTr	Transverse Transverse
WGM	Whispering gallery mode

Chapter 1: Introduction

1-A) Motivation of this study

Prior to my work, our research group has studied microwave resonances in single spheres of water theoretically using Mie scattering theory, computationally using COMSOL, and experimentally with grapes and other water-rich spheres, using a common household microwave oven [1]. The reason we chose water as a material for study is its response to electromagnetic radiations. Water acts like a resonator for microwave light because water has a high index of refraction at microwave frequencies. The index of refraction, $\tilde{n}$, quantifies how much slower light travels in the medium compared to its speed in a vacuum. It is related to the permittivity of water, denoted as $\tilde{\varepsilon}$ through the relationship [2]

$$\tilde{n} = \sqrt{\tilde{\varepsilon}}\,;\ \tilde{n}^2 = (n + iK)^2 = \tilde{\varepsilon} = (\varepsilon_1 + i\varepsilon_2). \quad (1)$$

In this equation, n represents the real part of the complex index of refraction, while K is the imaginary part. n affects the phase velocity of light in water, and K is responsible for the absorption of electromagnetic waves in the medium. When light passes through a material like water, its speed is reduced by a factor of n, as compared to its speed in a vacuum. This reduction in speed affects the wavelength of the light in the medium. The wavelength in water, λ, is related to the wavelength in a vacuum, λ_0, through [2]

$$\lambda = \lambda_0/n. \quad (2)$$

The imaginary part, K, plays a crucial role in understanding the absorption of light by water. It is linked to the absorption coefficient, often denoted by α, which describes the

extent to which the material absorbs light of a specific wavelength. In the case of Beer's Law, the absorption coefficient α is simply $2K$ [2].

Water, however, is unremarkable optically in the visible regime, and so our lab is not particularly interested in nano-scale aqueous objects. Instead, because of water's high index at GHz frequencies, our lab is interested in the microwave resonances that happen in water-based cm-sized objects, and I explain the experimental results in grapes by modeling them as balls of water. A significant observation we made during our experiments is the occurrence of sparks between two touching grapes placed in a microwave oven. This intriguing phenomenon does not occur when only a single grape is irradiated. Because we are interested in grapes as balls of water, we also experimentally study and simulate hydrogel beads (made of sodium polyacrylate) as better models for water spheres [1].

Understanding the factors behind this spark formation is crucial as it relates to the formation of hotspots in hydrogel dimers. Near-field hotspots in plasmonic systems (i.e., in metals) have been an active area of research and technology, and we are interested in exploring similar effects in dielectric systems. Investigating the underlying mechanisms behind dimer hotspots is of paramount importance in this effort because it offers valuable insights into the generation of sub-wavelength electromagnetic field concentrations. These excitations can confine and manipulate light at the nanoscale, leading to enhanced light-matter interactions and the generation of localized electromagnetic fields, often referred to as hotspots [3]. These hotspots open possibilities for various applications, including highly specific sensing like low/single molecule detection or advanced spectroscopy and efficient energy conversion [4].

This study explores a novel approach using water-based spheres with the appropriate sizes and high refractive index to concentrate electromagnetic energy into a minuscule focal spot situated between them. Remarkably, this geometry yields sub-millimeter (and sub-wavelength) focusing capabilities despite employing radiation with a relatively long wavelength of around 12 cm. So, if similar focusing could be achieved with visible light, it could provide significant improvements for example over current lithography technique (as the fabrication of microchips faces a major challenge in achieving extremely small feature sizes using lithography techniques [5] This advancement has the potential to revolutionize microchip fabrication by enabling precise writing at a small scale, thereby significantly facilitating the manufacturing process [5]. These hotspots created by focusing electromagnetic energy between spheres hold promise for various applications beyond lithography. One significant application is single molecule detection, where the highly-localized electromagnetic field can enhance the interaction between light and individual molecules. This enables sensitive detection and analysis of molecular processes, such as studying biomolecular interactions, monitoring chemical reactions, or investigating the behavior of nanoparticles at the single-molecule level [6].

Furthermore, the ability to achieve sub-wavelength focusing using these hotspots opens opportunities for near-field super-resolution imaging [7]. Near-field techniques surpass the diffraction limit of conventional optical microscopy, enabling imaging with resolutions beyond what is conventionally achievable. By utilizing the highly confined electromagnetic fields in hotspots, it becomes possible to visualize and characterize nanostructures, biological samples, and materials with unprecedented detail [8].

However, water in microwave regime has high refractive (index of refraction of water is 9.5 at 2.45 GHz) and there is currently a need for an equivalent high-index material in the visible regime. Ultimately, however, our interest in dimer and cluster hotspots is most immediately motivated by a desire to better understand why grape dimers spark in the microwave oven, and to extend that understanding to other geometries like trimer and weather it has a novel hotspot.

1-B) Thesis Outline

In Chapter 2, titled "Background," the fundamental principles governing the resonant behavior of water spheres in microwave radiations are discussed. This chapter explores Mie scattering and morphology-dependent resonances (MDRs), dielectric properties of water at microwave frequencies, microwave absorption mechanisms in water, and their temperature dependencies. Additionally, it delves into the unique characteristics of MDRs, compares them with surface plasmon resonances (SPRs) in metals, and provides insights into theoretical models and experimental studies related to MDRs, laying the groundwork for the subsequent research in the thesis.

Chapter 3, titled "Methodology," outlines the computational methods employed for investigating morphology-dependent resonances in simulated aqueous beads at microwave frequencies. The chapter details the use of COMSOL Multiphysics for finite element method simulations, encompassing steps such as model setup, meshing, solving electromagnetic field equations, and postprocessing data. It also provides insights into the simulation settings, including boundary conditions, material properties, meshing, model equations, and output data analysis, all crucial components for understanding the subsequent research in the thesis.

Chapter 4, as “Results and Discussion” starts with exploration of the behavior of aqueous spheres as monomers and I study morphology-dependent resonances in monomers in this chapter. It also delves into the unique electromagnetic phenomena and hotspots that arise in dimer configurations, emphasizing orientation-dependent variations in resonant behavior. A main focus of this chapter is to investigate the progression of MDRs in aqueous spheres, compare the resonant modes between monomers and dimers, and explore the emergence and intensity of hotspots in different dimer orientations.

Chapter 4-C focuses on investigating intermediate dimer orientations between fundamental dimers and exploring the emergence and intensity of hotspots during these transitions. The chapter systematically examines how the internal resonances and hotspot strengths evolve as dimers shift from one orientation to another, contributing to a deeper understanding of the principles governing these geometries. Furthermore, in chapter 4-D, I delve into the study of trimers as clusters of dimers, aiming to determine whether trimers exhibit unique hotspot characteristics and exploring their resonant behaviors. The chapter compares trimers to the combined properties of their constituent dimers, shedding light on the interactions and energy conservation within trimer systems.

Finally, In the Summary chapter of my thesis, I provide a comprehensive summary of the main approach and findings of this research, following with insights into potential future research directions, which include experimental free-space irradiation, cluster geometries, the dimerization processes, and potential temperature dynamics of these resonances.

Chapter 2: Background

2-A) Resonant behavior of water spheres in microwave radiations

The phenomenon of microwave resonances can be understood through the principles of Mie scattering and morphology-dependent resonances (MDRs) [9]. Mie scattering describes the interaction of electromagnetic waves with spherical particles, occurring when the particle size is comparable to the wavelength of the incident radiation. As the size of the sphere approaches the characteristic wavelength, specific resonant modes arise, leading to enhanced scattering and absorption phenomena [9].

Bohren and Huffman [9] provides theoretical explanations and mathematical formulas that describe the absorption and scattering properties of small particles, enabling the prediction of resonance frequencies and resonant modes for water spheres. By applying these formulas to the specific size and refractive index properties of water spheres, we can identify the resonant sizes and shapes contributing to the observed microwave resonant behavior.

The mode shapes of spherical particles including water-based spheres, are determined by solving the Mie scattering equations, resulting in different multipole modes, such as electric dipole, magnetic dipole, electric quadrupole, magnetic quadrupole [9]. Each mode shape corresponds to a specific angular distribution of the electric and magnetic fields within and around the particle [10].

2-A-1) Dielectric properties of water at microwave frequencies

Understanding the dielectric properties of water at microwave frequencies is crucial for explaining the behavior of objects under microwave irradiation. The dielectric properties

of water are primarily characterized by the complex permittivity $\tilde{\varepsilon} = (\varepsilon_1 + i\varepsilon_2)$. consisting of the dielectric constant (ε_1) and dielectric loss factor (ε_2). The dielectric constant represents the ability of the material to store electric energy, while the dielectric loss factor describes the ability to convert microwave energy to thermal energy [11]. The dielectric loss factor of water, related to energy dissipation through molecular rotation and dipolar relaxation processes, contributes to the overall behavior of water under microwave irradiation [12].

At this point, we need to know that the relative complex permittivity of water at the frequency of 2.5 GHz is $\tilde{\varepsilon} = (\varepsilon_1 + i\varepsilon_2) = 80 + i9.5$ at the room temperature (temperature of 20°C). So, the relative refractive index of water at this temperature is $\tilde{n} = n + iK = 9 + i0.6$ [13]. However, In the visible regime, there is currently no nm-visible analogue to water in microwave regime due to its high refractive property at microwave frequencies (refractive index of water is ~9 at 2.45 GHz). The highest known refractive index for dielectric materials at visible wavelengths is typically around 2.4 to 2.6. However, it's worth noting that in the mid-infrared range, materials with significantly higher refractive indices, reaching values as high as 6 or more, have been reported [14]. It is also worth noting that there are some exotic materials and structures, such as metamaterials and photonic crystals, that can exhibit higher refractive indices through engineered designs [15].

Several studies have investigated the influence of temperature on the dielectric properties of water and ice at microwave frequencies. Catenaccio *et al.* [16] studied the temperature dependence and observed that the dielectric constant of water decreases with increasing temperature, while the loss factor remains relatively constant. Matzler *et al*. [17] explored

the complex permittivity of water and ice, finding that the dielectric constant of ice is significantly lower than that of liquid water at the same frequency and temperature and the loss factor of ice is considerably higher than that of water, indicating increased absorption of microwave energy. Understanding these differences in the complex permittivity between water and ice contributes to the analysis of microwave interactions with real water-based materials in different phases.

2-A-2) Microwave absorption of water

Water's high dielectric constant (80) and loss factor (9.5) result in strong interactions with microwave radiation, leading to an interesting absorption and energy dissipation [12]. Understanding these properties of water enables us to comprehend phenomena such as microwave heating, where water molecules absorb microwave energy, resulting in heat generation [18]. Water as an electrically dipolar molecule, plays a crucial role in absorbing microwaves. The absorption process involves dipolar rotation of water molecules, where the alternating electric field of the microwave radiation causes the water molecules to align with the field and continuously rotate, leading to energy absorption and subsequent 'frictional' conversion into heat [19]. At low frequencies, the dipoles align easily with the electric field, while at higher frequencies, molecular interactions cause a phase lag between the dipoles and the field, resulting in greater dielectric loss and power absorption [13].

Studies by Yonas A., *et al.* [12] and Yin, Y. *et al.* [20] provided insights into the absorption mechanisms in water-based objects and the influence of factors such as temperature, frequency, and chemical composition on the absorption behavior. For example, The dielectric constant of purified water decreased from 78 to 52 when the temperature increased from 23°C to 100°C at the frequency of 2450 MHz (the complex permittivity of

water is 52.0 + 0.1 at 100 °C, while it is 78.0 + 0.01 at 23°C) [12].The absorption behavior is temperature-dependent, with decreasing dielectric constant and increasing absorption coefficient at higher temperatures [13].

2-B) Morphology-dependent resonances (MDRs)

Morphology-dependent resonances represent a fascinating phenomenon observed in various systems, particularly it is common in the study of nano-scale dielectric objects that are resonant in visible wavelengths. MDRs are resonances characterized by resonant peaks in the scattering spectrum, which are highly sensitive to the size, shape, and dielectric properties of the object [21]. When an incident wave interacts with the object, it undergoes multiple reflections and refractions, leading to constructive interference at specific wavelengths, thus generating peaks in the scattering spectrum and enhanced field confinement and energy localization [21]. The study of MDRs has gained significant attention in various fields, including optics, material science, and biomedical engineering, owing to their potential applications in sensing, imaging, and particle manipulation [22]. Eversole *et al.* [23] studied Morphology-Dependent Resonances in microdroplets. They focused on identifying the resonance frequencies, which provided insights into the behavior of light in the droplets. By analyzing these positions, the researchers gained information about the refractive index and observed differences in resonance positions for different modes.

The exact process of MDR formation relies on the geometric characteristics, material composition, and incident wavelength, which determine the resonant behavior [24]. For example, Vannes and Preston [25] explored non-spherical core-shell particles and investigated the influence of geometric characteristics and material composition on MDRs.

By investigating the resonant behavior of these particles, their work highlighted the existence of the internal field within the particles. Similarly, Rahman *et al.* [26] investigated a novel optical sensor based on whispering gallery mode (WGM) resonances (a subset of MDRs in this case) for measuring thermal deformation in some devices. They characterized the behavior of large-size-parameter microspheres in optical wavelengths theoretically and experimentally. They demonstrated that the geometric structure and material composition of the microspheres, along with the incident temperature changes, play crucial roles in determining the resonant behavior and efficiency of the WGM resonances.

2-B-1) Comparison of surface plasmon resonances and MDRs

MDRs in transparent dielectrics are analogues of surface plasmon resonances (SPRs) in metals. MDRs arise due to the interference of multiple scattering paths within an object, resulting in enhanced field confinement and energy localization [21]. One key difference between MDRs in dielectrics and plasmons in metals is the presence of internal modes in dielectric materials. While both SPRs and MDRs, as two optical phenomena, exhibit intense sub-wavelength field confinement, it is essential to note their distinct characteristics, particularly concerning internal electromagnetic (EM) modes [27].

Work by Deviliz *et al.* [3] demonstrates the equivalence between metallic particles hosting localized surface plasmons and MDRs in dielectric particles, in terms of their electromagnetic responses. They show that the electromagnetic fields scattered by metallic particles can be accurately reproduced by dielectric particles of very high refractive index, of order n~10. By deriving analytic formulas that relate the permittivity of the dielectric

and metallic particles, they establish an equivalence that yields identical dipolar electromagnetic responses. This finding enables the use of well-known dipolar models to predict the resonances of dielectric particles, which offers valuable insights into the comparison between surface plasmon resonances and MDRs in dielectrics.

While SPRs in metals have been extensively studied for their surface-confined fields-enhancements, the absence of internal modes differentiates them from MDRs in dielectric materials. When considering SPRs in metals, the absence of internal modes can be attributed to the nature of dielectric and metallic materials [28]. Metals have a high electrical conductivity, which leads to the rapid dissipation of EM fields within the material. Consequently, metals primarily exhibit surface plasmon polaritons (SPPs) resulting in the intense field enhancements near the surface but no significant internal field concentration [28]. In contrast, Dielectric materials possess a low electrical conductivity and a high permittivity, which allow for strong electric field confinement within the material volume [23]. This leads to the formation of internal EM modes that are trapped and confined within the dielectric structure. This different behavior causes MDRs exhibit rich spatial features and particular shapes within the objects, rather than being primarily confined to the surface [25].

2-B-2) Theoretical models and previous experimental studies

In the exploration of MDRs, some theoretical models and experimental studies have been conducted to deepen our understanding of these resonances. One commonly used approach is the Mie theory, which provides a mathematical framework to describe the interaction of electromagnetic waves with spherical particles [9]. Mie theory enables the calculation of scattering and absorption properties of particles as a function of their size, shape, and

refractive index. By applying Mie theory to aqueous objects, researchers can analyze the resonant behavior and predict the specific resonant frequencies and field distributions [9].

As an example, Mishchenko and Lacis [29] studied MDRs in nearly spherical particles, with an emphasis on the Mie theory. Their investigation aimed to understand the behavior of MDRs in particles with increasing sphericity by analyzing various particle shapes, including prolate and oblate spheroids. By applying the principles of the Mie theory, they found that even a slight deviation from a perfect sphere significantly alters the super narrow MDRs. These findings provide valuable insights into the influence of particle morphology on MDRs within the framework of the Mie theory. For example, grapes that we experimentally studied them in a microwave oven are not perfectly spherical; so, based on Mishchenko and Lacis, the best choice for our simulation models is to model perfect spheres.

In addition to Mie theory, several computational tools, such as the Finite Element Method (FEM) and the Finite Difference Time Domain (FDTD) method, have been used to study morphology-dependent resonances in more complex geometries to address the complexities of analyzing resonance phenomena in geometries beyond simple spheres [30,31]. Analytical methods like the multipole expansion approach, such as Mie theory, can be particularly challenging to apply to intricate structures due to their limitations in handling irregular shapes because it relies on assumptions of symmetry and homogeneity, making it well-suited for simple geometries like spheres [30,31]. This limitation naturally leads to the adoption of advanced computational techniques such as FEM and FDTD methods. These methods offer powerful tools for numerically simulating electromagnetic fields in objects with irregular shapes, allowing for a deeper understanding of resonance

modes and field distributions within the objects. The FDTD method is a computational technique widely used in electromagnetics. It discretizes space and time into a grid and solves Maxwell's equations iteratively, allowing for the simulation of electromagnetic field propagation and interactions with complex objects as well as prediction of the resonant behavior, field localization, and scattering properties of complex morphologies [30]. Similarly, FEM offers a versatile numerical technique for solving partial differential equations by subdividing the object into smaller elements. This method allows for a detailed analysis of resonance modes and field distributions within objects and has been extensively used for studying electromagnetic phenomena, including MDRs in complex geometries [31]. The combination of these theoretical models, including Mie theory, FDTD, and FEM, facilitates comprehensive investigations into MDRs [9,29,31].

In addition to theoretical studies, spectroscopy experiments, such as those conducted by Eversole, Jay D., *et al* [23] involve measuring the scattering properties of the objects to identify the resonant peaks associated with MDRs. These experiments provide valuable data on the resonant frequencies and field distributions, aiding in the validation and characterization of MDRs.

The combination of theoretical models and experimental techniques plays a crucial role in unraveling the intricate mechanisms and properties of MDRs in water-based objects [21]. It is important to distinguish traditional MDR research from the specific focus on water-based objects in my work. While MDRs have been studied in various materials, the unique interest in water as a high-index photonic material distinguishes my work from much of the nanomaterial MDR research.

2-C) Plasmonic and MDRs hotspot

Plasmonic and MDR hotspots are localized regions of intense electromagnetic field enhancement found in various types of structures, including plasmonic structures composed of metals, dielectrics, and hybrid materials such as dielectric-coated metal-core structures [32,33]. Plasmonic hotspots are induced by metallic nanoparticles or nanostructures, and their characteristics can be precisely controlled by tuning size, shape, polarization, and arrangement parameters [34]. For instance, the spacing and periodicity between nanoparticles govern the coupling and interaction of individual hotspots, resulting in collective plasmonic effects and modifications to the overall hotspot distribution. These findings highlight the importance of carefully designing the arrangement of nanoparticles to engineer hotspot properties [35].

MDRs hotspots in dielectrics offer an alternative to plasmonic hotspots. Dielectric materials exhibit resonant behavior due to their unique morphology and refractive index contrast, leading to the formation of MDR hotspots [33]. These hotspots, similar in nature to plasmonic hotspots, arise from the resonant behavior in dielectric materials. However, these hotspots are different from standard high-intensity field concentrations and the difference is that hotspots are formed outside the object and have more tightly focused presence in the designated area. Our group's previous work [1] provides a direct example of MDRs in aqueous dimers, highlighting the enhanced electromagnetic fields within water-based structures. The study in the referenced article investigated the plasma formation in grape dimers by linking it to the microwave resonances of cm-sized aqueous dimers. It demonstrated that the dielectric properties of the aqueous objects and the unique morphology of the dimers result in the formation of MDR hotspots outside the spheres.

Two recent investigations by other research groups have been inspired by the ground-breaking work previously done in our research group about plasma formation in grapes [1]. They have delved into the phenomenon of dimer-induced microwave plasma. These studies have primarily focused on the formation of focused dimer hotspots and strategies for controlling these microwave hotspots within aqueous dimers [36, 37]. Dimers serve as a special kind of antenna, not only enhancing field concentration but also allowing for a more compact concentration of fields compared to conventional lenses. This antenna is "passive" as it requires no external power or circuitry.

2-C-1) Applications of MDR and plasmonic hotspots

These kinds of hotspots offer several advantages in sensing and detection applications. The enhanced electromagnetic fields within these hotspots can greatly amplify the interaction between light and analyte molecules, resulting in increased sensitivity and enabling the detection of low analytes concentrations while improve the selectivity of the sensing platform [38].

The formation of a hotspot in the near field outside of the beads holds significant importance due to its super-tight focus. These hotspots, particularly when employing dimers as nanomaterials on a microscope plate, have the potential to advance single molecule detection in sensing applications [4]. The concentrated light within such hotspots opens up possibilities for novel sensing techniques, akin to those employing nanophotonic systems for dimer formation and sensing [39].

MDR hotspots hold relevance in aerospace-related challenges and have been explored for their potential in detecting airborne particles, monitoring fuel quality, and addressing aerospace sensor needs [24]. MDR-based sensors rely on the detection of small shifts in

optical resonances of dielectric spheres, known as whispering gallery modes (WGMs), which can be harnessed for various aerospace applications. applications. The sensor concept is based on the detection of small shifts of optical resonances in dielectric spheres caused by external effects.

MDR and plasmonic hotspots are pivotal in optics and photonics for enhancing light-matter interactions at the nanoscale. These hotspots enable precise control over light, offering potential for compact photonic devices[19,40,41]. By concentrating electromagnetic energy, they enhance light harvesting, emission, and imaging in nanostructured devices [35, 42–44], and hold promise for efficient energy conversion in solar cells, photocatalysis, and photothermal systems [45].

Despite the advantages of plasmonic hotspots, there are some limitations that need to be considered. One limitation is the fabrication challenges associated with achieving precise control over the size, shape, and arrangement of the nanoparticles or nanostructures. Variations in these parameters can impact the hotspot intensity and location, affecting the overall performance of the sensing platform [4]. Additionally, the localized field enhancements in plasmonic hotspots are highly sensitive to environmental changes, such as temperature, humidity, and refractive index variations, which can introduce noise and limit the reliability of the measurements [46].

It is worth noting that MDR hotspots in water-based cm-sized objects in the microwave regime can be related to plasmonic hotspots in the visible regime. Understanding the similarities and differences between these hotspots can provide insights into the design and optimization of sensing platforms across different frequency regimes. While plasmonic hotspots have shown promise in sensing and other fields, there are still challenges and gaps in knowledge that need to be addressed. Future research efforts should focus on advancing the understanding of hotspot phenomena, exploring new materials and techniques, and

developing innovative approaches to enhance the performance of hotspots in various applications.

Chapter 3: Methodology

In this section I describe the computational methods we used to study morphology-dependent resonances in (simulated) aqueous beads at microwave frequencies. These beads consist of isolated spheres of water in a "monomer geometry" or combined to form "dimers" or "clusters". I use COMSOL Multiphysics for finite element method (FEM) simulations to study this subject and I explain the steps involved in running and analyzing these simulations in this chapter. My FEM calculations of internal resonances are done for water-based spheres irradiated at 2.45 GHz in free space.

We can break down the finite element method into four general steps: The first step is a model set-up defines the equations to solve, creates the model geometry, defines the material properties, and sets up the simulation boundaries. The second step is meshing and discretizing the model volume using finite elements. The third step is solving a set of linear equations that describe the electromagnetic fields (i.e., "running the simulation"). Lastly, we postprocess our data which involves extracting useful information from the computed steady-state electromagnetic field distributions.

Overall, this methodology chapter provides a comprehensive description of the FEM simulations I performed, including all relevant details about the object geometry, material properties, simulation settings, and data analysis. Simulations were performed with COMSOL Multiphysics version 5.3.

3-A) Introduction to COMSOL Multiphysics

Real-world electromagnetic problems pose challenges for analytical calculations due to the complex physical geometries present in practical devices, inherent complexity, and non-

linearity of underlying physical phenomena. However, by incorporating suitable boundary conditions and constitutive relationships, computational techniques can overcome the difficulty of deriving closed-form solutions for Maxwell's equations. This highlights why computer modeling plays a crucial role in evaluating the effectiveness of a design during its development phase. Modeling can be employed to address optimization design issues, where an objective function comprising various physical properties (such as dielectric constants, thermal conductivities, and layer thicknesses) is optimized while considering physical constraints such as wavelength, index of refraction, and temperature.

I use the COMSOL Multiphysics package to conduct a three-dimensional steady-state analysis, simulating aqueous structures exposed to 2.45 GHz electromagnetic radiation in free space. In COMSOL, we have the option to solve problems using either steady-state or time-dependent analysis. The choice between these two approaches depends on the nature of the problem we are trying to solve and the behavior we want to capture in our simulation. Steady-state analysis is particularly useful for problems where the transient behavior is negligible (or unimportant), and we want to determine the system's response under a steady set of conditions. Steady-state analysis is used for our study as we assume that the system's properties and boundary conditions do not change with time, and the solutions remain constant.

COMSOL Multiphysics is an effective tool for simultaneously solving coupled physical phenomena. The software provides an interactive environment for solving systems of partial differential equations (PDEs) in up to three dimensions. These equations can be either obtained from a model library or prepared in a general form by the user. I used the

pre-packaged models in COMSOL. COMSOL Multiphysics internally compiles the set of PDEs that describe the model and solves them using FEM.

The software incorporates powerful adaptive meshing and error control, employing a range of numerical solvers for efficient finite element analysis. Using finite-element simulations, we predict the resonant behavior of grape-sized aqueous spheres and clusters and further explore the differences between internal and near-fielf mode intensities for different geometries in free-space at microwave frequencies. The following sub-section illustrate how COMSOL Multiphysics operates specifically for my project.

3-B) Physics module

One of the first steps involved adding the "Electromagnetics Physics Module" as the selected physics interface. Then, I chose the Frequency Domain study type from the list in the chosen physics interface. Other available study types include “Time Explicit” and “Transient”. The "Frequency Domain” Study type is specifically designed for conducting source-driven simulations at a single frequency or at a sequence of frequencies. It allows for computing the linear response or linearized model subjected to harmonic excitation. This interface enabled the analysis of steady-state electromagnetic field distributions for radio frequency electromagnetic waves in the frequency domain.

Creating global parameters is important for easily assigning variables throughout the model and for facilitating easier manipulation of parametric sweeps in later research stages. I used the Parametric Sweep functionality in my simulations to vary bead sizes (the swept parameter) and their corresponding gap distances, all at a fixed frequency of 2.45 GHz.

After running these simulations, I determined where the resonances are found (resonant sizes) and other relevant phenomena by interpreting the outcomes I got from COMCOL, such as internal energy densities over a range of bead sizes, for example.

3-C) Design of simulation geometries

Object geometries were created within the COMSOL Model Builder to accurately depict the spheres and their 3-D orientations. Spherical geometries were employed to construct the objects, while block geometries were used for the external simulation box filled with air. This rectangular simulation space was designed around the object.

The first geometry examined was a single sphere with a radius denoted by r. The range of r spanned from 0.5 to 2 cm, with a step size of 0.01 cm. The simulation box was designed as a cuboid with constant dimensions of 25 cm width, 25 cm depth, and 40 cm height, as depicted in Fig. 3.1. This size was chosen to accommodate a sensible range of sphere sizes, striking a balance of mesh density, computational time, and spatial resolution.

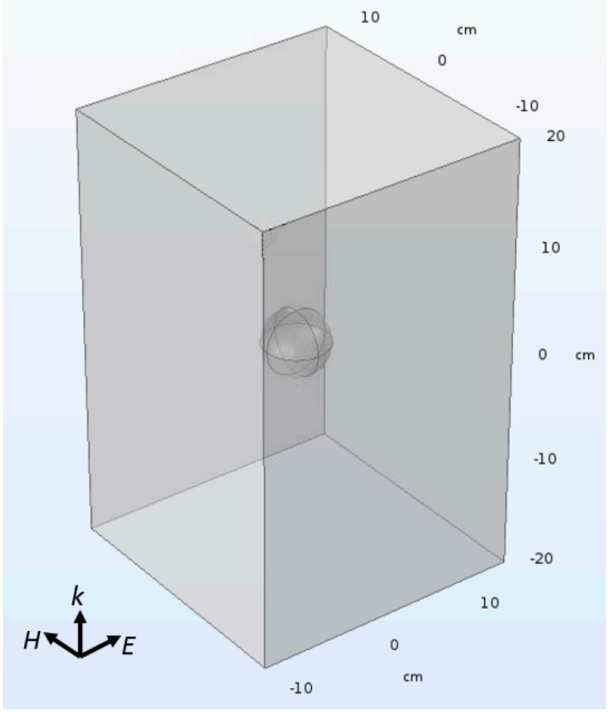

Figure 3.1. Single sphere geometry, wave propagating geometry, and the simulation box.

The second geometry investigated was the “dimer”, comprising two spheres with a separation distance denoted by *d*. The size of the dimers was determined by the radius of the spheres, again varying from 0.5 to 2 cm. A deliberate gap was introduced between the spheres with a fixed value of $d = r/50$, serving two purposes: Firstly, this gap prevented geometric features smaller than a single element as to avoid simulation artifacts. This is especially important when searching for super tiny hotspots at the 'contact' point between the spheres. Secondly, the gap facilitated the quantification of the axial hotspot outside of the object. By intentionally leaving a gap, the hotspot's strength could be more accurately measured, eliminating the likelihood of simulation artifacts arising from sub-resolution meshing. It's worth noting that we initially explored various gap sizes in our simulations, and our findings indicated that while we observed no discernible differences in results, the

chosen gap size ($r/50$) resulted in consistent and reliable results across different configurations. This approach not only standardizes our gap size but also addresses concerns about the sensitivity of results to small changes in gap size.

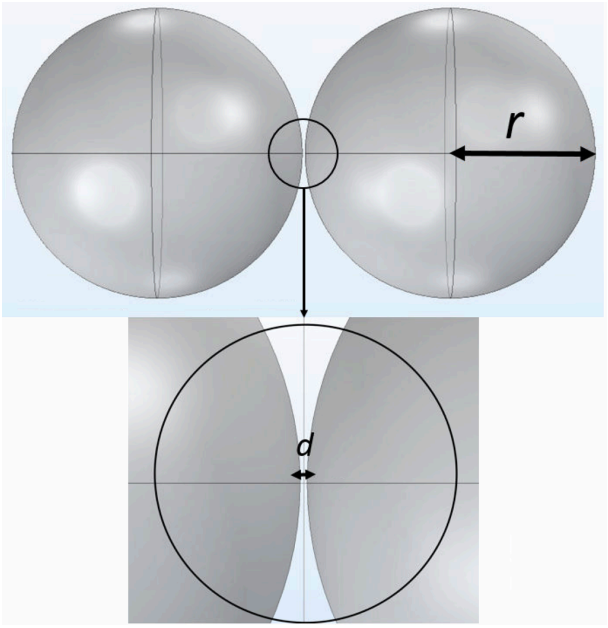

Figure 3.2. Geometry of a Simulated Dimer: Two Spheres with the radius of r and an axial gap distance of $d=r/50$

We initially define three fundamental orientations of dimers based on the dimer axis in relation to the propagating and electric field polarization directions. We denote these three fundamental excitation geometries as TrAx, AxTr, and TrTr orientations. For example, by TrAx orientation we mean that the dimer axis is oriented transverse to the propagating direction ($\boldsymbol{k}$) and along the polarization direction ($\boldsymbol{E}$). So, the TrAx dimer is excited by a plane wave propagating transverse to the dimer and polarized along the dimer axis. The AxTr dimer, however, is excited by a plane wave polarized transverse to the dimer axis and propagating along the dimer axis. Finally, the TrTr dimer is excited by a plane wave

polarized and propagating transverse to the dimer axis. These geometries are depicted visually in Fig. 3.3.

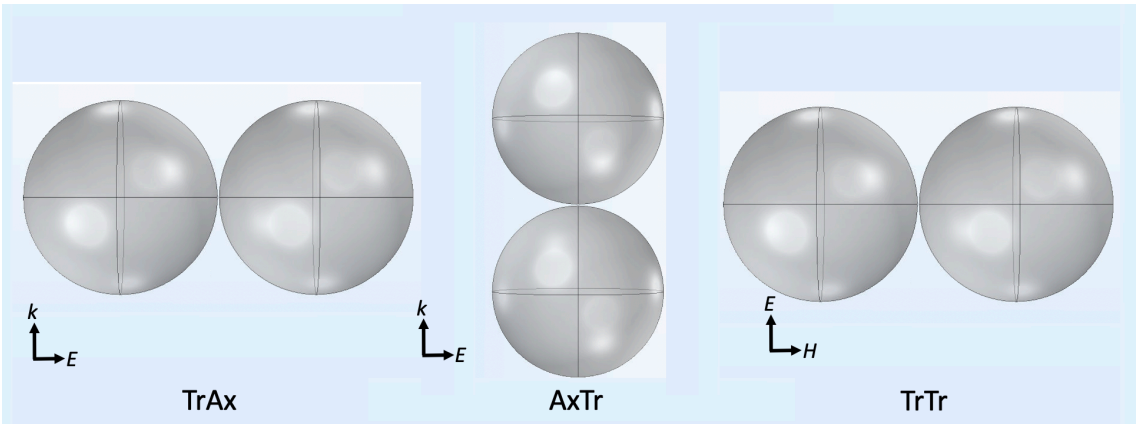

Figure 3.3. Three fundamental dimer orientations named for their *k*-*E* directions: TrAx, AxTr, and TrTr.

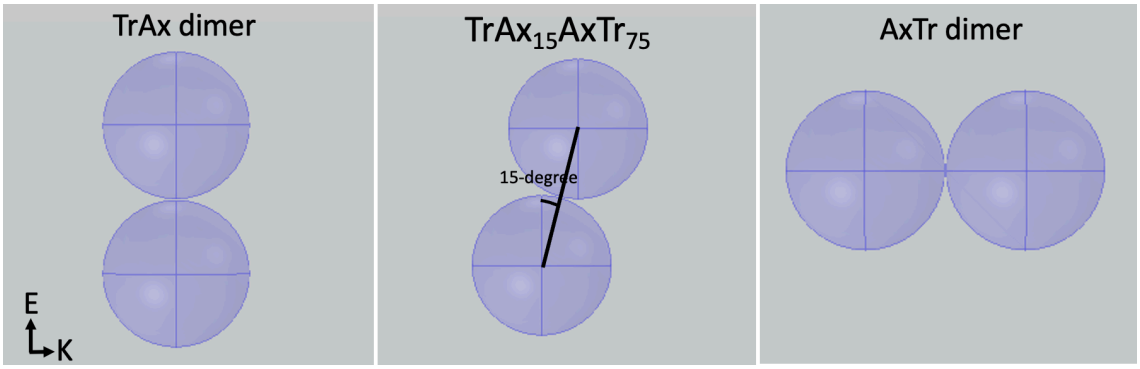

Figure 3.4. $TrAx_{15}AxTr_{75}$ intermediate dimer represents a 15-degree rotation from TrAx to AxTr

Following the three fundamental dimer orientations, the study progressed to explore "intermediate" dimer orientations. Five distinct intermediate orientations were defined between each pair of fundamental orientations. These intermediate orientations were swept

from one fundamental orientation to another (a 90-degree rotation) in 15-degree increments. The same plane and radius were retained while varying the angle.

The nomenclature I use for the intermediate dimers is based on the orientation and rotation angle from one primary dimer to another. For example, the notation $TrAx_{15}AxTr_{75}$ signifies that this intermediate dimer is rotated 15 degrees from the TrAx dimer towards the AxTr dimer.

Alternatively, it can be understood as having a 75-degree rotation relative to the AxTr dimer. Similarly, $TrAx_{60}TrTr_{30}$ represents an intermediate dimer that transitions from the TrAx dimer to the TrTr dimer with a rotation angle of 60 degrees from the TrAx dimer. By using this naming convention, we can clearly identify the orientation and rotational relationship between the intermediate and primary dimers. The $TrAx_{15}AxTr_{75}$ intermediate orientation is depicted in Fig. 3.4 as an example.

Finally, using primary and intermediate dimer orientations, trimer configurations were defined, representing the simplest form of a cluster geometry. A trimer consists of three spheres arranged in a planar configuration, conceptually composed of three dimers on this plane. The coordinates of center points for each sphere in a trimer are calculated to create the geometry in COMSOL. Trimer models could be rotated to yield additional trimers on different planes. Various trimer models were examined, comparing different combinations of dimers on different planes. An example of a *kE*-AxTr trimer is depicted in Fig. 3.5.

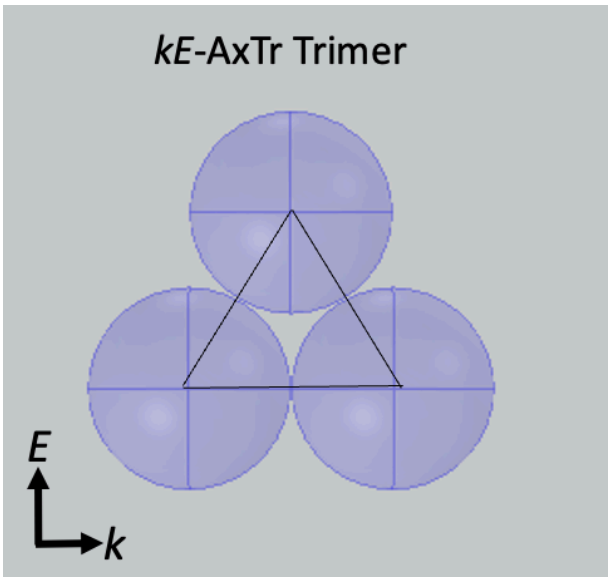

Figure 3.5. A trimer orientation on the *k*-*E* plane denoted as *kE*-AxTr trimer meaning it resides in the *k*-*E* plane and contains a AxTr dimer (The gap as with the dimers is maintained in trimers).

3-D) Simulation settings

In this section, I describe the simulation settings used, including the solver, boundary conditions, and relevant parameters. In the Electromagnetic Wave Module, various types of boundary conditions (BC) are available to define the behavior of the electromagnetic waves at the boundaries of the simulation box, including perfect electric conductors (PEC), magnetic perfect conductors (PMC)—which both are perfect reflectors and do not represent a free-space condition—, transition boundary conditions, and scattering boundary conditions (SBC). Free-space irradiation was simulated using large-area plane-wave incidence. The dielectric object was placed at the center, and fully absorbing boundary conditions were applied to the boundaries of the simulation box for eliminating reflections and accurately represent the free-space environment. Fully absorbing boundary conditions ensure complete absorption of incident waves, preventing any reflection back

into the simulation domain. Notably, in COMSOL, scattering boundaries can be considered as absorbing boundary conditions (ABC) when the incident radiation is precisely normal to the boundary, effectively absorbing plane waves.

We can think of the first four resonances happening at four different frequencies, but as we are interested in mapping resonances at a fixed at the frequency of 2.45 GHz, another way to think of it is resonances at four different object sizes. This means that at a certain size, a sphere of water would be resonant and when it gets bigger there would be another resonance that looks different. So, in this study, we keep the frequency fixed and sweep the radius of water beads as a size parameter. This process continues across the range of simulated sphere diameters. The study has a built-in setting that determines the size steps and size of the full simulation. Just like the mesh setting is more precise the denser the mesh, the parametric sweep portion of the study is more precise the denser the size steps are.

3-D-1) Boundary conditions

In COMSOL, it is important to provide clear definitions of boundary conditions and characteristic equations for all boundaries and domains within the model. A domain in COMSOL refers to a volume that is bounded by known conditions and represents the simulation box model in our case.

I employed scattering boundary conditions in COMSOL for the simulation box because these scattering boundary conditions provide a non-reflecting behavior for normally incident waves, effectively eliminating reflections and maintaining the desired non-reflecting characteristics. By utilizing these specific scattering boundary conditions, we ensured an accurate representation of the free-space environment without reflections or

interference, enabling focused investigations into the interaction of the dielectric object placed at the center of the simulation box.

In my simulations, one end of the simulation box, as shown in Fig. 3.6, was assigned a scattering boundary condition with a plane wave specified by the *E*-field. This means that an external predefined plane wave with specific properties, such as direction, polarization, and amplitude, is applied as the incident field on this particular boundary. This enables us to investigate the interaction between the incident plane wave and the object, observing the resulting scattering behavior and response of the electromagnetic fields.

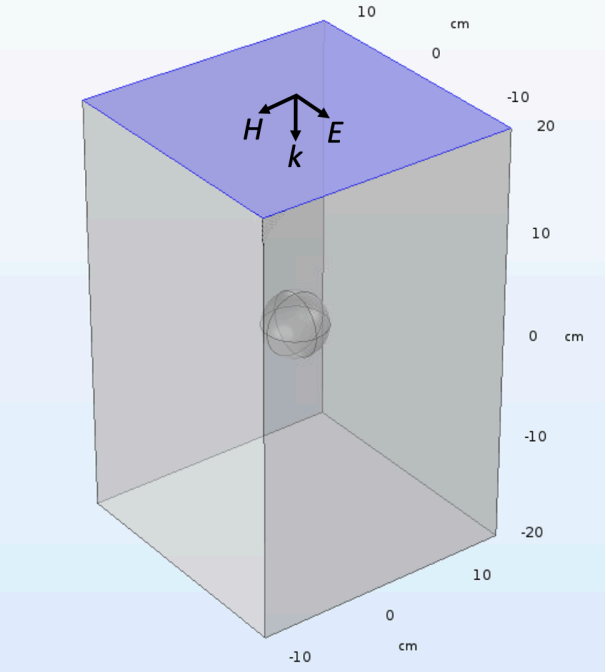

Figure 3.6. Microwave radiation at a frequency of 2.45 GHz is introduced through the upper boundary (blue surface, scattering boundary condition) along the propagating vector, ***k***. All other boundaries of the simulation box (grey surfaces) are modeled as perfect absorbers.

On the other hand, the remaining boundaries of the simulation cuboid were assigned absorbing condition with no incident field. This implies that no predefined incident field is specified for these boundaries. In other words, the original source is the top boundary of the simulation box, and none of the other sides act as sources.

3-D-2) Material properties

All objects are simulated as spheres of water with a mass density of 1.0 g/cm^3 and a relative complex permittivity of $\tilde{\varepsilon} = (\varepsilon_1 + i\varepsilon_2) = 80 + i9.5$ at a temperature of 20°C and at a frequency of 2.45 GHz [2]. To simplify the modeling process, the dielectric properties were assumed to be uniform throughout the object, independent of any localized temperature gradients that might occur during irradiation. In reality, the complex permittivity is temperature dependent, with both the real part and imaginary part diminishing at higher temperatures [16], as mentioned in Section 2-A-1.

The ambient material in the simulation volume is air. Air as the transmission medium was modeled with relative permeability and permittivity values both equal to unity (i.e., $\mu_r = \varepsilon_r = 1$) which are also the relative permeability and permittivity in vacuum. The specific values used for the dielectric and other relevant properties assigned to the air and water materials used in these simulations are presented in Table 3.1.

Table 3.1. Material properties assigned to the air and water used in the simulations.

Property	**Air**	**Water**	**Unit**
Relative Permeability, μ_r	1	1	(unitless)
Relative Permittivity, ε_r	1	80+*i*9.5	(unitless)
Electrical Conductivity, σ	0	5.50E-06	S/m
Density	1.225	1000	kg/m³
Thermal Conductivity	0.026	0.6	W/(m·K)
Refractive index, $\tilde{n}$	1	9+*i*0.6	(unitless)

3-D-3) Meshing

The resolution of the finite element mesh plays a crucial role in discretizing the model. COMSOL employs meshing and solver settings to conduct the finite element analysis. By dividing the model into small tetrahedral elements, the mesh generates volumes within the simulation domain. These volumes serve as individual elements where the simulation equations are calculated. FEM breaks down the model into geometrically simple shapes, enabling the computational model to solve the simulation equations by considering the element material interfaces of the mesh. The quality of the computation's solution output can be strongly dependent on the chosen mesh settings.

In COMSOL, "sequence type" and "size element" are two different parameters used in the meshing process. The sequence type refers to the order in which elements are created during the meshing process. There are two sequence types available: "User-controlled mesh" and "Physics-controlled mesh". In the user-controlled sequence, one has full control

over the order in which elements are created during the meshing process. One can specify the element creation order manually based on specific requirements. However, in the Physics-controlled Sequence COMSOL automates the meshing process by prioritizing elements based on the physics involved in the model. Based on the physics interfaces and the model geometry, it creates a well-suited mesh considering physical properties, material boundaries, and user-defined physics settings. This approach is advantageous for complex or Multiphysics models, as it handles the interplay of different, simplifies the workflow, and reduces manual intervention. Thus, I used the Physics-controlled sequence for simplicity and speed.

The size element parameter determines the characteristic size of the mesh elements in our model. It controls the element size in regions where the mesh needs to be refined or coarsened. The size element parameter influences the overall mesh density and quality. Smaller element sizes lead to a finer mesh and more accurate results but can increase computational requirements. Larger size elements can reduce computation time but may result in lower accuracy or create artifacts as larger mesh sizes accumulate errors throughout their volume. It is important to choose an appropriate size element that balances accuracy and computational efficiency for our specific simulation. So, I chose the “coarse” mesh among the list from extremely fine to extremely coarse. I found that the coarse mesh, which corresponds to the 6^{th} element size from a list of 9 sizes, yielded sufficiently accurate results within a reasonable computation time. In this mesh, each element has a volume of 0.073 mm^3. This means that in a gap distance of radius/50 between two water beads, we have 1.38 elements (the gap is longer than the length of one element of this mesh) which

represents nearly half of the number of elements a fine mesh would have over the same length.

3-D-4) Model equations and solver

The Electromagnetic Waves in Radio Frequency (RF) module describes the electromagnetic field model of a domain using wave equations and additional equations that account for the interaction between the incident wave and the material properties. This wave equation domain setting uses the relative permittivity of the material to model the electromagnetic field accurately in the frequency domain providing valuable insights into the interaction between the electric field and the geometry, as well as the field's variation with different parameter values.

Under the assumption that the fields vary sinusoidally in time at a known angular frequency ω and that all material properties are linear with respect to field strength, the governing Maxwell's equations in three dimensions reduce to [47]

$$\nabla \times (\mu_r^{-1} \nabla \times E) - \frac{\omega^2}{c_0^2}\left(\varepsilon_r - \frac{i\sigma}{\omega \varepsilon_0}\right) E = 0, \quad (3)$$

where the material properties are μ_r, the relative permeability; ε_r, the relative permittivity; and σ, the electrical conductivity. The equation is a modified form of the Helmholtz equation, accounting for material properties and complex permittivity and conductivity.

With the speed of light in vacuum, c_0, the above equation is solved for the electric field, throughout the modeling domain, where E is a vector with components E_x, E_y, and E_z. It is important to note that the time-varying electric fields give rise to magnetic fields (H-fields) through the fundamental relationship described by Maxwell's equations (the

primary time-step computation occurs on E, and only then the change in E is used to calculate H). Thus, the magnetic fields are derived from the time-varying electric fields. Once the magnetic fields are found, all other quantities (such as currents, and power flow) can be derived from the electromagnetic field dynamics.

3-E) Output data analysis

Following the completion of the simulations, I proceeded to analyze the results and extract pertinent information, such as the distribution of electric and magnetic fields or the total energy within the object. COMSOL provides a variety of plotting and analysis tools. These include 3D plots, surface plots (a type of 2D plot), derived values tools, data export tools, and more.

Figure 3.7 provides an illustrative cutaway schematic of a study cut plane for an arbitrary studied geometry.

To visualize the electromagnetic fields within the objects, I employed surface plots. This plotting format projects XY, YZ, and XZ planes onto the model, allowing for a clearer view of the field distribution. The surface plots were generated using the selected cut planes from the Data Sets section. By employing various EM field surface plots, a comprehensive understanding of the field shapes inside the objects was obtained. These plots allow for the visualization of the electric field intensity on 2D surfaces and facilitate the identification of different resonant mode shapes. It is worth noting that the plotted surfaces correspond to the surfaces of the 3D models. By selecting expressions such as electromagnetic field norms, energy densities, and more from the available expression list, detailed analysis of these parameters can be performed within the plots.

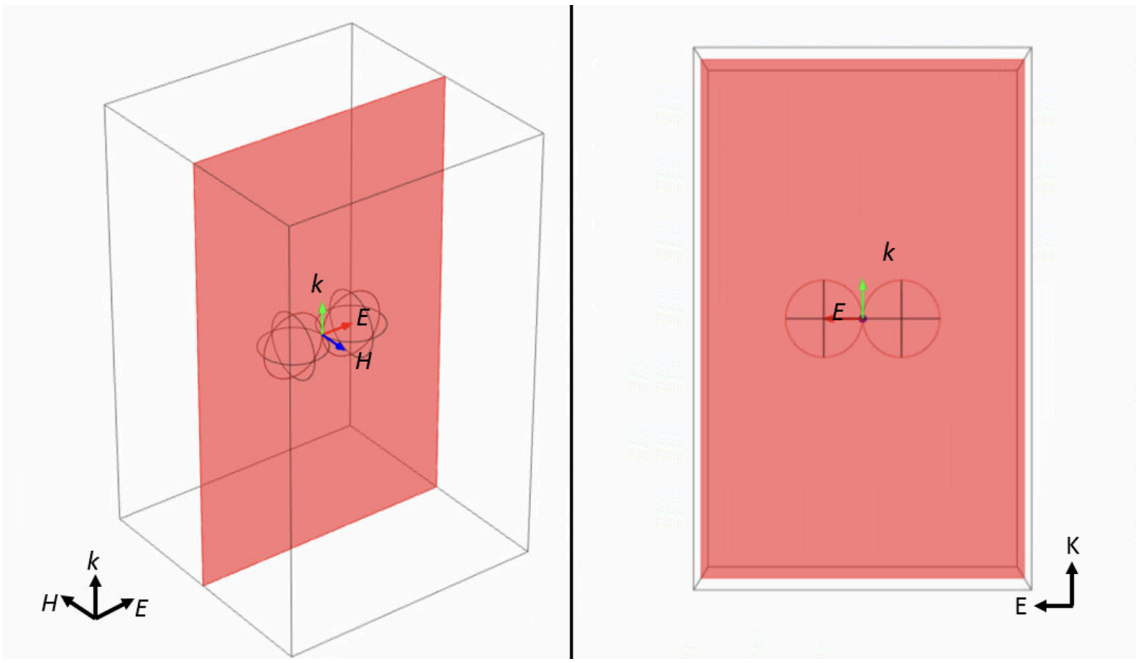

Figure 3.7. Cutaway schematic of TrAx dimer orientation in the *k*-*E* plane study cut plane.

Chapter 4: Results and Discussion

In this chapter, firstly, I talk about aqueous spheres as monomers and present the progression of MDRs in these objects. Next, I describe the three primary dimer orientations and visualization of EM field maps on different planes. I discuss the first four resonances/modes in these three dimer orientations. With a focus on the first two modes, I compare the dimer resonances with those of monomers and explain how the modes are arranged in 3 dimensions. Following that, I discuss intermediate dimer orientations for modeling the transformation of one fundamental dimer geometry to another. I define the angle of decrement to transmit from one orientation to another and repeat this for three primary orientations to demonstrate that the third transition is the combination of two other transitions. I also provide electric and magnetic field maps at each resonant size to discuss the mode and hotspot intensity change in each orientation. Then, in the fourth section of this chapter, I discuss trimers and their relation to a combination of dimer groups. I compare hotspot strengths in trimer models to those hotspots in the isolated dimers. Moreover, I compare different trimer models in an attempt to make a prediction for hotspots in trimers of intermediate orientations. Finally, I discuss how mode orientations change as a function of dimer orientation. We call this a “twisting” of dimer modes. I study twisting in trimers and compare it to that in the isolated dimers.

4-A) Morphology-dependent resonances in single spheres

To understand how microwaving a water bead gives us resonant modes, we first need to know a few things: First, the typical household microwave uses a frequency of electromagnetic radiation at 2.45 GHz which means the wavelength of the microwave inside the oven is about 12 cm long (122.45 mm). We know that interesting things start to

happen when the object or obstacle approaches the same size as the wavelength. A grape (or hydrogel bead) is certainly not 12 cm long, but that is where the index of refraction inside the material plays a role as an important quantity. We need to know the wavelength inside the object. The index of refraction of a material is different at different regimes. The index of refraction for water in the visible regime is only around n=1.33 but it is a lot higher in the microwave regime. The index of refraction of water at the microwave regime is almost 10 (n=9.5) meaning that microwaves travel 10 times slower in the grapes (or water beads) than in the air. It also means that the wavelength in the object is a tenth of its length through the air, so instead of 12 cm, the wavelength of microwaves inside a water object is approximately 1.2 cm which is very close to the diameter of a grape.

Now, we understand that the size of the object we are studying, as a single sphere of water—or "aqueous monomer"—is comparable to the wavelength of the microwaves inside it. This characteristic, the high refractive index of water and the size of the water beads, leads to the formation of standing waves within the object when exposed to microwave radiation. These standing waves result in resonant modes, with the maximum electric field intensity concentrated at the center of the sphere. Thus, the trapped microwaves inside the sphere generate standing wave patterns, contributing to the formation of resonant modes.

The size of water beads plays a crucial role in their resonant behavior within a microwave oven [21]. Typically, non-absorptive materials exhibit extreme amplification of electromagnetic (EM) fields at specific resonant sizes. These modes are characterized by a single size at which the light is trapped, and field amplification is maximum. However, due to water's inherent absorption properties at 2.5 GHz, the resonant peaks in water spheres

are broadened, resulting in less field amplification but over a wider range of sizes. This broadening effect allows us to observe each resonant mode at a range of sizes, eliminating the need for precise control of bead size to achieve resonances. This behavior is similar to that of cavity resonators, where the Q-factor is influenced by the presence of lossy materials [48,49]. The quality factor (Q-factor) of a cavity resonator, which measures the sharpness of resonance, is inversely proportional to the energy dissipation rate caused by the presence of lossy materials, such as water in our case. A higher energy dissipation rate corresponds to a lower Q-factor and a broader resonance peak, indicating less efficient energy storage and higher losses in the system [48,49].

4-A-1) Spectrum and field maps for monomers

Each resonant mode exhibits a distinct distribution of electric and magnetic fields. By examining the electric and magnetic fields (or energy) within the objects, we can visualize the internal mode shapes. Prior to my work, our goal focused on identifying morphology-dependent resonances at microwave frequencies for single water-based spheres. As expected from traditional Mie scattering theory, the first four resonances—corresponding to the smallest resonant bead sizes—look like magnetic dipole, electric dipole, magnetic quadrupole, and electric quadrupole modes, respectively [9].

Figure 4.1 shows the simulated total internal energy density (both *E* and *H* energy densities) for aqueous spheres of different sizes irradiated at 2.45 GHz in free space, showing the internal resonances in the monomer. The equation which refers the total EM energy is $U_t = U_e + U_m$, where $U_e = \left(\frac{\varepsilon_0}{2}\right)|E|^2$ and $U_m = \left(\frac{1}{2\mu_0}\right)|H|^2$ [48]. Resonant conditions are identified through peaks in the internal volume-averaged electromagnetic energy density. The vertical lines on the figure identify the first four resonant sizes at *r*=0.68, 0.95, 1.34,

and 1.65 cm, respectively [50]. The primary (first) resonance occurs at a diameter of 1.4 cm, which closely corresponds to the size of a grape, as previously reported by our group [1]. This particular mode exhibits a considerably higher intensity compared to the subsequent three modes observed in larger spheres.

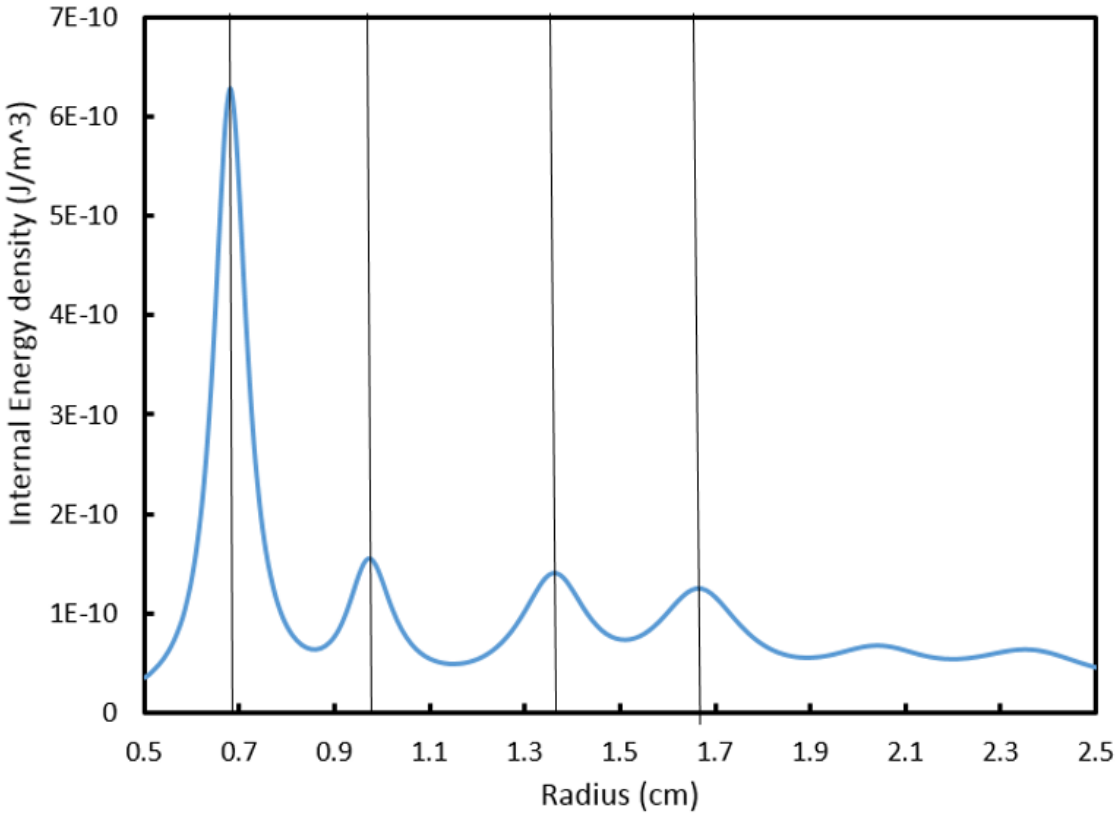

Figure 4.1. FEM calculations of internal resonances in a water-based sphere irradiated at 2.45 GHz in free space.

In Fig. 4.2, I provide the electric and magnetic field maps for the first four resonances on the same plane of *H-E.* For these maps, the colors are not scaled the same and they are normalized to present the internal field shapes properly.

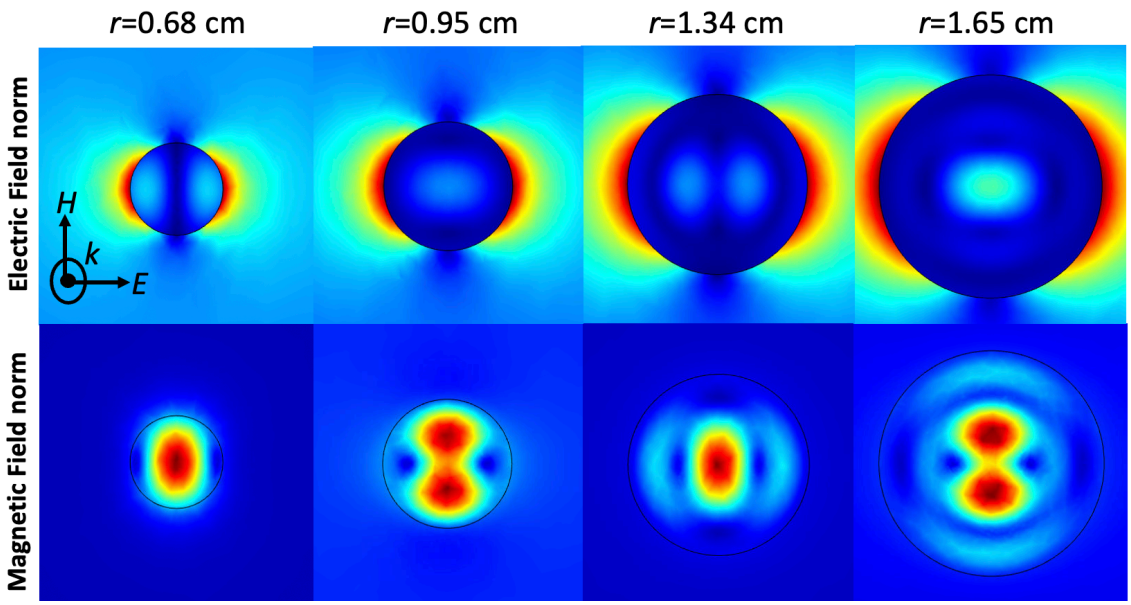

Figure 4.2. Simulated EM field norm maps at the *E*-*H* plane for the first four resonances in isolated water spheres. Note that the external near-field *E*-field concentrations mimic well-known plasmon resonances [3]. The color intensity on these maps varies, highlighting the field shapes within the spheres at these resonances.

The energy density maps of the electric and magnetic fields reaffirm our expectations, indicating that the first four modes correspond to a magnetic-dipole-like (MD), electric-dipole-like (ED), magnetic-quadrupole-like (MQ), and electric-quadrupole-like mode (EQ), respectively [9]. Based on Fig. 4.1 and 4.2, at a certain size, a sphere of water is electromagnetically resonant, and when it gets bigger there are other resonances, each looking different. The primary resonance in aqueous beads (a magnetic-dipole-like resonance) occurs at a diameter of 1.4 cm (r=0.68 cm at 2.5 GHz), while the higher-order resonances are found in incrementally larger beads. These mode shapes provide valuable insights into the fundamental characteristics and behavior of the resonant modes.

The lowest-order mode functions as a magnetic-dipolar mode, displaying a nearly spherical symmetric distribution of magnetic field and a doughnut-shaped electric field

concentration. Depending on the study plane (*H-E* in Fig. 4.2, for example), a map of the electric energy distribution for the first mode would appear either like a doughnut shape or as two lobes. The cut plane of *H-E* for display in Fig. 4.2 shows a two-lobes configuration. The next modes exhibit alternating patterns of electric and magnetic energy density maps, looking like circular distributions and lobed shapes for both magnetic and electric fields.

4-B) Dimers

While there is some evidence in Fig. 4.2 to indicate a concentration of near-field energy in the isolated spheres, my research primarily aims to investigate and compare the microwave resonances in dimer geometries relative to those in the monomers. The key focus is to explore whether dimer configurations exhibit significantly larger field concentrations, potentially orders of magnitude higher than those observed in the monomer. Specifically, I am interested in identifying substantial field enhancements within the gap of the dimer, potentially leading to field energy levels capable of ionizing air and forming a plasma. This investigation centers on morphology-dependent resonances in microwave frequencies, with a specific emphasis on water-based dimer MDR hotspots. The extension of dimer findings to other geometries further contributes to understanding the unique electromagnetic phenomena and paves the way for potential applications in diverse fields.

We have previously observed that when two spheres are well separated (say, by a distance greater than their diameters) they mostly behave as independent objects. In this case, microwaves become trapped within each sphere, with the maximum amplitude of the field energy concentrated at the center of each individual sphere. However, if we move these two spheres close together to the point of contact then we will see some sparks between the spheres because of some interactions between the electromagnetic fields inside them.

So, we get the greatest field concentration occurring at the contact point of these two spheres. Therefore, we call this the “dimer axial hotspot”. This external hotspot is a new resonant feature of MDRs in dimers, distinguishing them from the standard spherical MDRs.

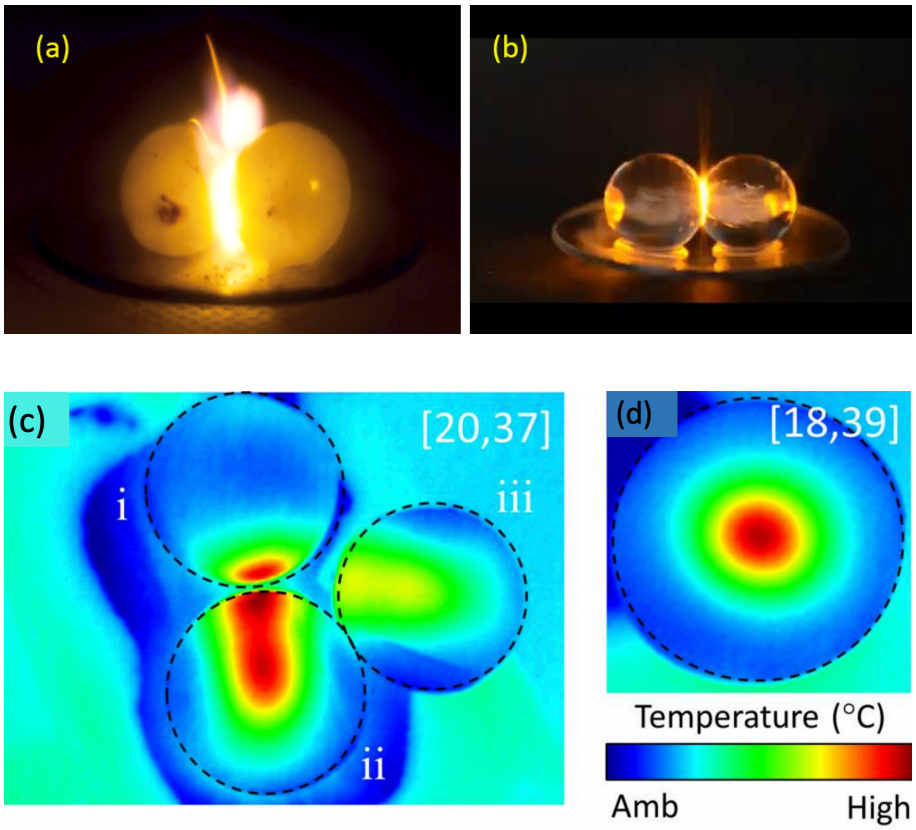

Figure 4.3. (a) Two grapes in the microwave oven, and (b) Grape-sized spheres of water in the microwave oven; I consider these as aqueous dimers. (c) and (d) are thermal maps of large 5.5-cm-diameter water beads. (c) The temperature distribution after 4-second irradiation of a hydrogel dimer. Object *i* is a whole sphere, showing only the hotspot on the surface near the point of contact; regions *ii* and *iii* are the post-irradiation-halved sister spheres to *i*, showing a more complex thermal distribution at the equatorial planes. (d) The temperature distribution of a post-irradiation-halved large bead monomer shows a well-confined radial mode that is hottest in the center. This figure is modified from Khattak *et al.*, 2019 [1].

Early on we found that if we bring two water-based spheres together to create a dimer, these two monomers interact to form something entirely new depending on the orientations, polarization, and excitation directions of microwaves. Studying the grapes in a microwave oven has led to an interest in the idea of "dimerization" of MDRs in water-spheres [1]. When two water beads or grapes are in contact in the microwave oven, there is a hotspot at the point of contact and maybe that is the reason that the grapes spark. Sparking has never been observed in an irradiated single sphere. Even if the primary reason for the spark formation is not well understood, the presence of a pronounced field concentration at the contact point of two resonant spheres is intriguing from a general physics perspective. We use the terms monomer and dimer as an analogy to chemical bonding. The polarization and propagation dependencies further add to the fascination of this phenomenon. While our primary motivation lies in exploring the fundamental physics, The prospect of harnessing such field concentrations, from microwave-sized objects to nanometer scales in the visible regime, remains an interesting aspect of our research.

4-B-1) Dimer hotspots and internal mode shapes

The hotspot itself is strong evidence that a dimer is not a simple addition of two monomers. We denote the hotspot at the point of contact between two objects as an axial hotspot. Dimer hotspots are not just the addition of near field concentration of electromagnetic radiations in two monomers close to each other. A dimer hotspot as an entirely new feature of the dimer is like an "optical bonding". We do not have a rigorous theory of optical bonding; it is just an idea to think where two atoms next to each other make some bond to form an optical molecule and the bond has some character; the same thing happens in a dimer as the dimer has some bonding character. We can draw parallels to the concept of

reduced energy in bonded atoms compared to unbonded atoms. In the case of a dimer, it is the bonding character contributes to enhanced resonant behavior in dimers compared to isolated monomers. The dimer hotspot shows that the dimer is a kind of interference and synergy of monomers (the interaction or cooperation of two monomers in a dimer produces a combined effect greater than the sum of their separate effects).

It is pertinent to note that a comprehensive reference figure (Fig. 4.24) has been included at the end of the 4-C section of this chapter and serves as a valuable point of reference for the entire work on dimers.

Figure 4.4 illustrates the presence of dimerization, where two monomers come together to form a dimer. The electric field shape **inside** monomer at the first mode is shown and is quite similar to that inside of the dimer. However, in the hotspot area, some differences in the field shape and concentration can be observed.

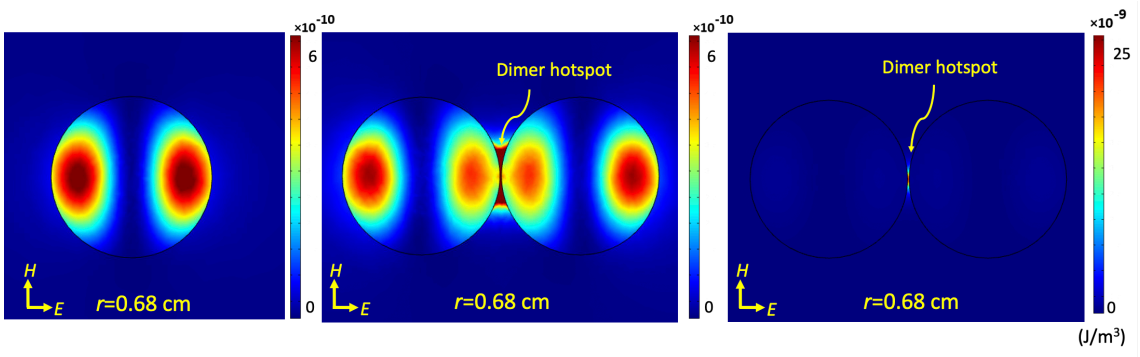

Figure 4.4. Electric field energy density maps on the *H-E* equatorial plane at the first resonance for a monomer and a TrAx dimer. This resonance corresponds to the magnetic dipole mode, as depicted in Figs. 4.1 and 4.2. The central panel presents a dimer map with the same intensity scale as the monomer (left), while the right panel shows the same dimer map rescaled to reveal that the axial hotspot in the dimer can dominate the EM energy landscape over any internal field concentrations in the system.

It is important to note that these maps represent a specific dimer, oriented in a particular way, and captured at the first mode when the spheres have a radius of 0.68 cm. In Fig. 4.5, I present the EM energy density maps for another dimer at a higher mode, providing an additional reference for comparison with that of monomer.

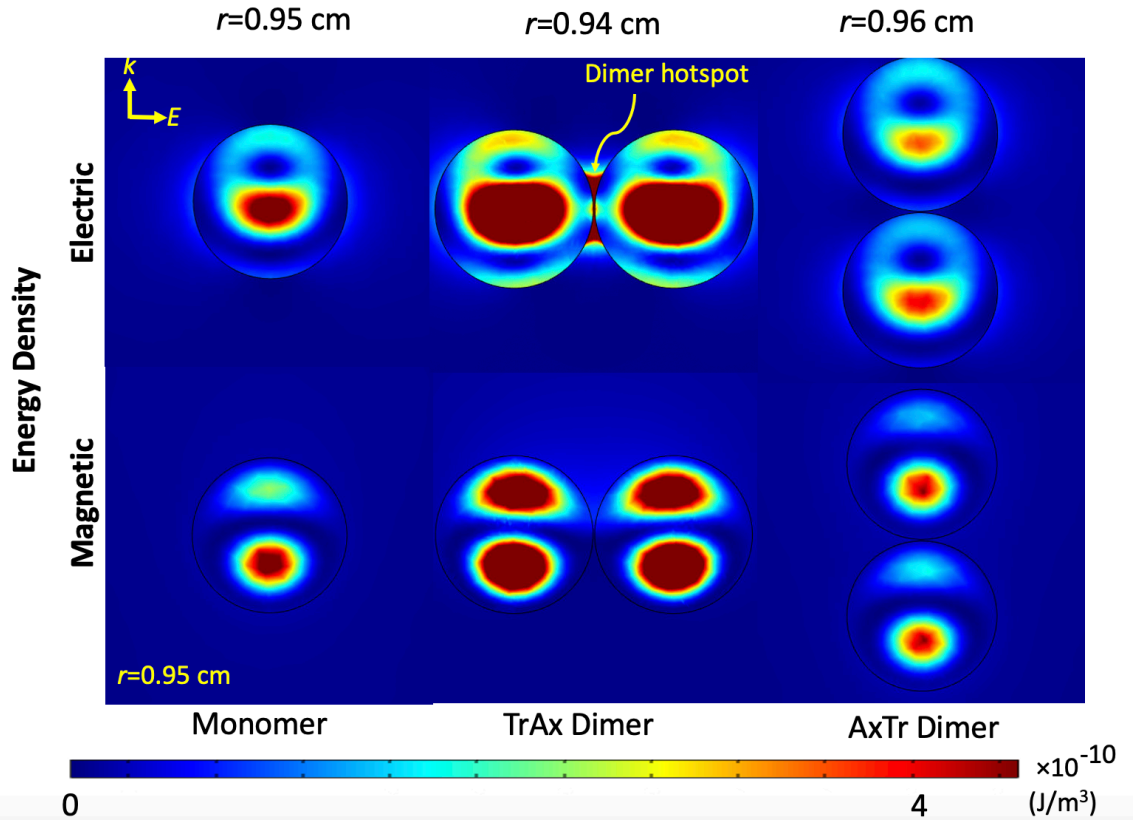

Figure 4.5. Electric and Magnetic field energy density maps for two dimers (TrAx and AxTr) at their second modes. The dimers show similar field shapes (with some modifications) compared to the monomer. This mode is known as electric dipole mode, as shown in Figs. 4.1 and 4.2, but here a different cutting plane is being visualized. Note the presence of an axial hotspot in the TrAx dimer, but not in the AxTr dimer. Any vertical asymmetry is likely due to absorption along the propagation direction.

The field shapes in the energy density maps for these two dimers at their second modes are nearly identical, with some variations observed in certain dimers compared to the monomer. As examples of these variations, the electric and magnetic field concentration is less intense in the AxTr dimer and more intense in the TrAx dimer, both in comparison to the monomer. Additionally, a distinct **electric** hotspot is observed in the TrAx dimer. Furthermore, the internal electric and magnetic modes in the TrAx dimer appear to be twisted compared to the monomer modes. The map colors are scaled uniformly, demonstrating the increased field concentration at the dimer hotspots. However, it should be noted that neither electric nor magnetic axial hotspots form in the AxTr dimer at this resonance.

Figure 4.6 displays several examples of EM field concentration maps for monomer and two dimers at different modes. When simulating the fields inside the dimers, we observe that some of them closely resemble the internal fields of monomers. The AxTr dimer field maps look very similar to that in the monomer, while others exhibit modifications as illustrated in the second map of parts (A), (B), and (C). The TrAx dimer modes look significantly altered from that of the monomer. Moreover, new features, such as a hotspot at the point of contact, can emerge in certain dimers, as demonstrated in the electric field maps of the TrAx and AxTr dimers at the first (r=0.68 cm) resonance in part (A).

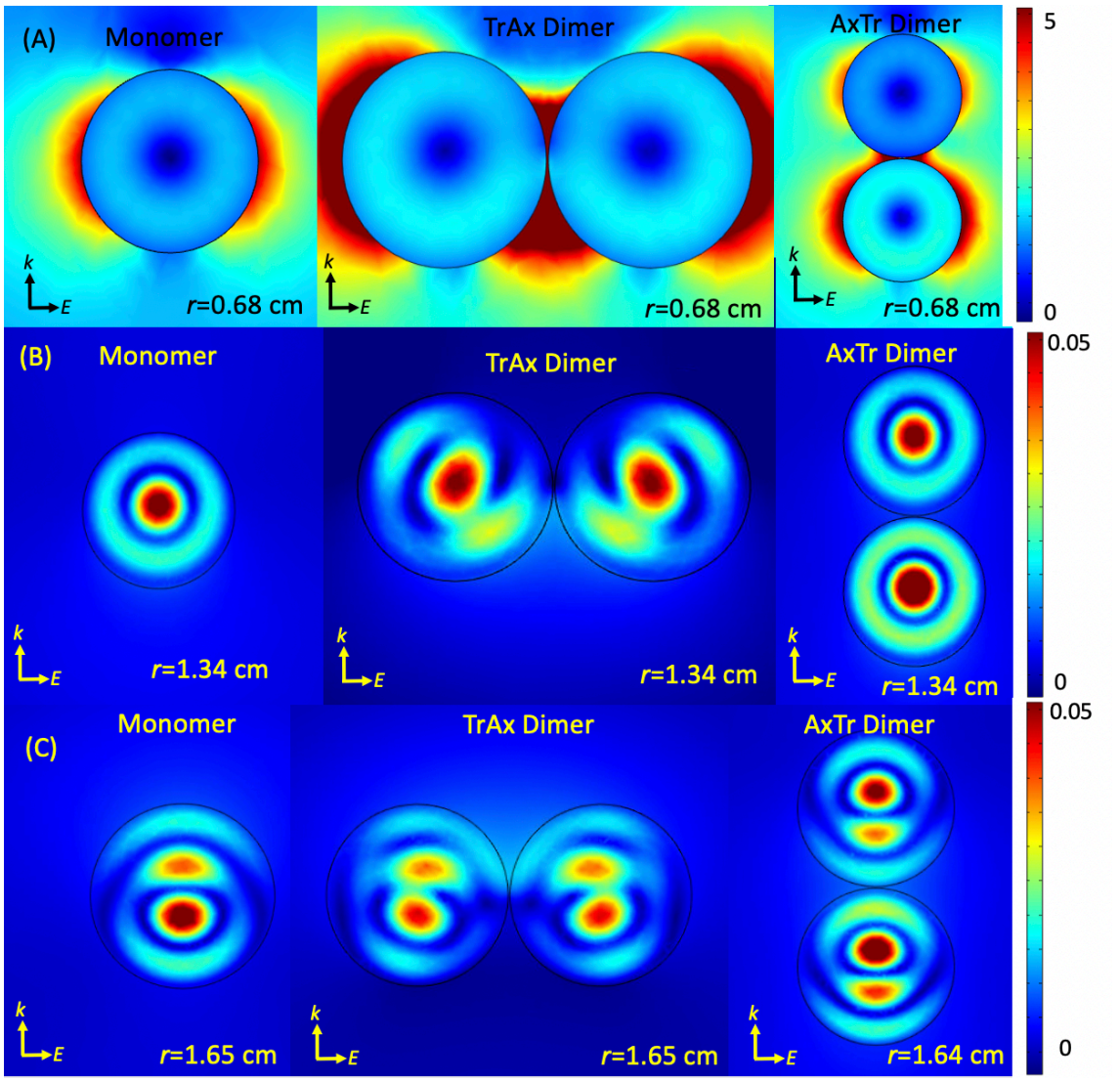

Figure 4.6. EM field concentration inside a monomer and two dimers (TrAx and AxTr) on the *k*-*E* Plane. (A): Electric field maps at the first resonance (magnetic dipole mode) (B): Magnetic field maps at the third resonance (magnetic quadruple mode) (C): Magnetic field maps at the fourth resonance (electric quadruple). No magnetic hotspot is observed in these cases.

4-B-2) Three primary dimer orientations

This section focuses specifically on the three fundamental excitation geometries in dimers, namely TrAx, AxTr, and TrTr orientations. I discuss the effects of different excitation geometries on dimer hotspots and resonance modes. The interesting aspect of this part lies

in understanding the occurrence of hotspots and the fundamental differences in mode characteristics (including internal and external field concentration) between dimers and monomers. In this subsection, I study three fundamental excitation geometries in dimers, illustrated in the diagrams shown in Fig. 4.7.

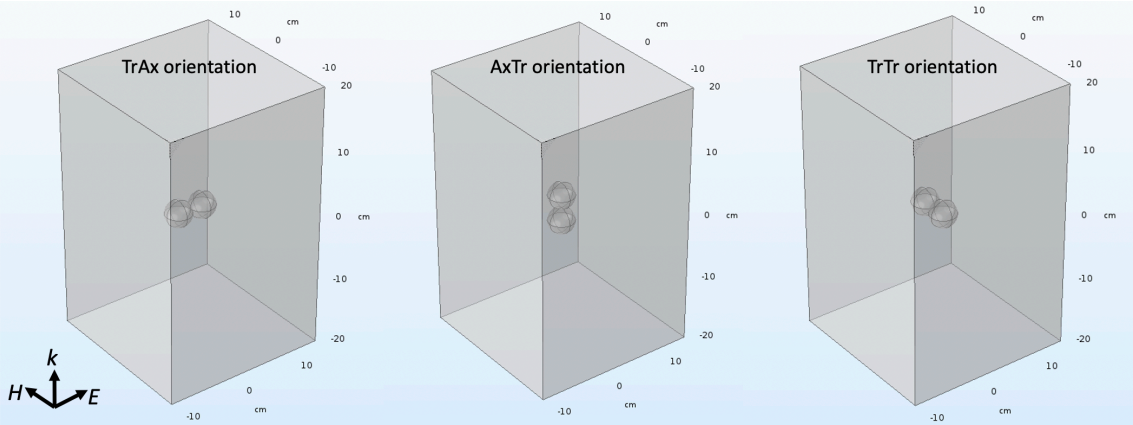

Figure 4.7. Simulation box of dimers along the three fundamental *k*-*E* orientations; TrAx, AxTr, and TrTr.

Figure 4.8 displays the internal energy density of the three primary dimers as a function of size. This spectrum is visualized through **internal** volume-averaged EM energy densities and captures the first four resonances within this size range. Most of the resonances in the three primary dimer geometries are found at the same (or very close) sizes as in isolated MDRs. Table 4.1. represents the first four resonant sizes for the three primary dimers.

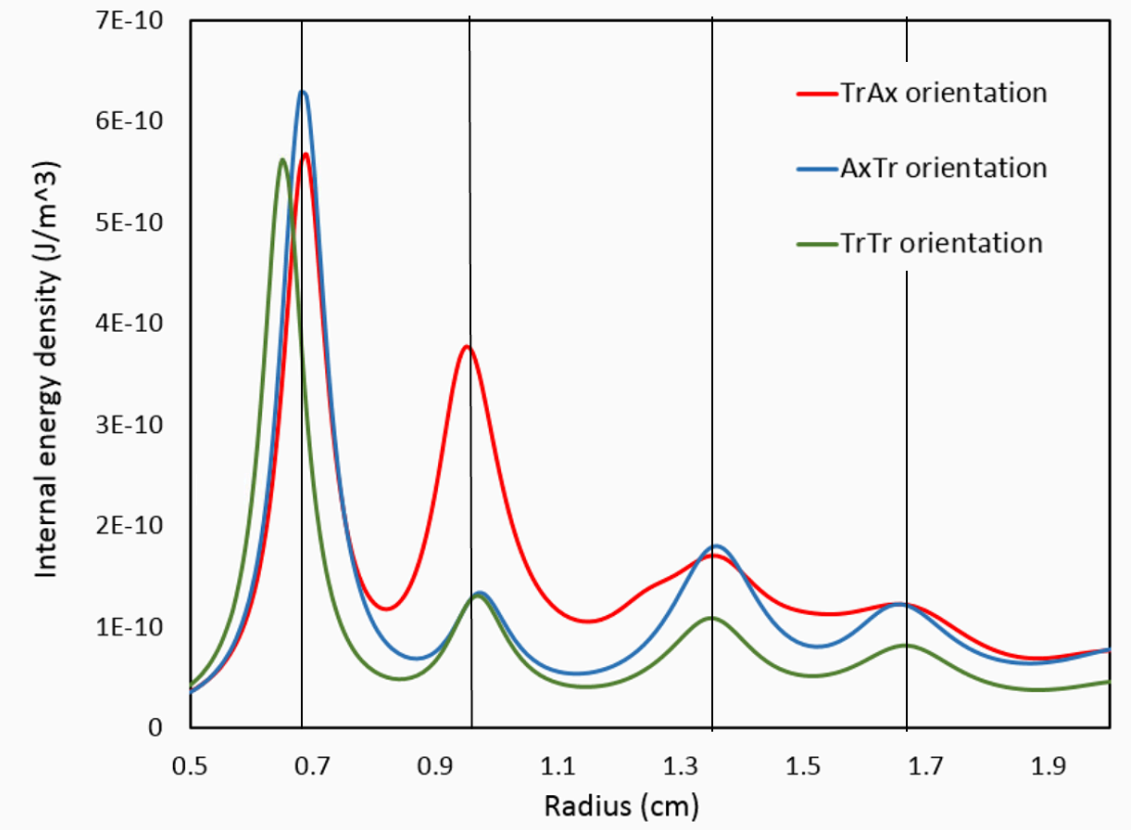

Figure 4.8. The Spectrum of internal resonances in the three primary dimers. The total internal energy density for TrAx, AxTr, and TrTr dimers is represented by the red, blue, and green lines, respectively. The vertical lines represent the peak locations for the isolated (monomer) MDRs, highlighting small shifts in some dimer resonances.

Table 4.1. The first four resonant sizes for the three primary dimers.

Object geometry	First resonant size (r)	Second resonant size (r)	Third resonant size (r)	Fourth resonant size (r)
Monomer	0.68 cm	0.95 cm	1.34 cm	1.65 cm
TrAx dimer	0.68 cm	0.94 cm	1.34 cm	1.65 cm
AxTr dimer	0.68 cm	0.96 cm	1.34 cm	1.64 cm
TrTr dimer	0.65 cm	0.96 cm	1.34 cm	1.65 cm

At the primary resonance, although the resonant size shifts in the TrTr dimer (in comparison with monomer), the energy density in both TrAx and TrTr dimers remains similar, while the AxTr dimer orientation shows a slight difference. Moving to the second resonance, AxTr and TrTr dimers exhibit comparable energy densities, while TrAx dimers demonstrate higher internal energy density. At this resonance, there is another size shift observed in the TrAx resonance compared to the resonant size of monomer.

Finally, at the third and fourth resonances, both TrAx and AxTr dimers exhibit nearly identical internal energy densities, whereas TrTr dimers show slightly lower energy densities. Overall, this figure illustrates that the AxTr dimer is orientation-dependent at the first resonance, the TrAx dimer is orientation-dependent at the second resonance, and the TrTr dimer is orientation-dependent at the third and fourth resonances.

Based on Fig 4.9, the TrAx dimer showcases resonance modes that progress much like those in the individual spheres: A magnetic dipole mode at the first resonance (r=0.68 cm), an electric dipole mode at the second resonance (r=0.94 cm), a magnetic quadrupole mode at the third resonance (r=1.34 cm), and an electric quadrupole mode at the fourth resonance (r=1.65 cm).

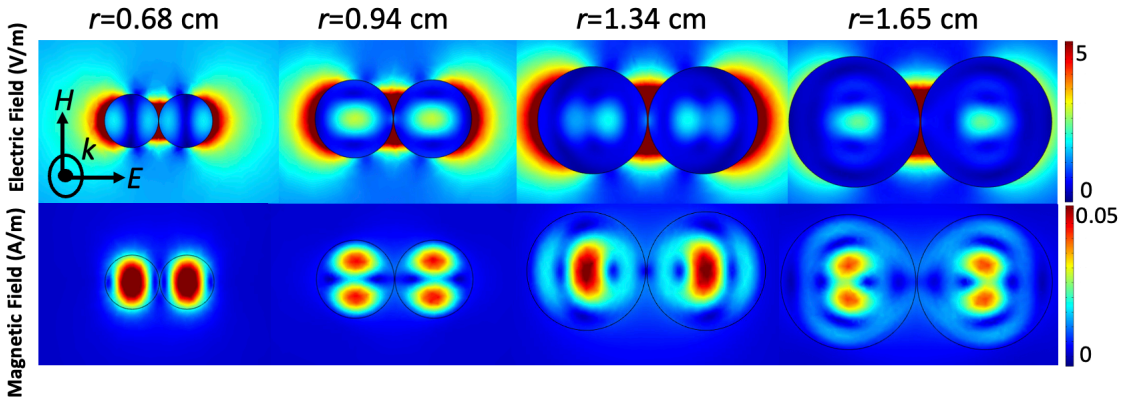

Figure 4.9. Simulated EM field norm maps at the E-H equatorial plane for the first four resonances in TrAx dimer.

The analysis of the EM field concentration within TrAx dimer reveals that the electric field exhibits significantly higher intensity compared to the magnetic field. Moreover, prominent electric hotspots are present, displaying immense concentration compared to the internal field. Upon comparing this figure with Fig. 4.2, we observe that the internal field shapes remain relatively consistent on the same cut plane. However, slight deviations in the modes can be observed at specific resonance points, involving twists and minor modifications in their pattern. For example, at the third and fourth resonances, both magnetic and electric field shapes show a tendency to be pulled toward the point of contact between the two spheres. Additionally, a notable new feature observed at all resonances of the TrAx dimer is the presence of highly intense **electric** axial hotspots. Furthermore, the field concentration and strength differ within the dimer at different resonances. For instance, the magnetic field strength is significantly more intense at the first resonance compared to the next three resonance.

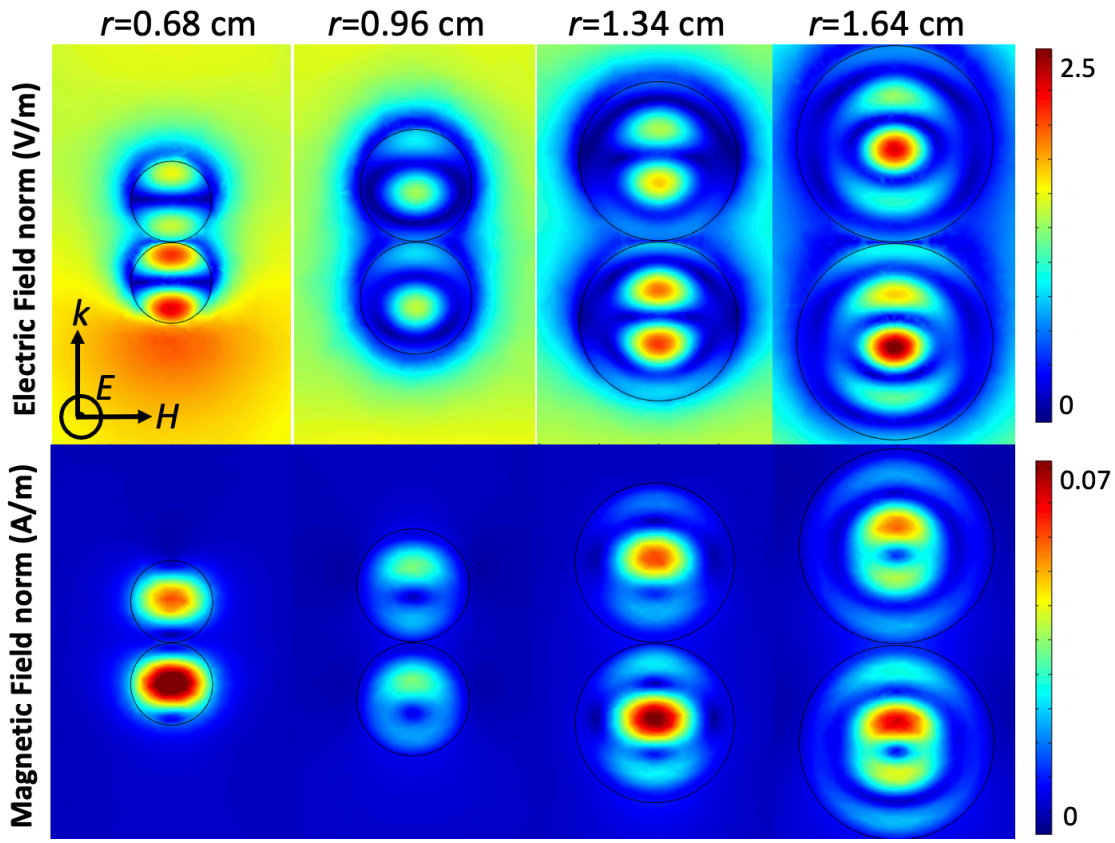

Figure 4.10. Simulated EM field norm maps at the *k*-*H* equatorial plane for the first four resonances in the AxTr dimer.

Based on Fig. 4.10, similar electromagnetic modes are observed at the first four resonances in the AxTr dimer, which is another primary dimer orientation. To study the modes specific to this dimer, simulations are performed at a different cut plane, perpendicular to the polarization direction. Once again, the first four modes correspond to magnetic dipole, electric dipole, magnetic quadrupole, and electric quadrupole modes, respectively. However, there are some differences in the presence and intensity of the axial hotspots, as well as the field concentration within the AxTr dimers compared to the TrAx dimer and monomer.

One notable distinction in the field maps for the AxTr dimer is the vertical asymmetry in the internal field concentration in two spheres of this dimer. This means that due to the absorptive properties of water, as the wave propagates along the dimer axis, some of the field is absorbed in the first sphere. Consequently, the field inside the second sphere is less concentrated and less intense. As a result, both spheres exhibit similar field shapes, with slightly different field intensities.

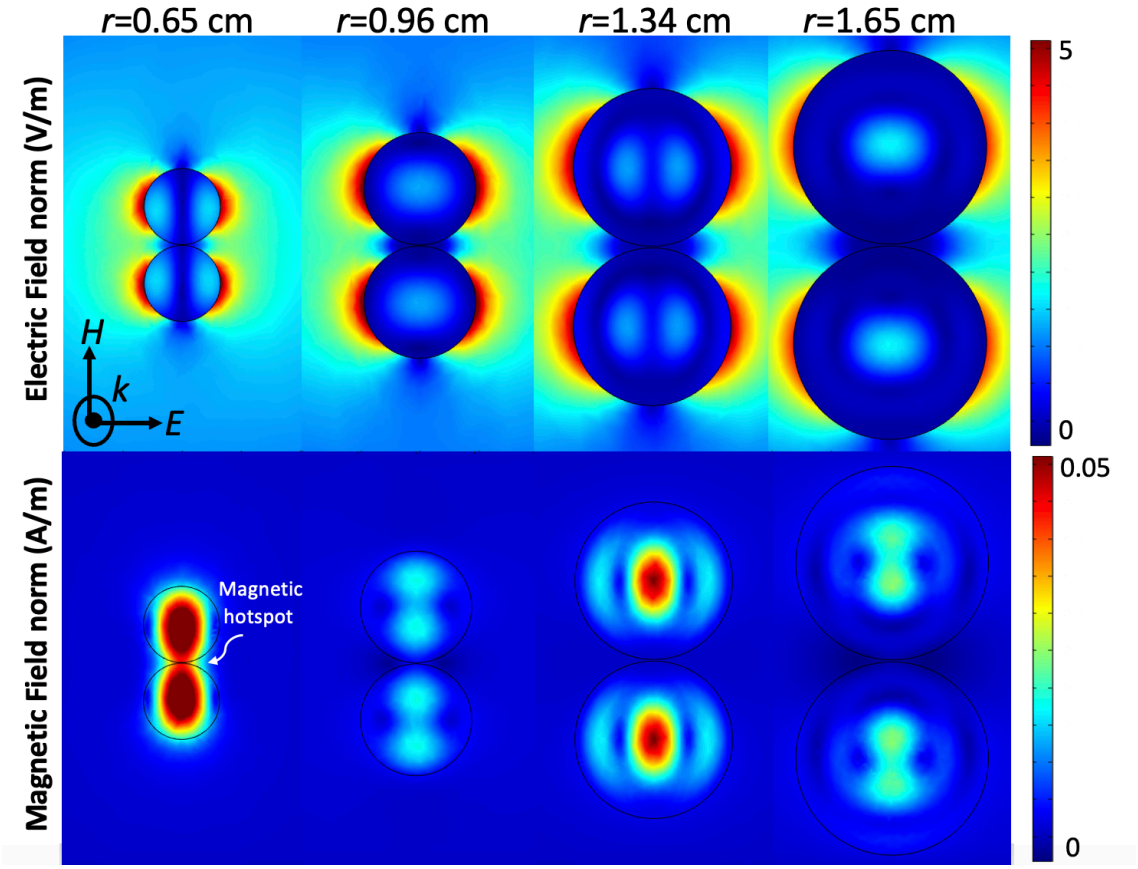

Figure 4.11. Simulated EM field norm maps at the *k*-*H* plane for the first four resonances in TrTr dimer; The colour scaling is consistent across all four magnetic field maps as well as all four electric field maps, although the scaling differs between the magnetic and electric maps.

Figure 4.11 displays the EM field norm maps for the TrTr dimer, on a cut plane perpendicular to the propagating direction. Similar investigations were conducted (by us) for other primary dimers and the monomer, allowing for a comparison of mode shape and field concentration within this dimer with others. Interestingly, no significant hotspots were observed in my simulations when irradiating this dimer at the microwave frequency in free space. However, studying its internal mode shape in comparison to others remains valuable. The simulated maps exhibit very similar internal modes to those observed in the monomer (as shown in Fig. 4.2), with minimal shape modifications and slight variations in field concentration intensity.

Our focus lies in exploring the dimer hotspots at the first four resonances for the three fundamental orientations and understanding how the hotspot intensity is influenced by the orientation. The following figure and table clearly demonstrate that the appearance and intensity of the hotspots are indeed dependent on the orientation.

Figure 4.12 presents the electric field norm maps for the first four modes of these three dimers. The color bars in the figures are scaled differently, indicating the strength of the hottest points in the maps.

Table 4.2. provides a comprehensive list of dimer geometries and resonances, clearly indicating which configurations exhibit magnetic/electric hotspots. Notably, magnetic-field axial hotspots are absent for all dimer orientations and resonances. For electric-field axial hotspots in this table, each entry is annotated as Intense (I), Moderate (M), Weak (W), or Non-existent (N).

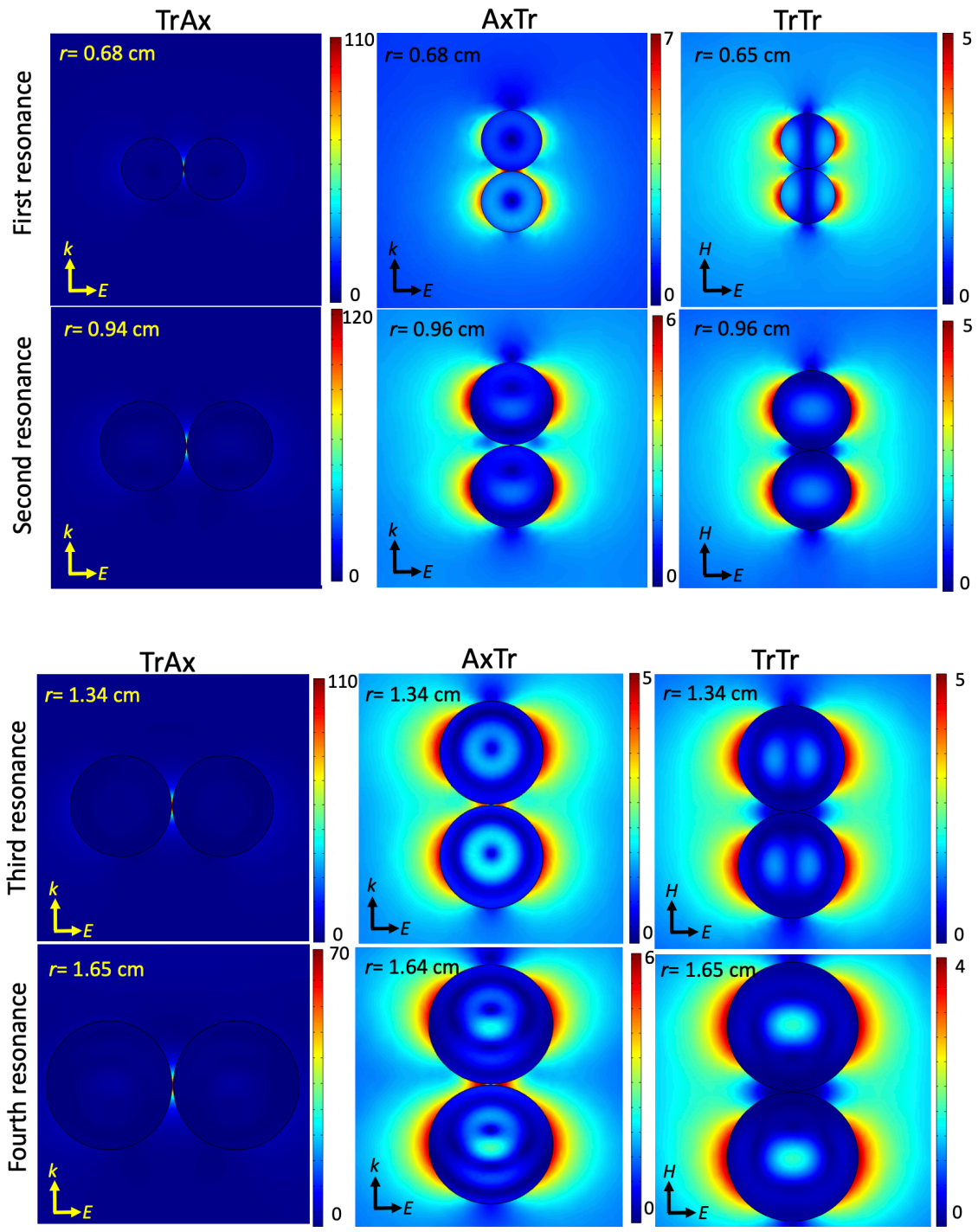

Figure 4.12. Simulated electric field norm maps depicting the first four resonances for three fundamental orientations (TrAx, AxTr, and TrTr). The maps emphasize the presence and intensity of axial hotspots. Notably, TrAx dimers exhibit strong electric axial hotspots at both resonances, AxTr dimers show a weak axial hotspot at the first resonance, and TrTr dimers do not display any electric hotspots at either resonance. The intensity of the hotspots is represented by the color bar alongside each map.

Table 4.2. Axial **electric** hotspot intensity based on dimer orientation and resonance. Quantitative visualization of these hotspots can be found in Fig. 4.12.

Dimer orientation	TrAx	AxTr	TrTr
First resonance	I	W	N
Second resonance	I	N	N
Third resonance	I	W	N
Fourth resonance	M	W	N

Based on Fig. 4.12 and Table 4.2, it is notable that in the TrAx dimer, the field is predominantly dominated by axial hotspots. Although the maps only depict the hotspots due to the concentrated field in these regions, it should be noted that the internal field exists within the spheres of these dimers, but it is overshadowed by the intense axial hotspot. Consequently, the TrAx dimer exhibits the most prominent **electric** axial hotspots at all four of the first resonances. On the other hand, the maps for the AxTr dimer show relatively weak **electric** axial hotspots at the first, third, and fourth resonances, while the TrTr dimer does not exhibit any hotspots within the first four resonances.

By comparing the internal energy of the three primary dimer orientations with those of the monomer, as shown in Fig. 4.13, I discovered that two of the dimers (TrAx and AxTr) have a similar resonant size/frequency as the monomer at the first mode. However, the TrTr dimer exhibits a slightly different resonant size/frequency at this mode, indicating that the TrTr magnetic-dipole mode happens at smaller sizes (i.e., smaller frequency; lower energy) than in the monomer. We also observed that the electric-dipole-like mode (second

resonance) is significantly more resonant in the TrAx dimer than it is in the monomer. Moreover, another shift in energy appears for the TrAx dimer at the second mode.

Additionally, Fig. 4.13 also reveals that in the AxTr dimer the internal energy density at the third resonance is higher than that at the second mode. This indicates a stronger resonance occurring at the third mode compared to the second mode in AxTr dimer. Analyzing the mode frequencies of the monomer and different dimers allows us to examine how dimerization impacts resonant behavior. The observed differences in resonances are intriguing because they suggest that resonance conditions vary depending on the dimer orientation.

In the analysis of dimer spectra, it is important to note that while mode shifts have been observed and comprehensively discussed in this study, the resolution of potential mode-splitting resulting from the dimerization of monomer modes presented a significant challenge. The intricacies of this phenomenon, if it exists, could not be fully resolved due to the complex nature of water bead structures and the limitations of the simulation tools employed. This aspect highlights a potential area for further investigation, possibly through refined experimental approaches and advanced simulation techniques, to gain deeper insights into the effects of mode-splitting in dimer configurations.

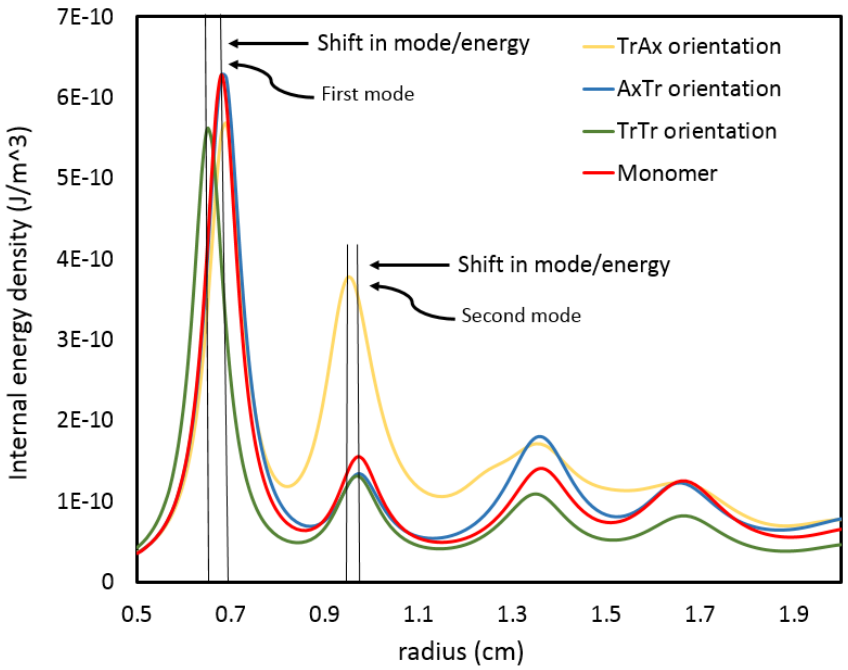

Figure 4.13. Comparison of internal resonances between the monomer and three fundamental dimer orientations. Resonant size shifts occur at the first mode for the TrTr dimer and at the second mode for the TrAx dimer. Additionally, the figure highlights the increased internal strength of the third mode in the AxTr dimer compared to its second mode.

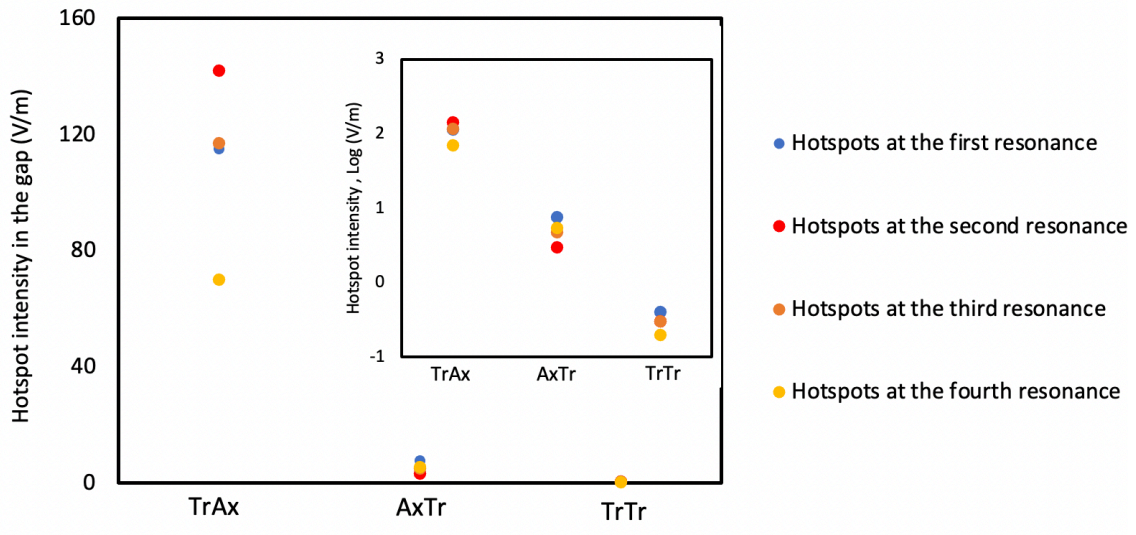

Figure 4.14. Presence and intensity of axial hotspots at the first four resonances for the three primary dimers. This is measured in the gap area, different from the internal energy in the objects. Inset: a rescaling of the figure with a logarithmic y-axis.

We observe distinct variations in dimerization among the three primary orientations for the lowest four modes/resonances. Certain modes in specific orientations exhibit no hotspots, such as the TrTr dimers for all the first four modes. Conversely, other modes and orientations display electric hotspots, such as the TrAx dimer for all the first four resonances and the AxTr dimer with weak hotspots in some select modes.

4-C) Intermediate dimer orientations

One of the primary objectives of my research is to explore whether the three fundamental orientations can be used as a basis set for intermediate orientations. This is important to us because we want to explore trimers as comprising dimers that are not always oriented at a fundamental geometry. Specifically, because we found that the three fundamental dimers are not identical in terms of their resonant behaviour and propensity for the formation of the axial hotspots, it motivates the study of intermediate orientations in terms of a superposition of fundamental dimer geometries so that we may understand and predict trimer and other cluster geometries.

In Fig. 4.15, I present a series of five intermediate dimer orientations between TrAx and AxTr. By incrementing the angle by 15-degree steps, I systematically moved from the TrAx dimer to the AxTr dimer. A commensurate investigation was carried out for the other primary dimer, TrTr. Specifically, I explored the transitions from AxTr to TrTr and from TrAx to TrTr, seeking to establish if there are interconnections between these transitions and if we can predict one based on the other two. This analysis will contribute to a deeper understanding of the underlying principles governing these geometries.

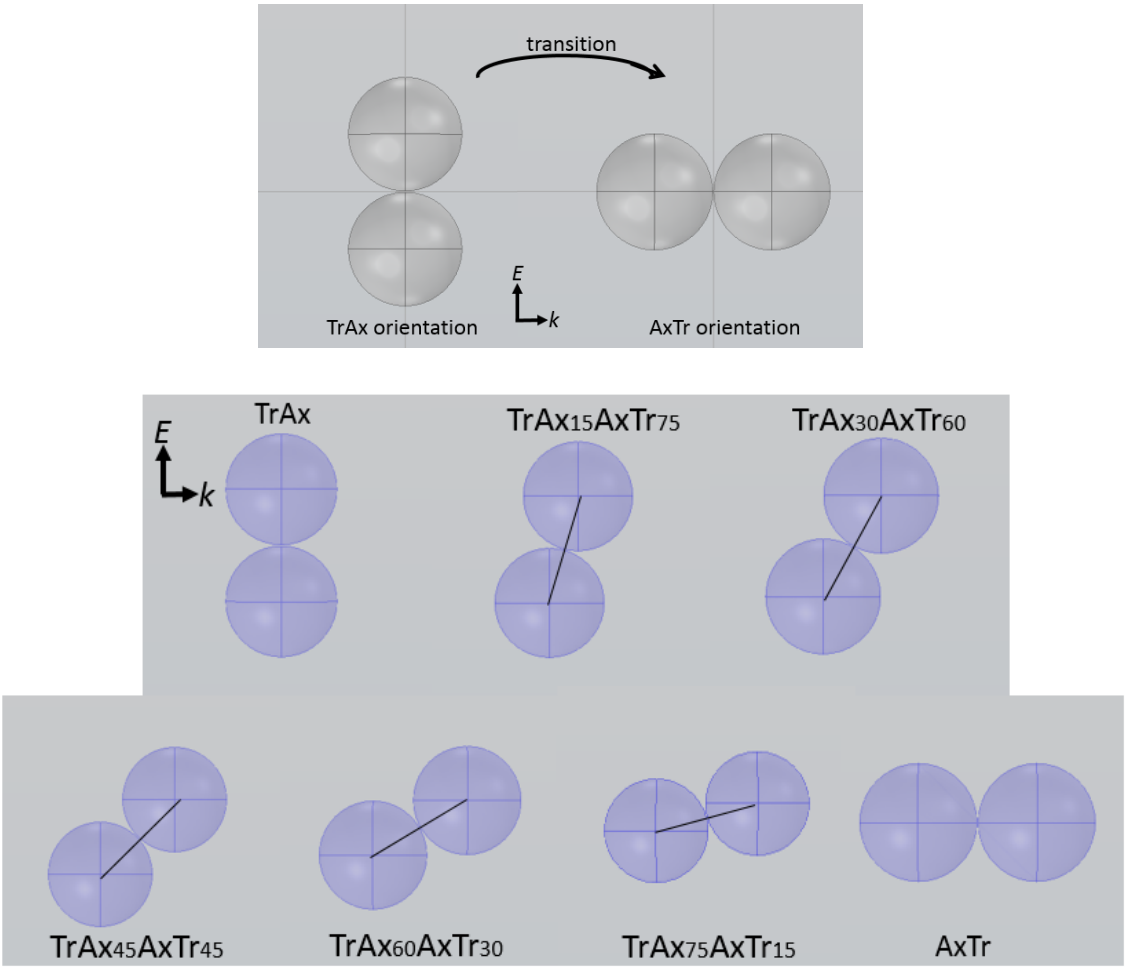

Figure 4.15. Transitional progression from TrAx dimer to AxTr dimer, showcasing intermediate dimer orientations with incremental changes (e.g., the $TrAx_{15}AxTr_{75}$ intermediate dimer represents a 15-degree rotation from TrAx to AxTr).

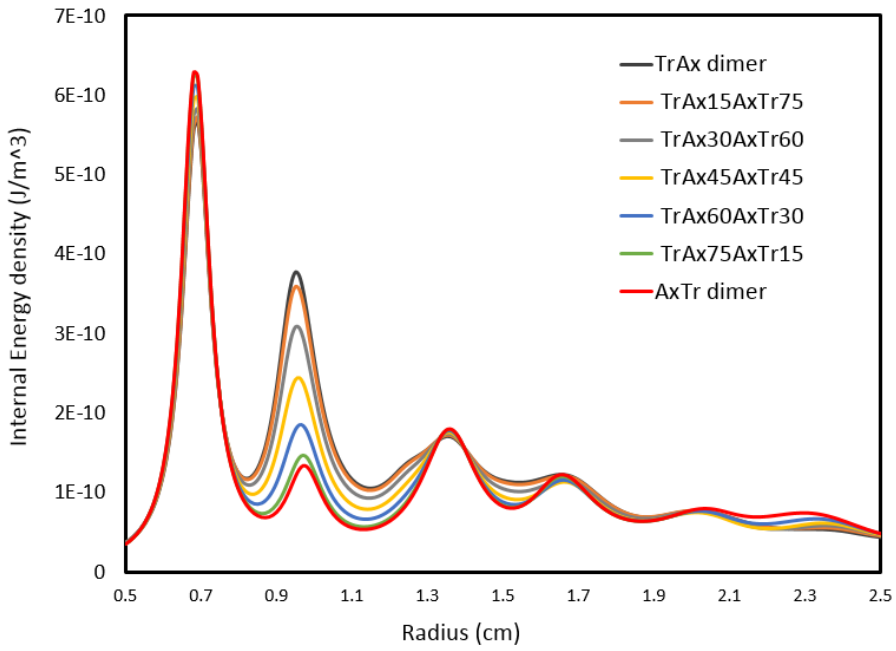

Figure 4.16. The Spectrum of internal resonances in intermediate dimer orientations from TrAx to AxTr.

The graph depicted in Fig. 4.17 illustrates the maximum electric field norm in the dimer gap for 7 orientations, including both primary and intermediate orientations, ranging from TrAx to AxTr at the first four resonances. The maximum electric field norm serves as a key parameter to measure and compare the strength of axial hotspots in dimers/trimers. By analyzing the electric field maps, we observe that all axial hotspots exhibit significant electrical intensity. This makes the maximum electric field norm an appropriate metric for quantifying hotspot strength (also the total EM energy analysis yields consistent results and can be considered as an alternative measurement parameter). The horizontal axis represents different orientations characterized by the rotation angle around the TrAx orientation, while the vertical axis represents the maximum electric field norm, indicative of hotspot intensity in the gap area.

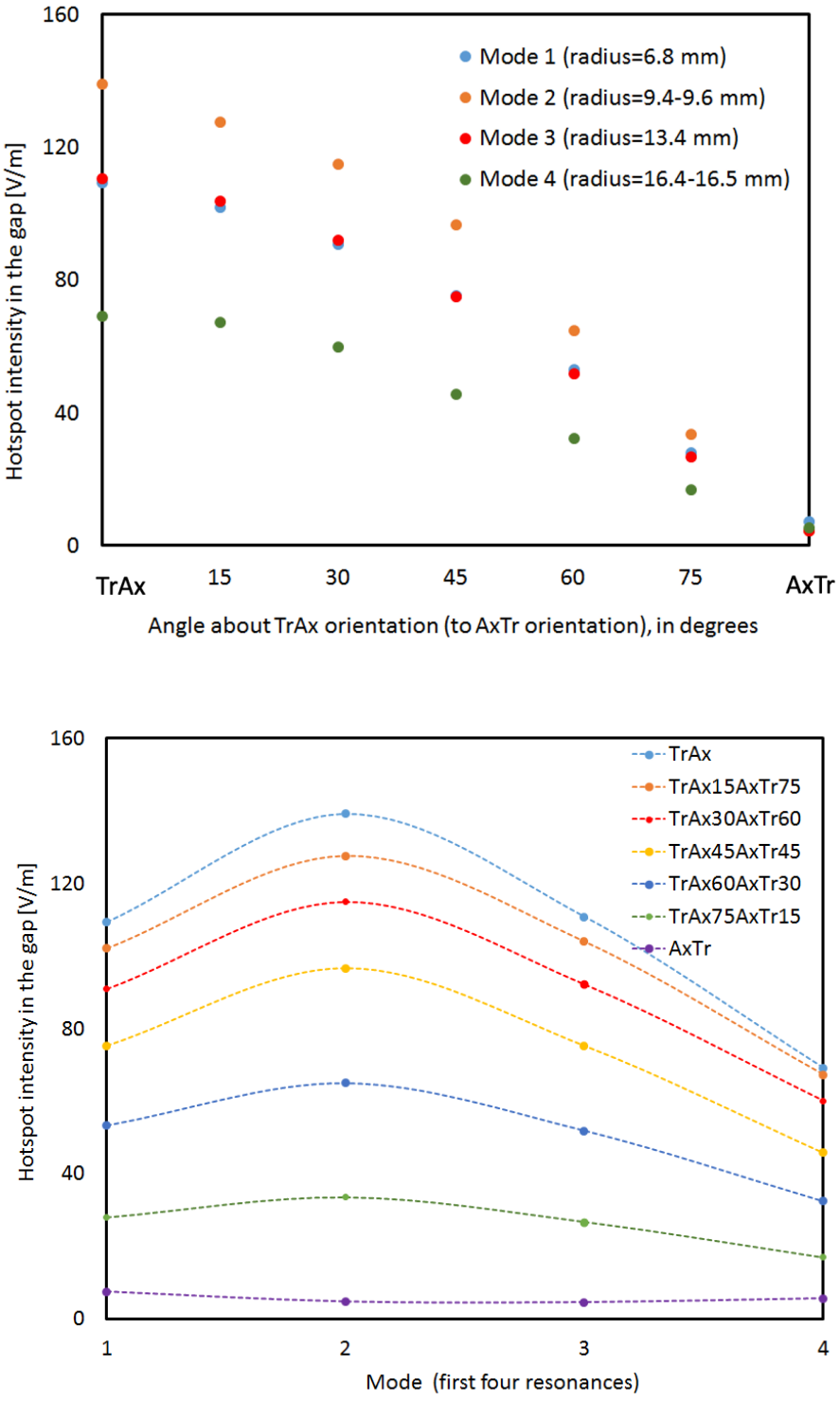

Figure 4.17. Dimer hotspot strength at the first four modes for orientations during the transition from TrAx dimer to AxTr dimer, with 15-degree increments.

Based on the findings depicted in Fig. 4.17, a notable observation is that the strongest hotspots are consistently observed at the second modes for all 7 dimer orientations from TrAx to AxTr. The graphs presented in this figure showcase the trend in hotspot intensity variations from the first mode to the fourth mode, as well as the trend in hotspot intensity changes while transitioning from TrAx dimer to AxTr dimer. It becomes apparent that TrAx dimers exhibit the most intense hotspots across all modes, confirming our notion that it is a 'fundamental' orientation. That is, no intermediate orientation displays a more intense hotspot.

Furthermore, by analyzing the graphs representing hotspot intensity for all four modes, we can discern a smooth and monotonic trend during the conversion from TrAx dimer to AxTr dimer. Interestingly, all seven orientations exhibit a peak hotspot intensity at their respective second modes. However, it is worth noting that the hotspot intensity of TrAx dimers surpasses that of the other orientations across all modes. These observations provide valuable insights into the trend of hotspot intensity changes during the conversion process from TrAx dimer to AxTr dimer, highlighting the consistent prominence of hotspots in TrAx dimers throughout the modes.

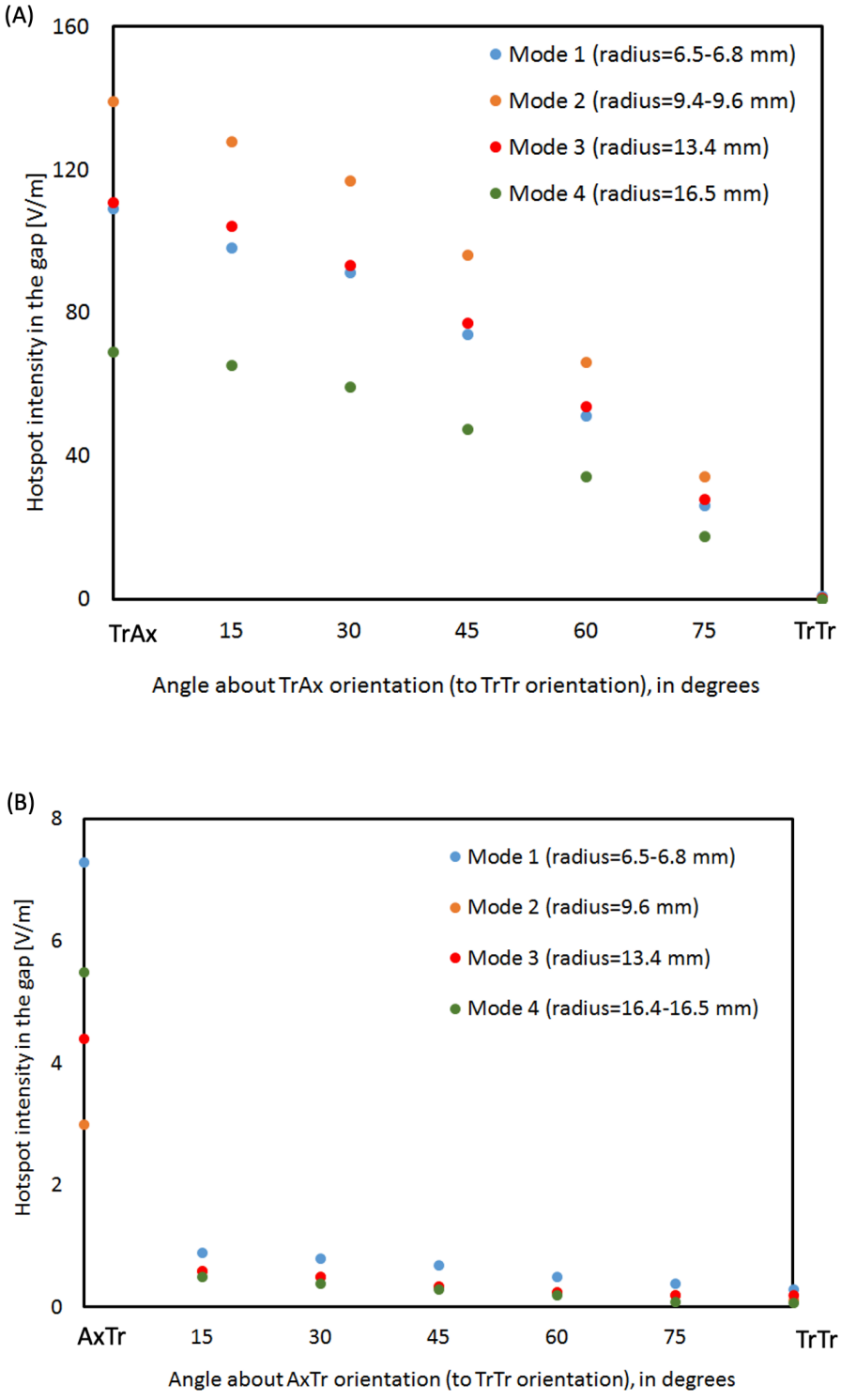

Figure 4.18. Hotspot intensity graphs at the first four modes for all orientations (primary and intermediate) during two primary transitions: (A): TrAx to TrTr, and (B): AxTr to TrTr. The transitions are shown with 15-degree increment steps.

Figure 4.18(B) presents remarkable data showcasing the rapid disappearance of the hotspot during the transition from AxTr to TrTr. This observation strongly implies that these hotspots are very sensitive to orientation. For practical applications that utilize these axial hotspots, precise alignment of the dimers or careful control of polarization becomes essential. The unexpected and significant nature of this finding justifies further exploration and consideration in the context of potential applications. Now, returning to the overall analysis of the graphs in Figs. 4.17 and 4.18, they consistently demonstrate that while the dimer hotspots strongly depend on orientation, smooth transitions between fundamental dimer orientations consistently show clear trends in hotspot behavior. These trends also confirm that maximum hotspot intensity is always found at one of the primary alignments and not at an intermediate orientation.

4-C-1) Internal mode twisting in dimers

To explore the potential interaction between dimers in the formation of a trimer, an additional approach involves comparing the internal mode shapes and orientations. By systematically rotating a dimer from one primary dimer orientation to another, the shape of field concentration **inside** the dimer also undergoes a corresponding rotation. However, at a certain intermediate orientation, an intriguing phenomenon occurs; the internal mode either ceases to rotate or exhibits a different angle of rotation compared to the axial angle of the dimer. We refer to this phenomenon as "internal mode twisting". While we do not yet know the cause of this effect, nor its significance, by observing the changes in the mode shapes and orientations, we hope to gain a deeper understanding of the interplay between the constituent dimers of a trimer and how they contribute to the unique properties of the trimer system.

Figure 4.19 illustrates the concept of internal mode twisting through an example of an intermediate dimer. The figure provides a comparison between the physical rotation of a dimer and the corresponding rotation of the internal mode. The dimer orientation for this intermediate dimer is rotated by 15 degrees from TrAx. Upon examination, we observe that the internal mode rotates by less than 15 degrees, indicating a "twisted" internal mode.

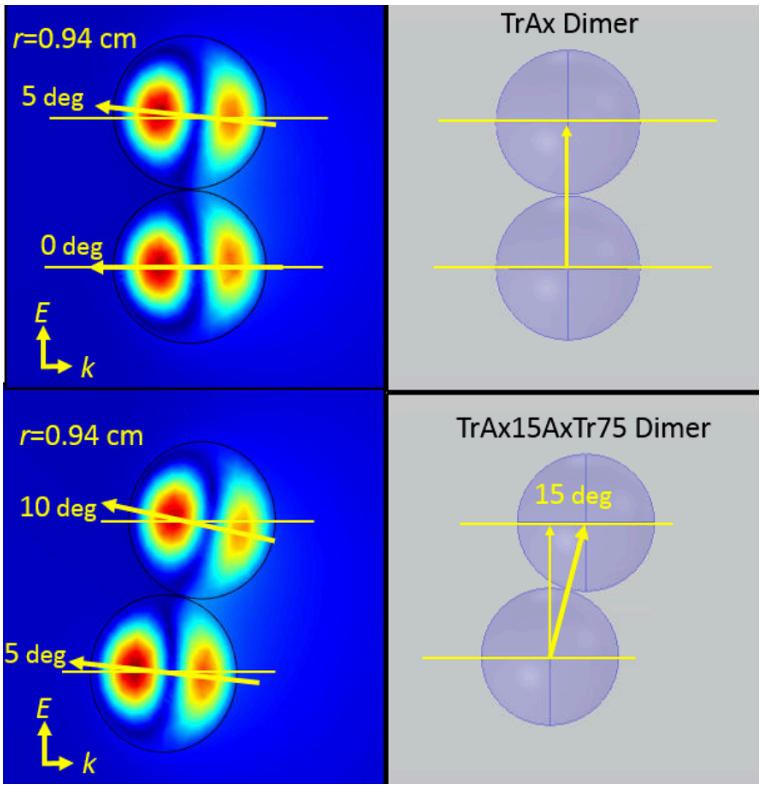

Figure 4.19. Magnetic field mode twisting example in$TrAx_{15}AxTr_{75}$ intermediate dimer with a 15-degree rotation around the TrAx orientation at the second resonance.

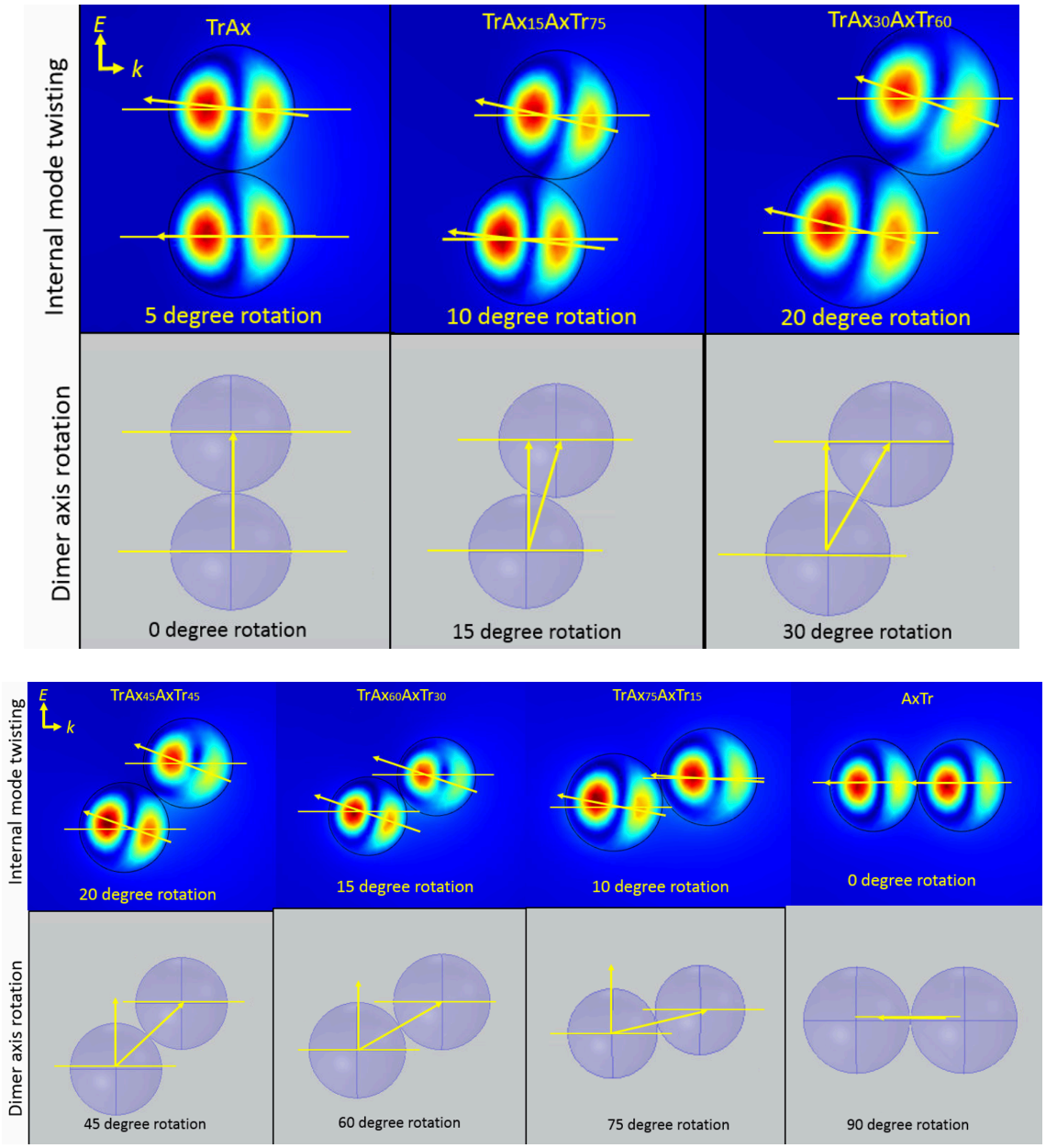

Figure 4.20. Magnetic field mode twisting in a dimer during rotation from TrAx to AxTr orientation. The figure illustrates the progression of the internal mode rotation alongside dimer axis rotation. Initially, the mode rotates in sync with the dimer axis for the first two steps, but with a lag. At the third step, the internal mode ceases rotation, and from that point onward, it undergoes a counter-rotation to return to its initial position, deviating from the trend of dimer axis rotation.

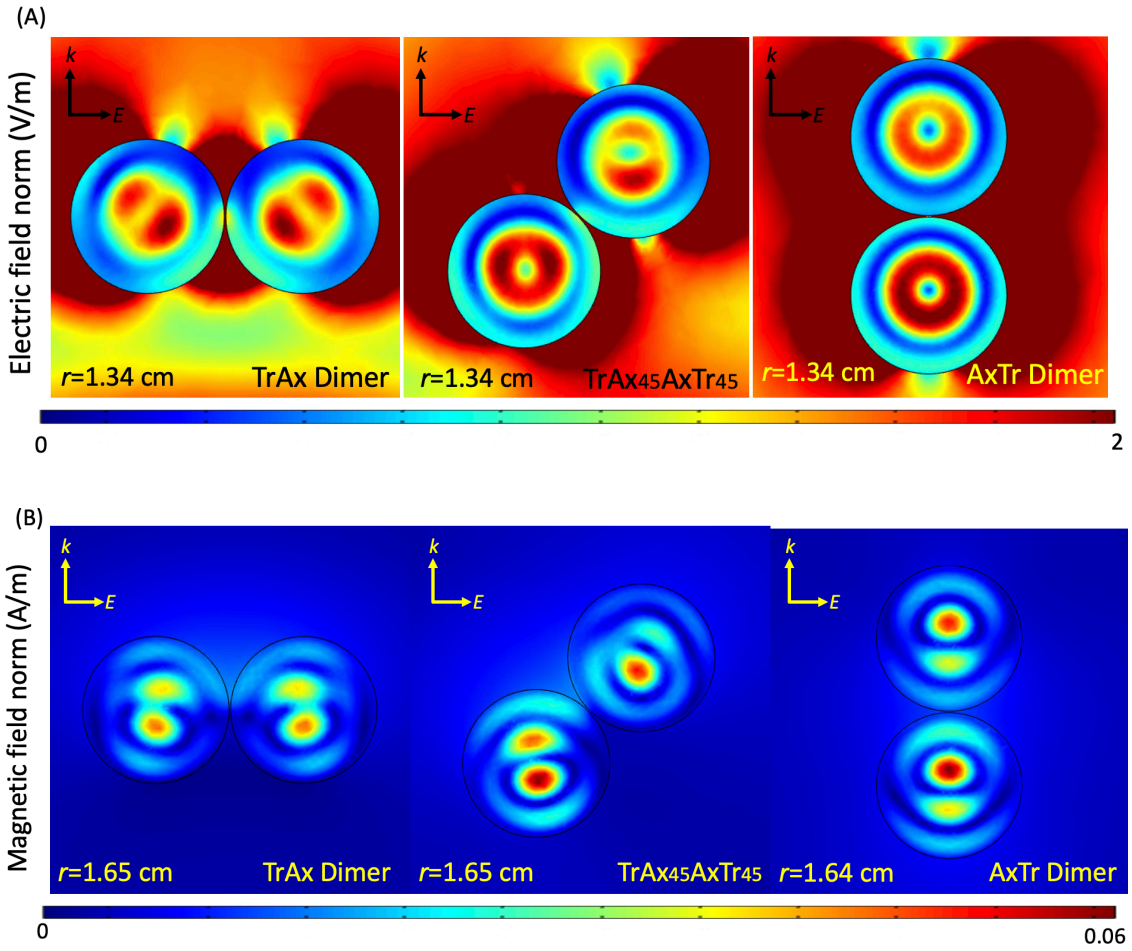

Figure 4.21. Simulated electromagnetic field norm maps on the *k*-*E* equatorial cut plane illustrating the internal field shape and concentration of the TrAx45AxTr45 intermediate dimer, compared to the primary TrAx and AxTr dimers. (A): Electric field norm maps at the third mode (magnetic quadruple mode). (B): Magnetic field norm map at the fourth mode (electric quadruple mode).

In Figs. 4.21, 4.22, and 4.23, a series of electromagnetic field maps are presented, illustrating the behavior of an intermediate dimer, the intermediate dimer with a 45-degree rotation from two primary dimers, at the first four resonances. These maps offer valuable insights into how the field concentration, shapes, and internal mode characteristics evolve during the transition from one primary dimer to another.

By examining these maps, we can assess any modifications in the internal mode shape and observe if the intermediate dimer exhibits a twisted internal field compared to its primary counterparts. Furthermore, these maps provide a means to gauge the relative strength of the fields inside the intermediate dimer compared to the primary dimers. To facilitate such comparison, the color bars in each set of maps are consistently scaled, allowing for an accurate assessment of the internal field intensity (we did not want to consider the dimer hotspots here). Additionally, all maps in each set of maps are captured on the same study cut plane, enabling comprehensive analysis and comparison of the mode shapes.

The maps presented in Fig. 4.21 highlight significant modifications in the internal mode shape of the intermediate dimer as we transition from the TrAx dimer to the AxTr dimer. In the AxTr dimer, the axes of the internal fields in both spheres are similarly oriented, while in the TrAx dimer, we observe symmetry in the internal field shape within each sphere of the dimer. However, in the intermediate dimer, we observe distinct field shapes inside the spheres, indicating a twisting of the internal mode shape at different angles within each sphere compared to the 45-degree rotation from TrAx to AxTr. This twisting and shape modification of the modes demonstrates that water beads interact differently when forming different dimers. Additionally, the field concentration within the intermediate dimer is not symmetric, as the dimer axis is not perpendicular to the propagating direction. As a result, the field inside one of the spheres is (slightly) stronger than the field inside the other sphere of this dimer.

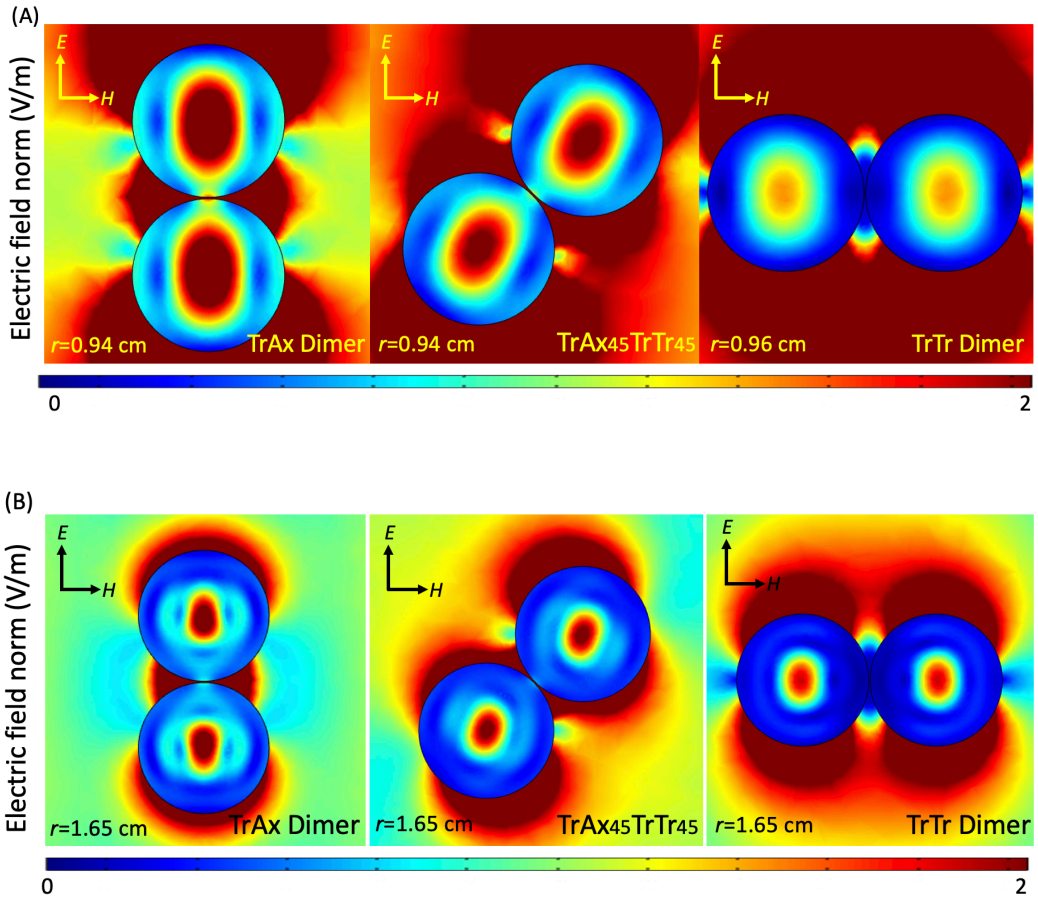

Figure 4.22. Simulated electromagnetic field norm maps on the *E-H* equatorial cut plane illustrating the internal field shape and concentration of the $TrAx_{45}TrTr_{45}$ intermediate dimer, compared to the primary TrAx and TrTr dimers. (A): Electric field norm maps at the second mode. (B): Electric field norm map at the fourth mode.

Figure 4.22 presents a series of maps that explore the internal field of another intermediate dimer, $TrAx_{45}TrTr_{45}$, during the transition from the TrAx dimer to the TrTr dimer. Although axial hotspots are present at all the first four resonances, the primary focus of these maps is not on investigating the hotspots. Rather, they are intended to study the internal modes, which is why the color bar scale is kept consistent. The same scale maps make it possible to capture the internal mode shapes even with the presence of very strong axial hotspots. The maps reveal symmetric field concentrations due to the dimer axis being

perpendicular to the propagating direction, *k*. This symmetry leads to equal field strengths in both spheres of these dimers. In terms of mode shapes, the field shapes are symmetric in both the TrAx and TrTr dimers. For the $TrAx_{45}TrTr_{45}$ dimer, I observed a less pronounced modification in the field shape compared to TrAx and TrTr dimers. The internal mode in this dimer appears to exhibit a rotation effect with the same angle as the dimer rotation angle which is 45 degrees for this intermediate dimer.

Lastly, I present the electromagnetic field maps for another intermediate dimer with a 45-degree rotation in the transition between the other two primary dimers. Figure 4.23 displays the maps that compare the $AxTr_{45}TrTr_{45}$ dimer with the AxTr and TrTr primary dimers. Similar to the observations made in Fig. 4.21, these maps show shape modifications and field twisting within the spheres of the $AxTr_{45}TrTr_{45}$ dimer in comparison to the AxTr and TrTr dimers. We have differently oriented mode shapes in each sphere of this intermediate dimer.

Additionally, the field concentration within the $AxTr_{45}TrTr_{45}$ dimer is not symmetric, similar to the AxTr dimer, indicating that the field is stronger in the bottom sphere compared to the top sphere. However, in the TrTr dimer, the field strength is symmetric since the dimer axis is perpendicular to the propagating direction, *k*, for this particular dimer.

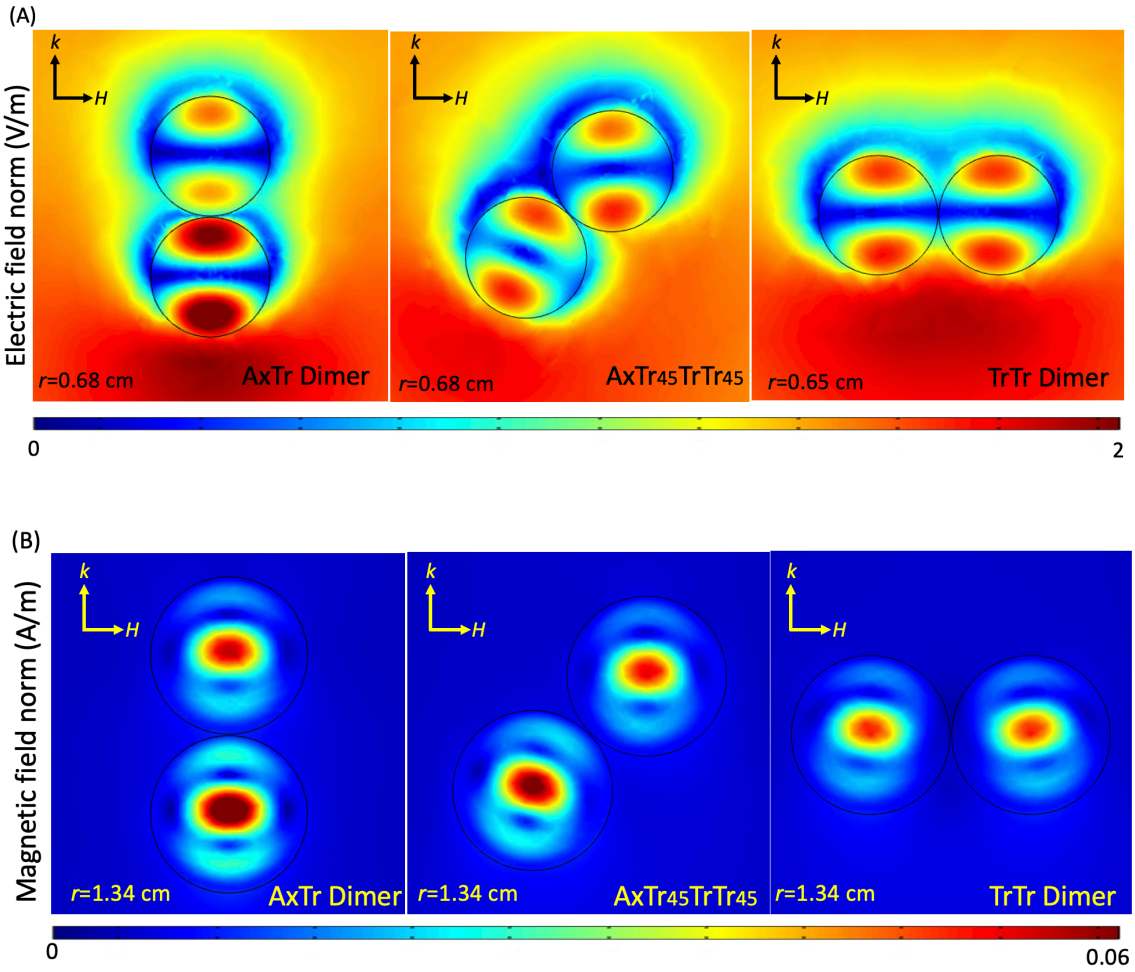

Figure 4.23. Simulated electromagnetic field norm maps on the *k-H* equatorial cut plane illustrating the internal field shape and concentration of the $AxTr_{45}TrTr_{45}$ intermediate dimer, compared to the primary AxTr and TrTr dimers. (A): Electric field norm maps at the first mode. (B): Magnetic field norm map at the third mode.

Figures 4.21 to 4.23 provide examples of twisted internal modes, showcasing significant changes in the internal mode shape as we transition between primary dimers. In the AxTr primary dimer, the internal modes in both spheres are similarly shaped while the TrAx and TrTr primary dimers demonstrate internal mode shape symmetry within their spheres. This observation holds true across all resonances. However, in certain intermediate dimers, distinct field shapes are observed within each sphere. For instance, in the $TrAx_{45}AxTr_{45}$

dimer (Fig. 4.21), the field shapes exhibit different orientations within each sphere, differing from both AxTr and TrAx dimers and indicating a twisting of the internal mode shape at different angles within each sphere, compared to the 45-degree rotation from TrAx to AxTr. In contrast, an intermediate dimer like $TrAx_{45}TrTr_{45}$ (Fig. 4.22) exhibits similar rotation of the internal mode in both spheres, aligned with the dimer axis rotation angle of 45 degrees. Therefore, this specific intermediate dimer does not display a twisted internal mode. Conversely, in cases such as the $AxTr_{45}TrTr_{45}$ intermediate dimer (Fig. 4.23), one sphere showcases a different angle of internal mode rotation compared to the dimer axis rotation, while the mode shape remains unrotated within the other sphere. This exemplifies an internal mode twisting phenomenon that occurs differently within each sphere of the intermediate dimer.

In the Fig. 4.24, I provide all the electric and magnetic field maps corresponding to the first four modes in a single master figure. This comprehensive visualization serves the purpose of summarizing our findings in a unified manner and facilitating a comparative analysis of the internal mode shapes and the presence or absence of hotspots among the three primary dimers alongside the monomer, across all modes.

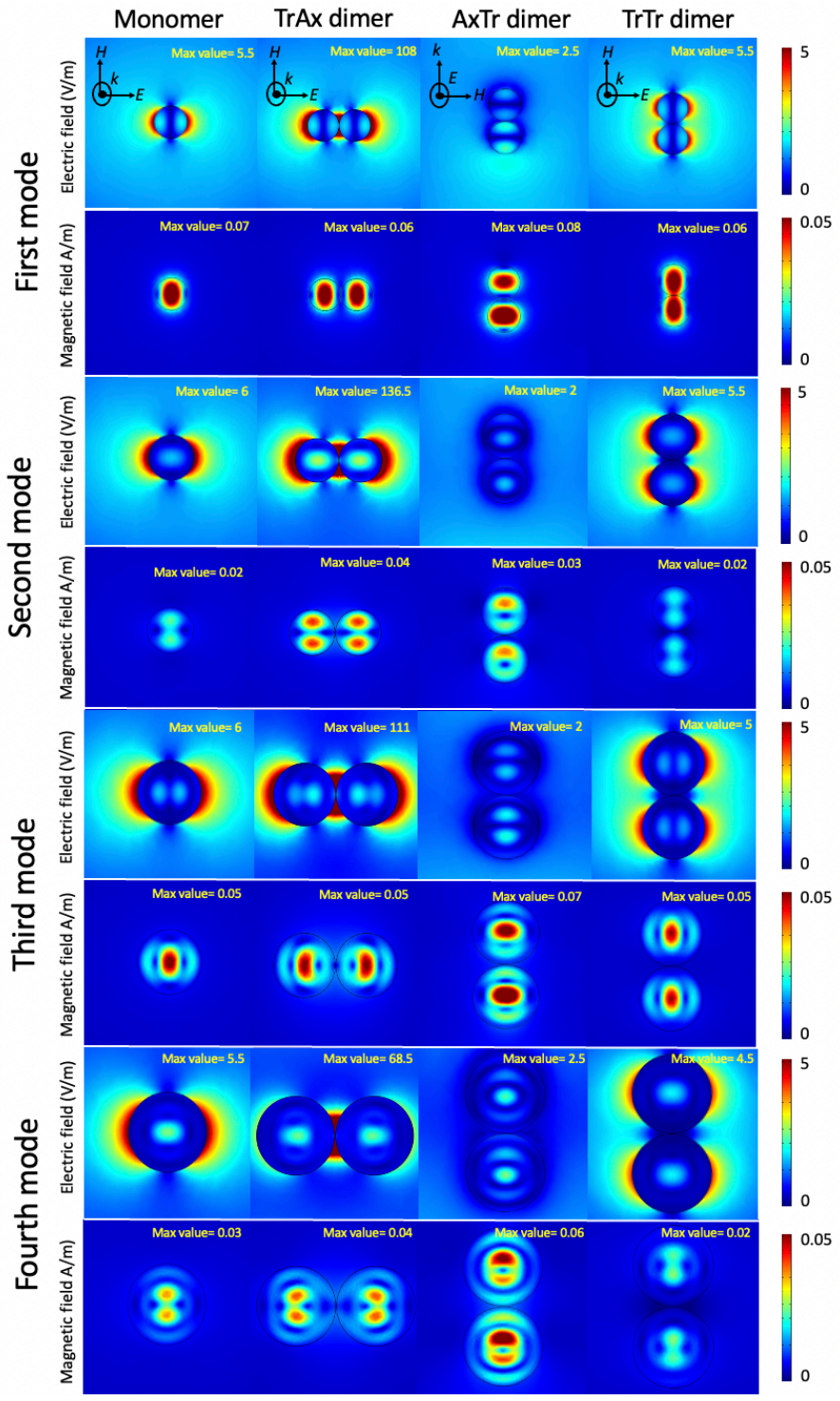

Figure 4.24. A summary master figure showing the electric and magnetic field modes in the monomer and the three primary dimer orientations at the first four resonances. The colour bar scale for each sequence and field mode has been made the same, and the maximum intensity of each panel is labeled in yellow to allow for comparisons of hotspot intensities.

4-D) Trimers as dimer clusters

In this section, I delve into the topic of cluster geometry and explore various trimer models. I examine the hotspot intensity and appearance in trimers, comparing them to those observed in dimers. I also look for a hotspot located at the trimer center, or “nexus”, as a sign of the dimer interactions within a trimer. Additionally, I discuss the phenomenon of mode twisting in trimer geometries. By delving deeper into these aspects, we hope to gain a better understanding of the dynamics and characteristics of cluster formations.

As defined in the Methodology chapter, our trimer is a combination of three water-based spheres arranged on a plane, conceptualized as being composed of three dimers on this plane. A key aspect of our investigation is to determine if trimers exhibit features that distinguish them from dimers. Just as dimers possess a unique feature not found in monomers (i.e., the axial hotspot), we aim to explore whether trimers also showcase a distinct hotspot, potentially located at the trimer center. This leads to the central question of my thesis: Does a trimer exhibit a novel hotspot, such as a nexus hotspot, that is not observed in dimers? If trimers indeed possess such unique features, they will signify that a trimer is not simply the sum of three individual dimer groups, much like we have shown that a dimer is more than a simple combination of monomers.

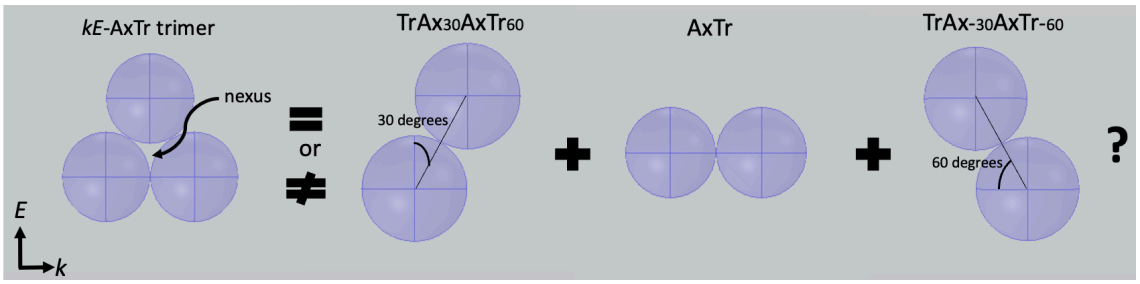

Figure 4.25. An example trimer geometry, *kE*-AxTr trimer: A composition of three dimer groups on the *k*-*E* plane, that incorporates the AxTr dimer. Investigating whether this trimer is merely an aggregation of the three individual dimers or exhibits distinct characteristics.

The *kE*-AxTr trimer shown in Fig. 4.25 exemplifies one possible trimer geometry. It can be conceptually visualized as consisting of three dimers; one positioned at the AxTr orientation, and the other two representing intermediate dimers between TrAx and TrTr orientations. Specifically, one intermediate dimer is oriented at a 30-degree rotation about the TrAx orientation, while the other intermediate dimer is positioned with a 60-degree rotation about the AxTr orientation.

So far, our findings indicate that while monomers do not exhibit external hotspots when resonant, at certain orientations axial dimer hotspots can form at the resonances of monomers. However, upon studying trimers at the resonances of dimers and monomers, we do not identify any new hotspots at the trimer nexus. In Fig. 4.26, an analysis of the total energy density at the nexus of the *kE*-AxTr trimer was conducted by examining the averaged EM energy as a function of size. A cylindrical volume was defined within the nexus with a radius of *r*/6 and a height of *r*/6 to collect the average EM energy. In a coarse mesh, when the trimer is with a radius equal to 1 cm, each sphere of this trimer contains 3775 (tetrahedral) elements and this cylindrical volume located in the nexus contains 199 elements. This figure presents a comparison between these resonances and the internal

resonances within the trimer to assess if they exhibit similar spectra. However, notable differences were observed between the spectra of the energy density at the nexus and the energy density inside the trimer itself.

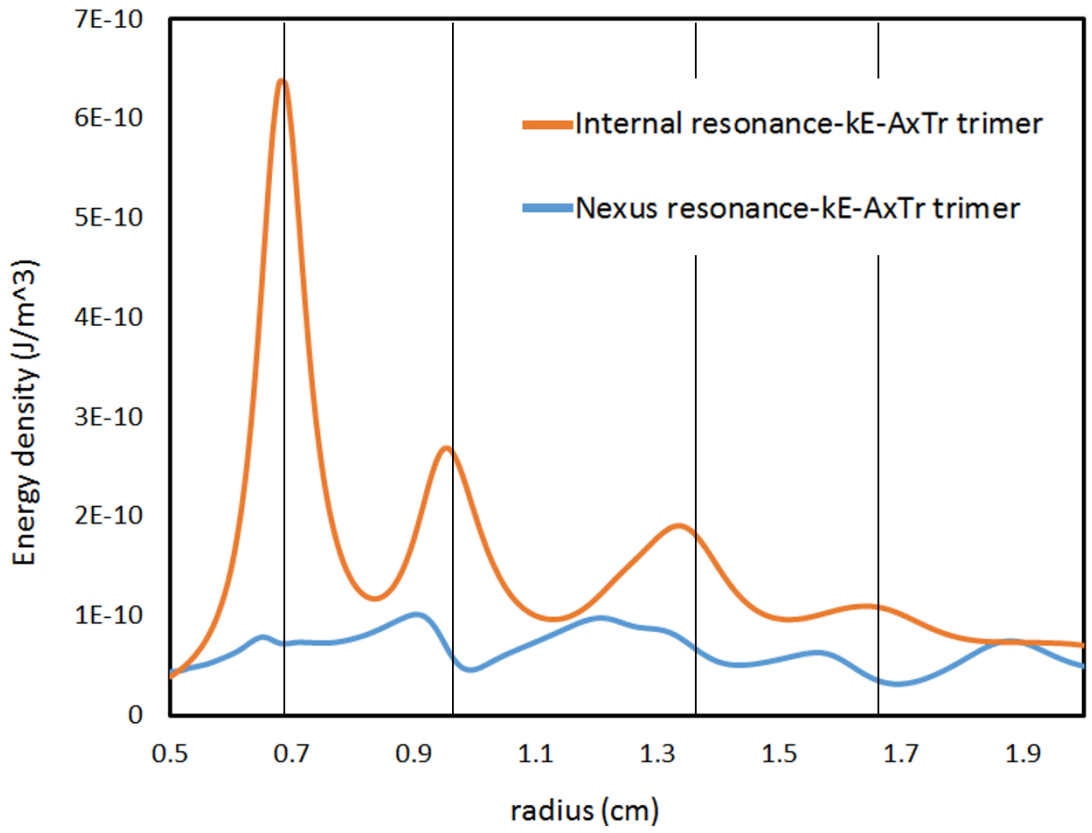

Figure 4.26. Comparison of EM energy density within the *kE*-AxTr trimer and at its nexus. While resonant behaviour is observed at the nexus, it does not align with the internal EM energy spectrum. The vertical lines represent the peak locations for the isolated (monomer) MDRs.

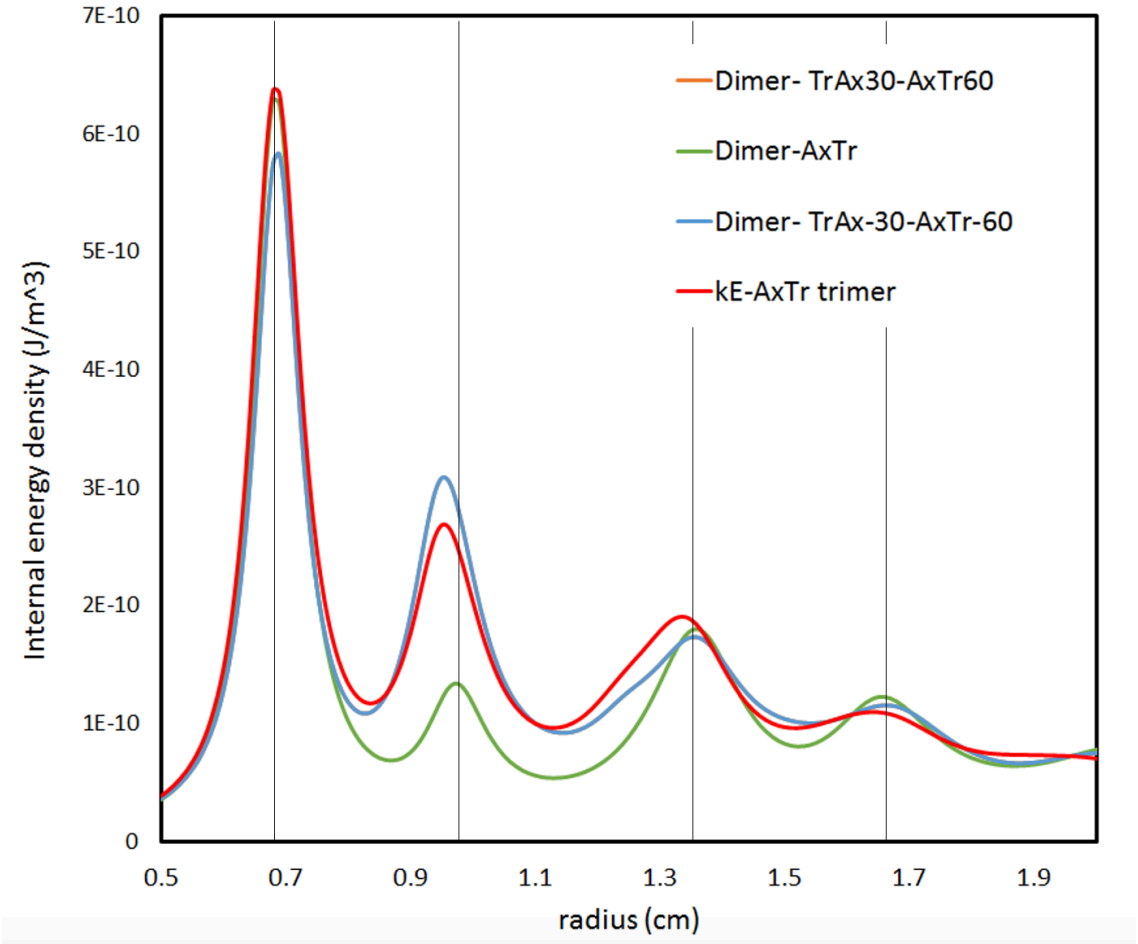

Figure 4.27. Comparison of the internal EM energy density spectrum between the *kE*-AxTr trimer and the constituent isolated dimers. The spectrum showcases internal resonances within the *kE*-AxTr trimer, indicated by vertical lines representing the first four monomer resonances.

Based on Fig. 4.27, slight variations in resonant size and energy are observed for the trimer compared to the isolated dimers, particularly at the second, third, and fourth resonances. In the *kE*-AxTr trimer, the second resonance occurs at 0.94 cm same as in the $TrAx_{30}AxTr_{60}$ and $TrAx_{-30}AxTr_{-60}$ intermediate dimers, while the second resonant size is 0.96 cm for the AxTr dimer which means different resonant frequency/energy we have for the trimer and its constituent dimers. Furthermore, small energy shifts are observed in the trimer at the

third and fourth resonances. The third resonant size is 1.32 cm for the trimer, whereas it is 1.34 cm for the isolated dimers. Similarly, the fourth resonant size is 1.65 cm for the two intermediate dimers, whereas it is 1.64 cm for the AxTr dimer and trimer. These energy shifts and comparisons between the trimer and its isolated dimer constituents demonstrate slight differences in the resonant behavior of the trimer and some subtle interaction of dimers when they come together to create a trimer. However, the trimer resonant sizes are closely related to the three isolated dimers, suggesting that the trimer is essentially composed of these constituent dimers.

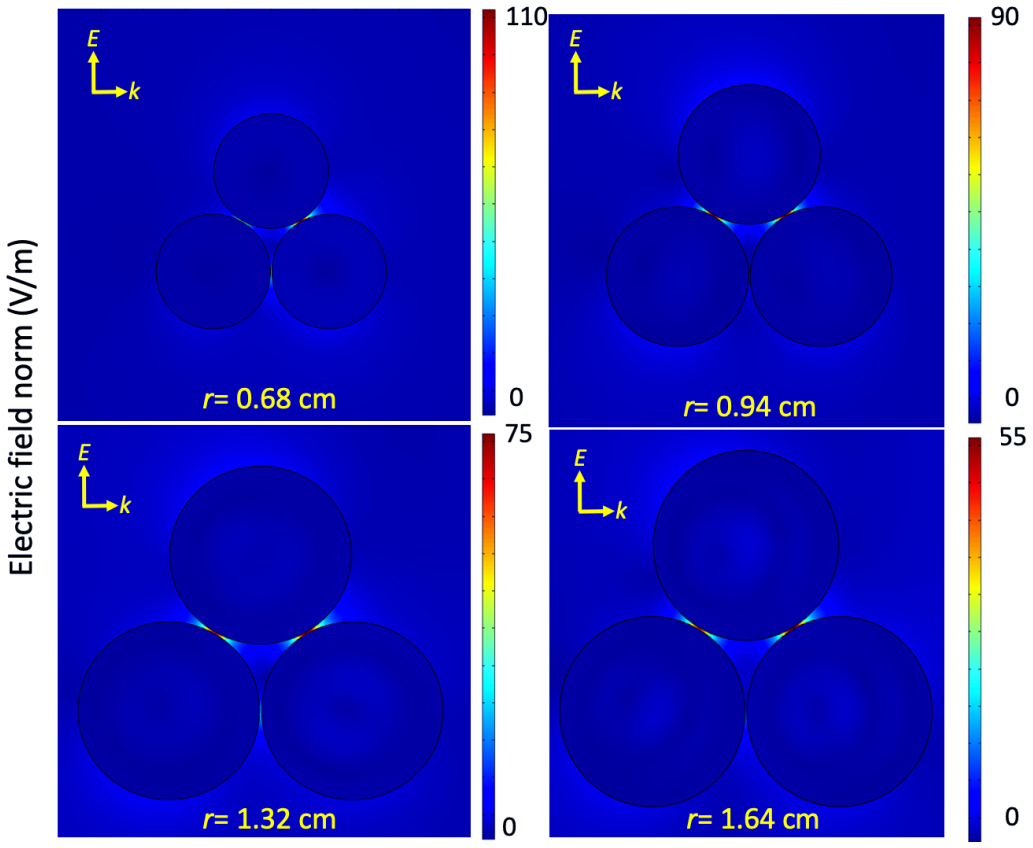

Figure 4.28. Electric field norm maps for the *kE*-AxTr trimer at the first four resonances, illustrating the distribution and intensity of trimer hotspots at each resonance. (Only axial hotspots are observed. There is no identifiable hotspot at the trimer nexus.)

At the first resonance of the trimer, one strong hotspot and two medium hotspots are observed. The second resonance exhibits two equally strong hotspots. Moving to the third, two relatively strong hotspots and one weaker hotspot are observed. Finally, the fourth resonance shows two medium hotspots. The color bars in the maps are scaled differently to indicate the intensity of the hotspots, enabling a comparison of hotspot intensity across different modes. Notably, the presence of strong axial hotspots dominates the field, limiting the visibility of internal fields within the spheres. Instead, the maps highlight how the trimer hotspots prevail at the points of contact between each pair of spheres within the trimer.

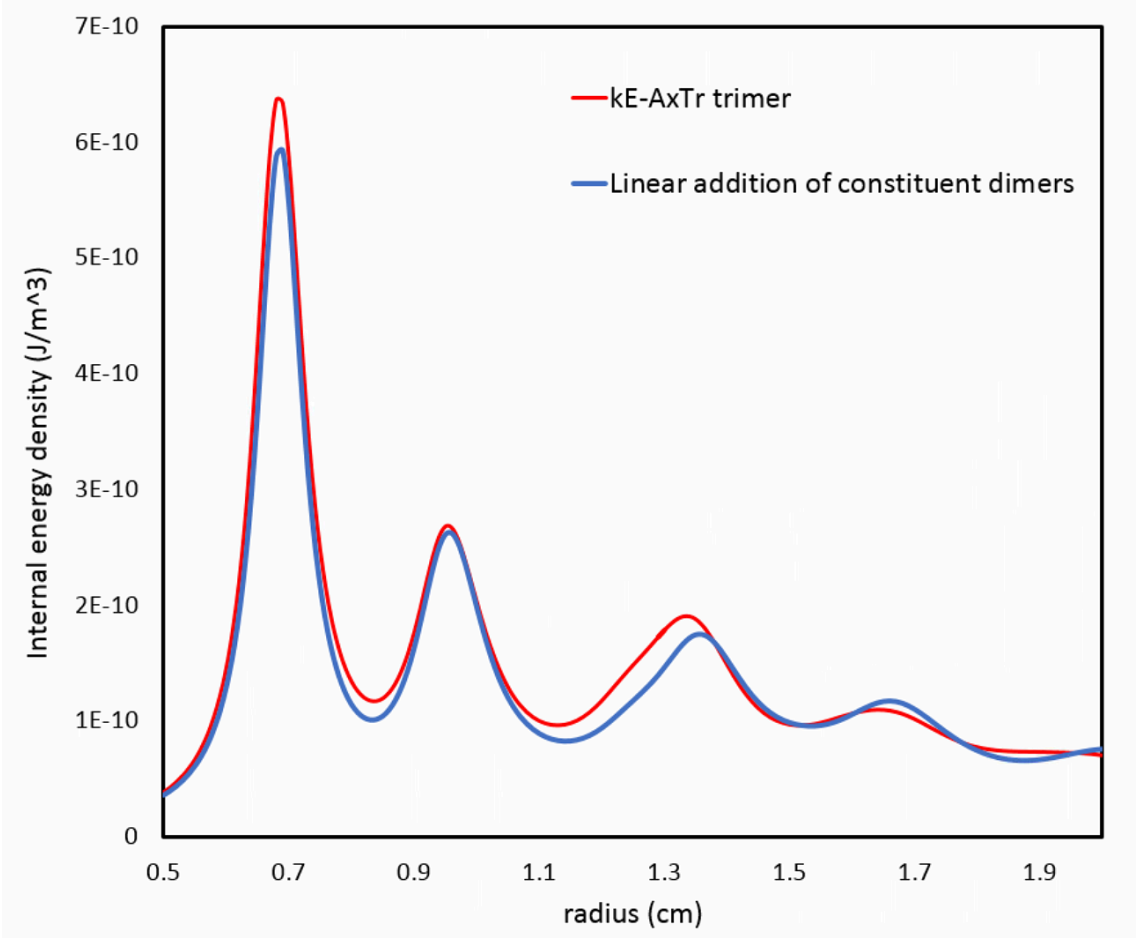

Figure 4.29. Comparison of the EM energy density spectrum between the *kE*-AxTr trimer and the recreated spectrum obtained by adding the EM energy from the constituent isolated dimers. The recreated spectrum closely matches the internal resonances of the *kE*-AxTr trimer, demonstrating that the combined EM energy densities of the isolated dimers successfully approximate the spectrum of the trimer.

To investigate the trimer as a combination of dimers, a simple linear combination approach was employed. The internal electromagnetic energy densities of the three constituent dimers in the *kE*-AxTr trimer were summed to recreate its spectrum. Equal weights were assigned to the two intermediate dimers (each 1/4), while the AxTr dimer was assigned a unique weight (1/2). This recreated spectrum, illustrated in Fig. 4.29, exhibits a close correspondence with the internal resonances observed in the *kE*-AxTr trimer. These

findings demonstrate that the combined EM energy densities of the isolated dimers effectively approximate the spectrum of the trimer.

Overall, my findings from Figs. 4.28 and 4.29 indicate that a trimer is not fundamentally distinct from a combination of dimers. Rather, a trimer can be understood as an interactive system composed of three interconnected dimers. However, the interactions between these dimers can be described as relatively straightforward. Essentially, a trimer can be viewed as a composition of three individual dimers arranged in different orientations with variations in hotspot strengths and internal mode orientations. Consequently, while a trimer can be considered as a combination of three dimers, the intensity trends of the hotspots themselves do not necessarily align with those observed in the individual dimers.

To fully analyze the characteristics of a trimer, it is essential to investigate the three individual dimer groups comprising the trimer and compare their respective hotspots to those observed within the trimer itself. Through my simulations, no conclusive evidence of a new hotspot located at the trimer nexus has been observed at any sizes and trimer planes.

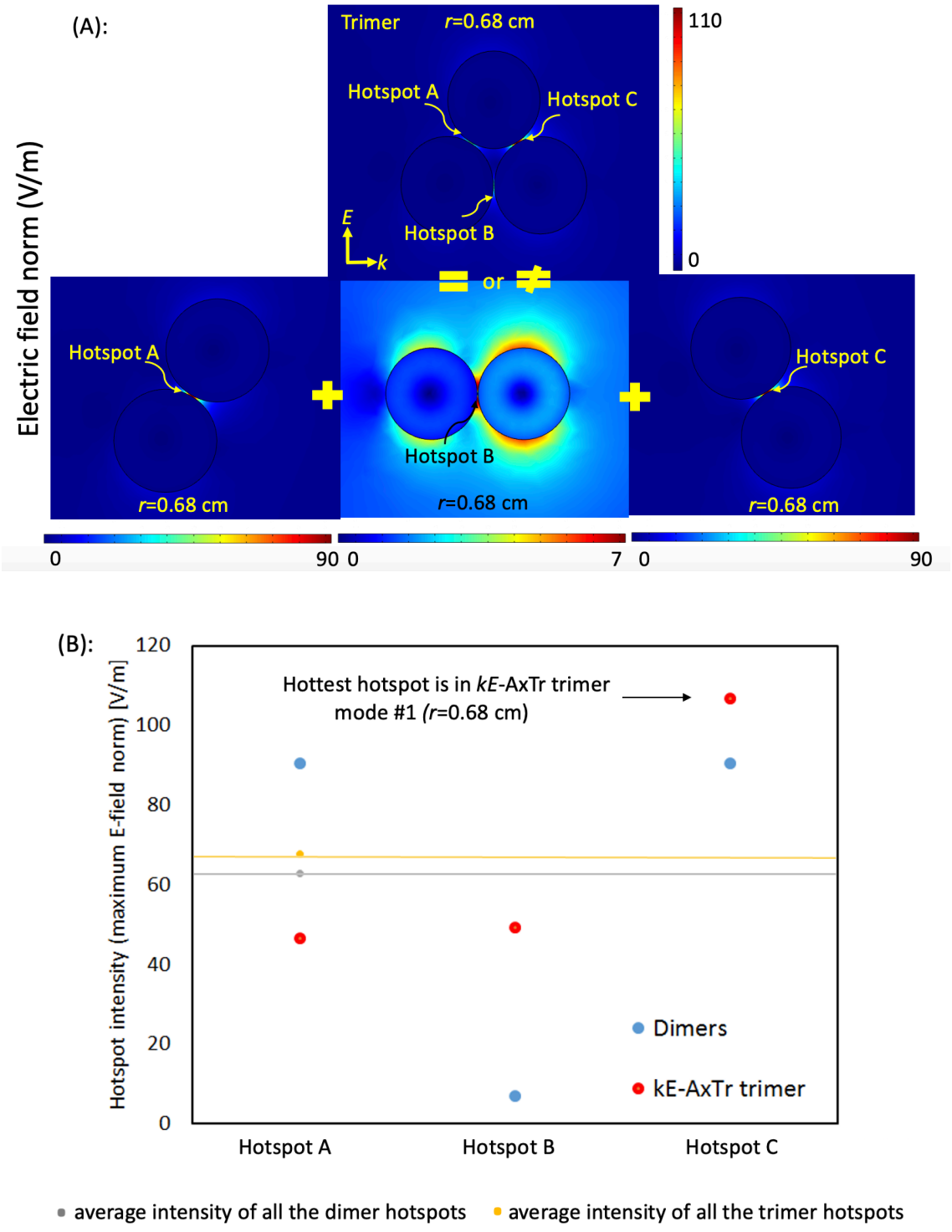

Figure 4.30. (A): Simulated electric field norm maps for the trimer and the individual dimers in isolation, showcasing the first mode at r=0.68 cm. (B): A graphical representation of hotspot intensity, depicted by the maximum electric field norm, comparing the trimer's hotspots with those of the isolated dimers.

In Fig. 4.30, an analysis is conducted on a specific trimer referred to as the *kE*-AxTr trimer, which includes the AxTr dimer within its structure. The focus lies on examining the trimer hotspots at the first mode/resonance, precisely at r=0.68 cm, in comparison to the hotspots of the isolated dimers. The isolated dimers for this trimer consist of two intermediate dimers, namely $TrAx_{30}AxTr_{60}$ and $TrAx_{-30}AxTr_{-60}$, as well as the primary AxTr dimer. It should be noted that the color bar scales vary across the panels, ensuring accurate interpretation of the data. Notably, despite the middle map appearing intensely coloured, it represents the weakest intensity as we can observe in the scale of the color bar for this map. Based on this information, insights can be gained regarding the disparities between the trimer hotspots and those observed in the isolated dimers in terms of intensity. Furthermore, while the average intensity of the trimer hotspots closely aligns with that of the isolated dimer hotspots, the hottest axial hotspot at the first mode belongs to the trimer itself, (Hotspot C). Notably, Hotspot B is most changed as it is more than 5X as strong in the trimer as the dimer. However, not all hotspots are boosted in the trimer. In fact, Hotspot A is about half as intense in the trimer.

4-D-1) Trimer orientation

A question explored in this study is whether the magnitude or strength of hotspots in various trimer models can be predicted based on the combined isolated dimers or other trimers. Additionally, it investigates whether trimers exhibit a consistent trend in terms of the presence and intensity of hotspots.

As an example of different trimer models, we can explore two trimer models on the *k*-*E* plane; trimer model 1 and trimer model 2 (although trimers can also be created on other primary planes such as *k*-*H* or *E*-*H*). Trimer model 1 is composed of three dimers,

$TrAx_{30}AxTr_{60}$, AxTr, and $TrAx_{-30}AxTr_{-60}$, while trimer model 2 consists of a different combination of three dimers, TrAx, $TrAx_{60}AxTr_{30}$, and $TrAx_{-60}AxTr_{-30}$. The purpose of this comparison is to assess the differences between trimers on various planes and with different dimer combinations. In Fig. 4.31, I present these two trimer models on the *k*-*E* plane, referring to them as the *kE*-AxTr trimer and *kE*-TrAx trimer due to the presence of the AxTr dimer and TrAx dimer within their structures.

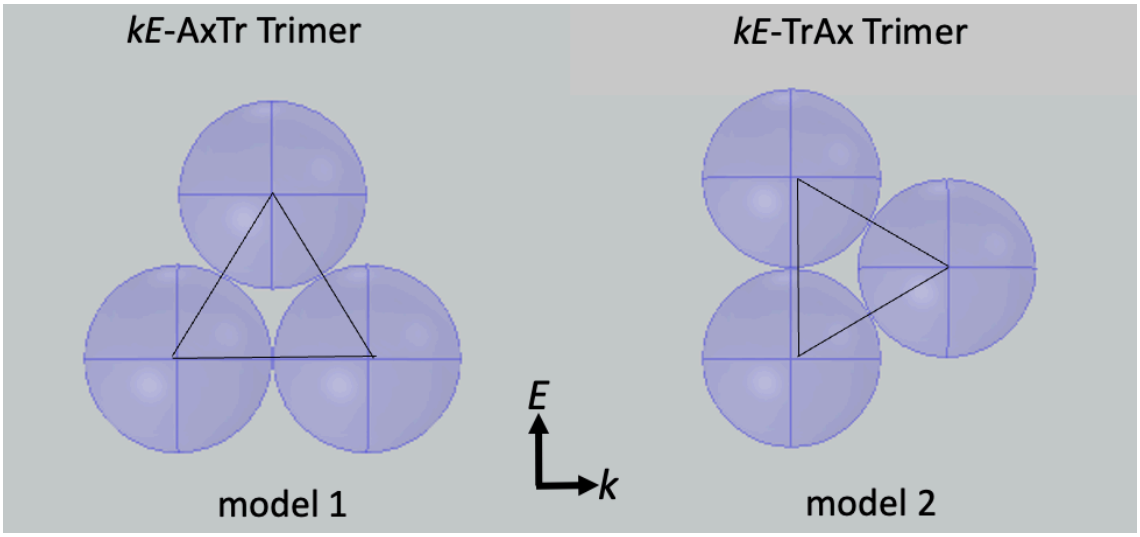

Figure 4.31. Two trimer orientations in the *k*-*E* plane; Trimer model 1 (*kE*-AxTr trimer) featuring an AxTr dimer, and trimer model 2 (*kE*-TrAx trimer) featuring a TrAx dimer.

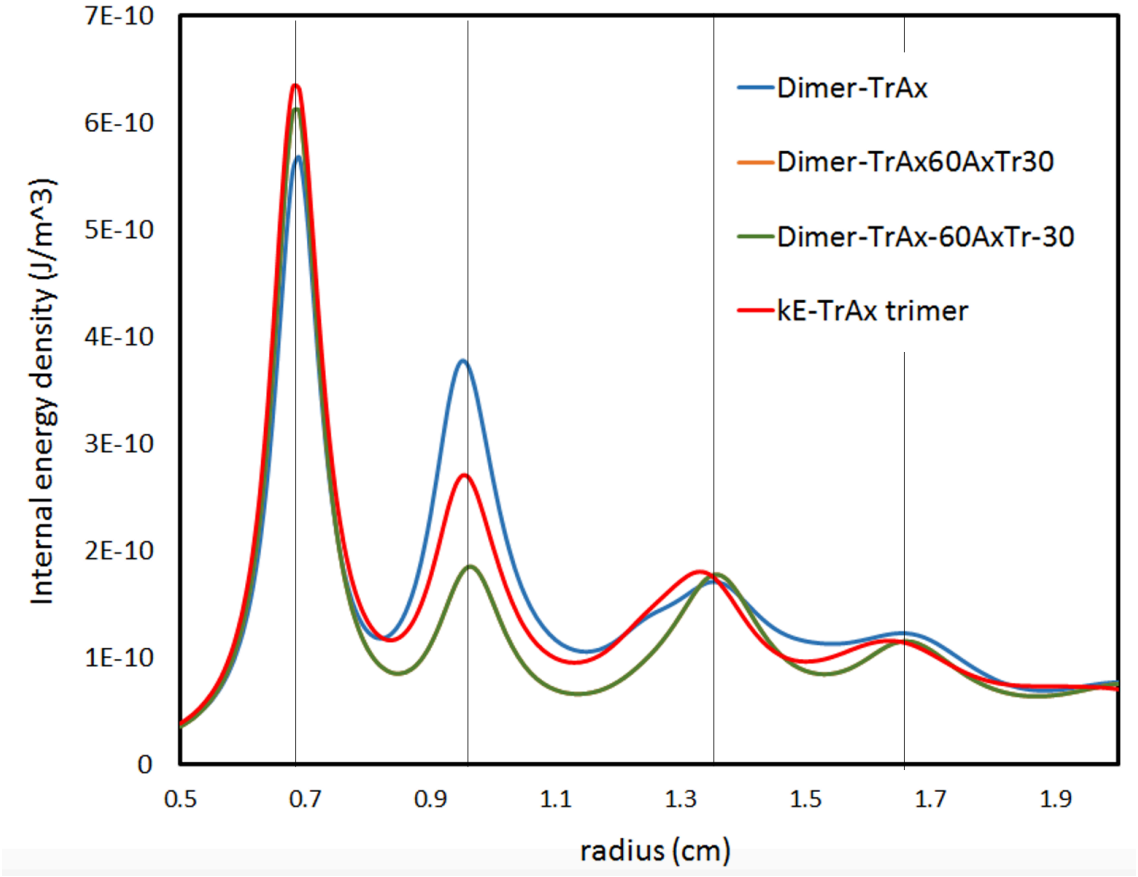

Figure 4.32. Comparison of the EM energy density spectrum between the *kE*-TrAx trimer and its constituent isolated dimers.

The spectrum depicted in Fig. 4.32 illustrates the internal resonances within this particular trimer model. The vertical lines denote the first four resonances at sizes r=0.68, 0.94-0.96, 1.32-1.34, and 1.64-1.65 cm, respectively. Like the observations in the *kE*-AxTr trimer, as shown in Fig. 4.27, the resonances occur at the same sizes in *kE*-TrAx trimer. However, there are slight shifts in energy observed in the trimer compared to its isolated dimers. For instance, at the second resonance, the trimer and one of the dimers exhibit the size of 0.94 cm, while the intermediate dimers show a size of 0.96 cm. Additionally, energy shifts are observed for the trimer compared to its constituent dimers at the third and fourth modes.

Figure 4.33 provides a comparison of the presence, location, and strength of hotspots in the TrAx trimer model across its first four modes.

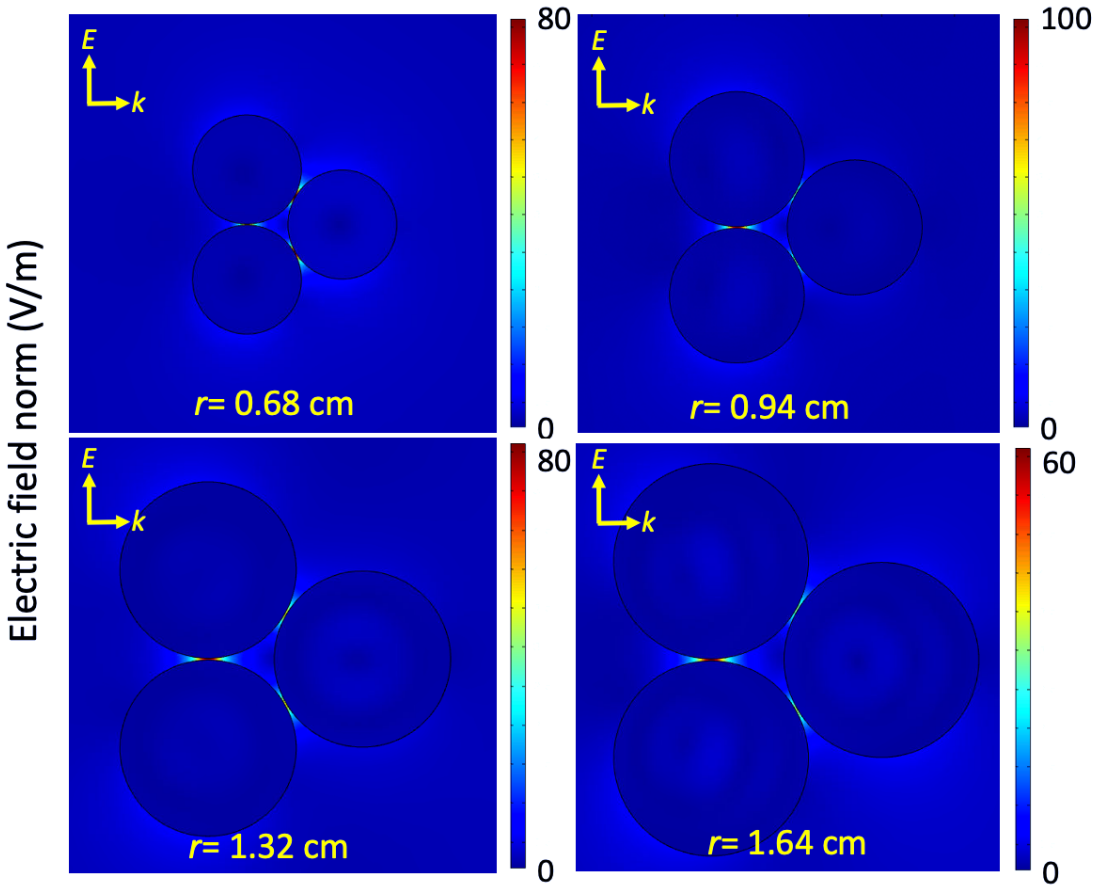

Figure 4.33. Electric field norm maps for the TrAx trimer on the *k*-*E* plane at the first four resonances, illustrating the distribution and intensity of trimer hotspots at each resonance.

Based on the observation of Fig. 4.33, it can be concluded that at the first mode, *kE*-TrAx trimer exhibits three strong axial hotspots with almost equal intensity. Notably, the axial hotspot of the TrAx dimer in this trimer is slightly weaker compared to the other two axial

hotspots at the intermediate dimers. This is interesting because if the constituent dimers were in isolation, the hotspot intensity would not follow the same trend as that of the trimer.

At the second mode, this trimer displays one strong hotspot and two medium hotspots. For the second, third, and fourth resonances, the appearance, location, and intensity of the hotspots follow similar trends. However, it is observed that the hotspot intensity decreases from the second resonance to the fourth resonance.

In Fig. 4.34, I examine the *kE*-TrAx trimer at the first mode, alongside the three individual dimers that compose the *kE*-TrAx trimer. I compare the axial hotspots observed within the trimer to the axial hotspots exhibited by the isolated dimers at the primary resonance in terms of presence and intensity.

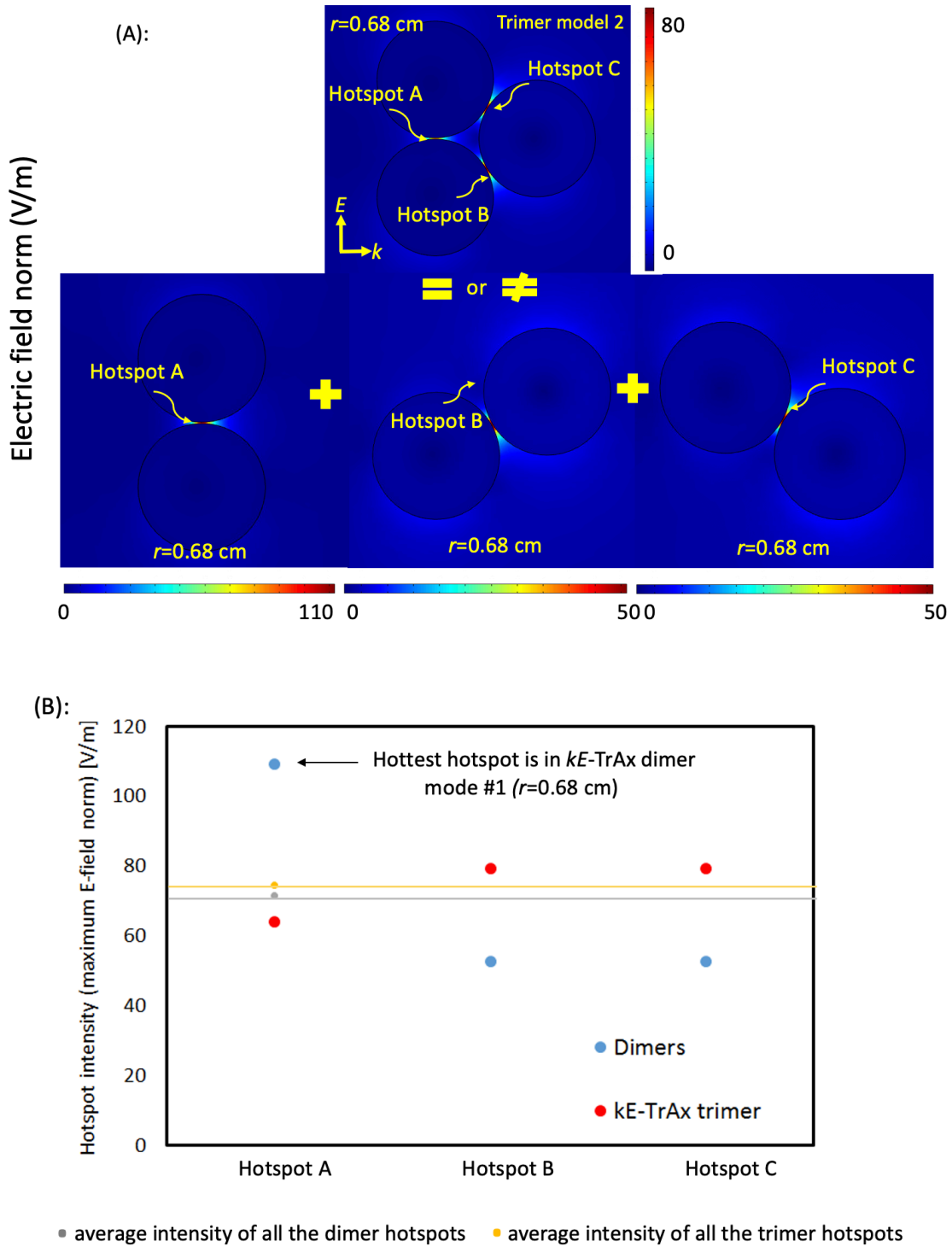

Figure 4.34. (A): Simulated electric field norm maps for Trimer model 2 (*kE*-TrAx trimer) and its combined dimers in isolation at the primary resonance (r=0.68 cm). (B): The hotspot intensity in terms of maximum electric field norm for the trimer hotspots compared to those in the isolated dimers.

The primary focus of this study revolves around analyzing the hotspots' strength in dimers and trimers. I conducted a quantitative investigation to compare the hotspot occurrences in dimers with different orientations, as well as those observed in trimers and the isolated dimers. While evaluating these hotspots, particular emphasis is placed on identifying the hottest hotspot, as it holds significant importance for researchers interested in using dimers and clusters for near-field photonic excitations. In nanoscale experiments, a super-hotspot may prove more valuable than three weaker hotspots.

To assess energy conservation and examine whether hotspots are lost during the transition from dimers to trimers, I calculated the average intensity of all hotspots in this trimer model and its isolated dimers, as depicted in Fig. 4.34. The results indicate that near-field energy is nearly conserved, as the average intensity of all hotspots in a trimer closely matches the average intensity of all hotspots in the constituent isolated dimers. It is worth noting that although the distribution of hotspot intensity may differ between a trimer and its isolated dimers, the overall energy conservation is essentially maintained. As a result, trimers could potentially offer a more convenient and practical material platform for sensing applications, as they may not require as precise orientational alignment as dimers do.

Here, it is important to note that a trimer is not strictly a non-interacting set of dimers, as we observe some evidence of interaction, resulting in hotspots that differ from those of the dimers in isolation. However, despite these differences, the average values of dimer/trimer hotspot energy remain very similar. This suggests of the conserved near-field energy when a trimer is composed of three dimers. This conservation of energy underscores the cohesive nature of the trimer system.

4-D-2) Mode twisting in trimers

The investigation and discussion of mode twisting in dimers is important because it can provide strong evidence of monomer interaction when they combine to form dimers. Likewise, the observed twisting of dimer internal modes differs between dimers in isolation and within a trimer as depicted in Fig. 4.35. This indicates that dimers also interact when they come together to form a trimer. Consequently, it supports the notion that trimers are not merely a straightforward combination of three dimers, just as dimers are not a simple sum of monomers.

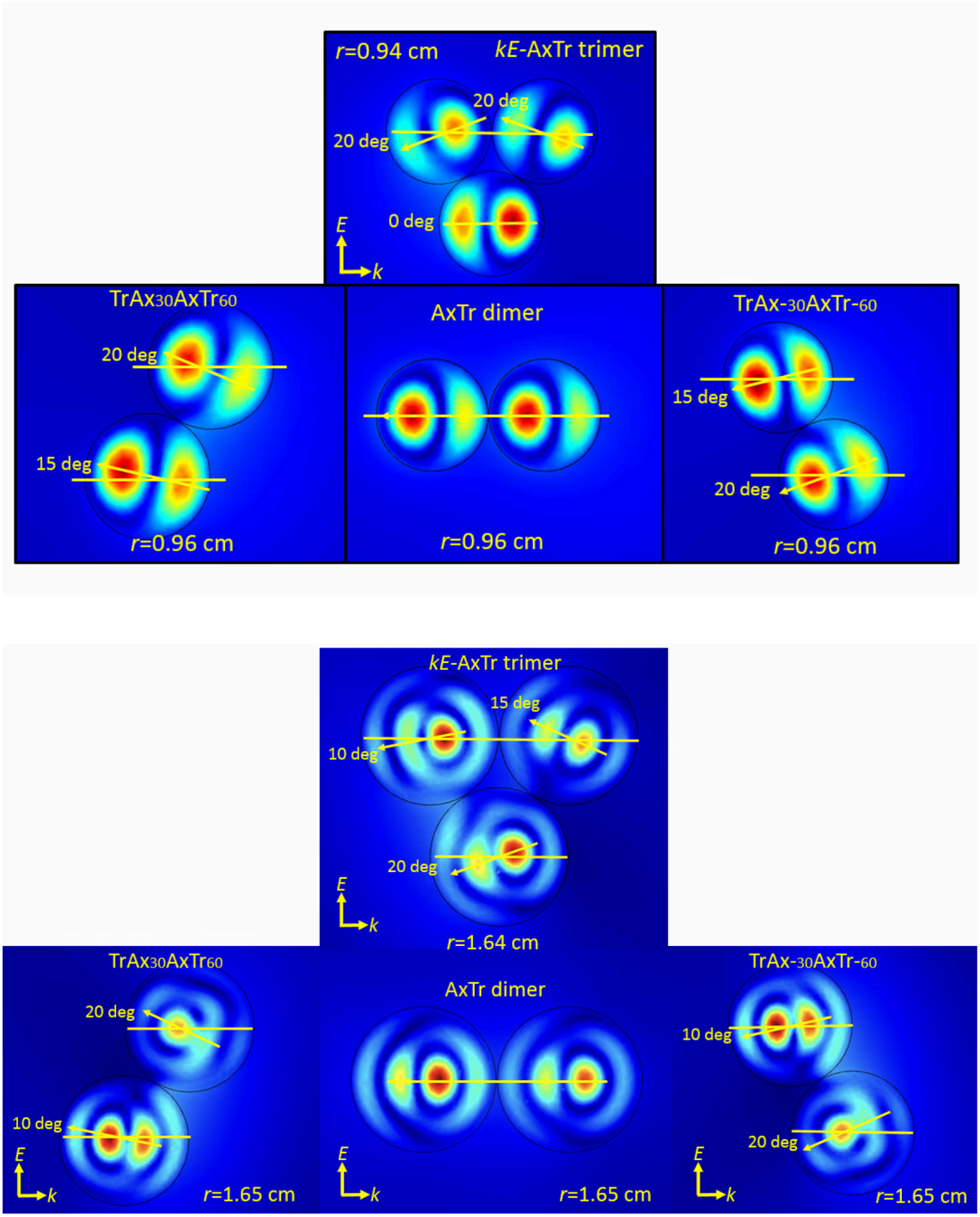

Figure 4.35. Internal mode shape and twisting in the *kE*-AxTr trimer and its constituent isolated dimers at the second and fourth modes. Notably, the mode within the trimer exhibits a distinct twisting pattern, differing from that observed in the individual dimers. (These **magnetic** field maps are scaled the same, and the angles of twisting are indicated on each sphere.)

Overall, Dimers exhibit evidence of monomer interaction through the formation of dimer hotspots and twisting of internal mode shapes. However, trimer hotspots can nearly be explained as the addition of three isolated dimers, with minimal evidence of interaction between dimer groups. Therefore, the significance of internal mode twisting becomes more pronounced for trimers compared to dimers. It demonstrates the interaction of modes, as they undergo deformation and modification when dimers combine to form trimers. While this finding might not have immediate technological applications, it serves as important evidence that dimers communicate and influence each other in a cluster geometry. Therefore, it is crucial to accurately identify, measure, and explain internal mode twisting in differently oriented dimers and trimers.

Chapter 5: Summary

In this thesis I have investigated morphology-dependent resonances (MDRs) in aqueous beads at microwave frequencies. These beads comprised isolated water spheres in different geometries, such as monomers, dimers, and trimer clusters. The study used COMSOL Multiphysics for finite element method (FEM) simulations to explore the behavior of these structures. The simulations focused on various geometries, starting with a single sphere ("monomer") and then investigating dimer configurations with different orientations. Additionally, intermediate dimer orientations and trimer configurations were explored. All objects were simulated as water spheres in a simulation box filled with air and with fully absorbing boundary conditions to eliminate reflections and simulate free-space irradiation. By sweeping the water bead radius at a fixed frequency of 2.45 GHz, resonant sizes and other relevant phenomena such as internal energy densities over a range of bead sizes were studied.

Due to the high refractive index and size of the water beads, standing waves form within the spheres, leading to resonant modes. The first four resonant sizes for monomers are found to occur at approximate bead diameters of 1.4, 1.9, 2.7, and 3.3 cm, respectively. The simulated EM field norm maps reveal that these resonant modes demonstrate well-known MDR resonances, with the lowest-order mode functioning as a magnetic-dipolar mode, displaying a nearly spherical symmetric distribution of magnetic field and a doughnut-shaped electric field concentration. Depending on the observation plane, the electric energy distribution for the first mode appears either as a doughnut shape or as two lobes. The next three resonant modes exhibit distinct distributions of electric and magnetic

fields, representing electric dipole, magnetic quadrupole, and electric quadrupole-like modes.

This research primarily aimed to compare microwave resonances in dimer geometries to those in monomers. Dimer configurations showed significantly larger field concentrations, creating a new resonant feature called the dimer axial hotspot. This hotspot indicates an interference between monomers, leading to a combined effect greater than their individual contributions distinguishing dimers from standard spherical resonators.

In the three primary dimer geometries, most resonances were found at the same or very close sizes as isolated monomer resonances. Comparing the internal resonances of the dimer orientations with those of monomers revealed that the TrTr dimer showed a slightly different resonant size/frequency at the first mode, occurring at smaller sizes than in the monomer. The electric-dipole-like mode (second resonance) was significantly more resonant in the TrAx dimer than in the monomer, with resonant size shifts occurring at the second mode for the TrAx dimer. Additionally, the AxTr dimer displayed increased internal energy density at the third mode compared to its second mode. This study explored dimer hotspots at the first four resonances for three orientations. Notably, magnetic-field axial hotspots were absent for all dimer orientations and resonances, except for the TrTr dimer which showed a small magnetic axial hotspot at the first resonance. The TrAx dimer exhibited the most prominent electric axial hotspots at all four resonances, while the AxTr dimer showed relatively weak electric axial hotspots at first, third and fourth resonances, and the TrTr dimer had no axial hotspots within the first four resonances.

A main research question was whether the three fundamental dimer orientations could serve as a basis set for intermediate orientations. Understanding this is crucial as it allows

us to explore trimers as superstructures composed of dimers, some of which are not oriented at a fundamental geometry. The three fundamental dimers showed variations in their dimerization, motivating the study of intermediate orientations as a superposition of fundamental dimers. I systematically examined the transitions from TrAx dimer to AxTr dimer, TrAx dimer to TrTr dimer, and from AxTr dimer to TrTr dimer. During these transitions, hotspot intensity analysis for all four modes revealed smooth and monotonic trends. Notably, all seven orientations that were defined for the transition of TrAx to AxTr displayed a peak of hotspot intensity at their second modes, with TrAx dimers exhibiting the highest hotspot intensity across all modes. The hotspot behavior during the transitions from TrAx to TrTr and AxTr to TrTr demonstrated similar trends, while hotspot intensity rapidly and differently disappeared during the AxTr to TrTr transition. These findings consistently demonstrate both that **dimer hotspots strongly depend on orientation**, and that transitions between fundamental dimer orientations are smooth and monotonic in terms of hotspot intensity.

To explore potential interactions between dimers within a trimer, we compared the internal mode shapes and orientations. Systematically rotating a dimer from one primary orientation to another resulted in a corresponding rotation (or distortion) of the field concentration inside the dimer. However, at certain intermediate orientations, I observed Internal mode twisting that means the internal mode either ceased to rotate or exhibited a different angle of rotation compared to the dimer's axial angle. Twisted internal modes indicates distinct interactions between water beads in different dimer configurations. Additionally, when the dimer axis was not perpendicular to the propagating direction, the field concentration within the dimer became asymmetric, resulting in stronger fields inside

one sphere compared to the other sphere of the dimer. This is attributed to absorption in the direction of propagation.

The investigation then moved on to trimer configurations, comprising three interconnected dimers. I explored various trimer models and examined hotspot intensity and appearance in trimers compared to dimers. While axial dimer hotspots were found at certain orientations such as TrAx and AxTr, **no new hotspots were identified at the trimer nexus.** Trimers' energy density spectrum showed slight variations compared to their isolated dimers, indicating subtle interactions between dimers within trimer structures. However, a linear combination of resonances in isolated dimers effectively approximated the *kE*-AxTr trimer's energy density spectrum, suggesting very little interference between the dimers. In this manner trimers are different than dimers: Whereas dimers show a distinct feature compared to isolated spheres—namely, the axial hotspot—no new feature is observed in the trimers that doesn't exist in the dimers.

The comprehensive analysis of a trimer characteristics involved investigating the three individual dimer groups within it and comparing their hotspots with those present in the trimer. My findings showed while the distribution of hotspot intensity differed between trimers and isolated dimers, overall energy conservation was maintained. This suggests that trimers could be a practical material platform for sensing applications, as they may not require as precise orientation as dimers do. In analyzing hotspot strengths in dimers and trimers, a particular emphasis was put on identifying the hottest hotspot. In the *kE*-AxTr trimer, the hottest hotspot was found within the trimer at the first mode, surpassing the hotspot intensity of its isolated dimers. However, in the *kE*-TrAx trimer, the hottest hotspot

did not appear in the trimer at the first mode when compared to the hotspot intensity of its constituent dimers.

In summary, dimers exhibited evidence of monomer interaction through the formation of hotspots and twisting of internal mode shapes. However, trimer hotspots can largely be explained as a combination of isolated dimer hotspots, with minimal evidence of interaction between dimer groups. Nonetheless, internal mode twisting was more pronounced for trimers compared to dimers, suggesting some subtle interactions between dimers within a trimer.

Overall, this research provided valuable insights into the behavior of morphology-dependent resonances in aqueous dimers and trimers at microwave frequencies. The study contributes to the understanding of near-field excitations for the water beads in the microwave regime and the potential applications of these structures in various fields. The investigation of dimer and trimer geometries sheds light on the behavior of these structures, and the results open up possibilities for future applications in sensing and other relevant fields.

Future directions

In our experimental research, we have primarily focused on working within the constraints of a microwave oven, limiting our ability to control polarization. However, to further enrich the scope of our investigations and validate the simulation work presented in this thesis, we recognize the need to explore alternative experimental approaches. One crucial future direction that merits exploration is the transition to free-space irradiation with controlled polarization.

Despite its significance, we acknowledge that the move to free-space excitation should not dominate the entirety of our future research considerations. In this section, l outline various avenues for further investigation that extend beyond the limitations imposed by the microwave oven. One of the key aspects that can be explored is the study of various cluster geometries. This investigation will help identify the most practical platform for applications such as sensing, which may require less precise orientation yet offer higher hotspot intensities. By examining a range of cluster configurations, we can gain valuable insights into the interplay between geometry, polarization, and hotspot properties. Additionally, we plan to conduct larger cluster simulations to investigate their collective behavior and properties. This will provide a more comprehensive understanding of cluster dynamics and how they differ from isolated monomers.

Another crucial direction for future research is the investigation of the dimerization process. This entails analyzing the gap energy as a function of bead proximity and quantifying the axial hotspot variation with gap distance. Understanding the transition from isolated monomers to interacting monomers and eventually forming a dimer will shed light on the dynamic behavior of clusters under different conditions.

Finally, expanding our modeling efforts to include temperature dynamics of the resonances will be another valuable avenue for research. Building upon the already identified temperature dependence in our introduction, this direction will allow us to explore questions of resonance stability and runaway processes. Perhaps some resonances are more likely to be observed in practice because the internal field mode is ‘self-healing’ as the refractive and absorptive properties of the dielectric change in response to localized heating.

References

[1] H. K. Khattak, P. Bianucci, and A. D. Slepkov, "Linking plasma formation in grapes to microwave resonances of aqueous dimers," *Proc Natl Acad Sci U S A*, vol. 116, no. 10, pp. 4000–4005, Mar. 2019, doi: 10.1073/PNAS.1818350116/SUPPL_FILE/PNAS.1818350116.SM05.MP4.

[2] D. K. Cheng, and S. Juan, "*Field and Wave Electromagnetics*," Second Edition, (Addison Wesley, 1989).

[3] A. Devilez, X. Zambrana-Puyalto, B. Stout, and N. Bonod, "Mimicking localized surface plasmons with dielectric particles," *Phys Rev B Condens Matter Mater Phys*, vol. 92, no. 24, Dec. 2015, doi: 10.1103/PHYSREVB.92.241412.

[4] S. Lal, S. Link, and N. J. Halas, "Nano-optics from sensing to waveguiding," *Nat Photonics*, vol. 1, no. 11, pp. 641–648, Nov. 2007, doi: 10.1038/NPHOTON.2007.223.

[5] S. D. Gittard and R. J. Narayan, "Laser direct writing of micro- and nano-scale medical devices," *Expert Rev Med Devices*, vol. 7, no. 3, pp. 343–356, May. 2010, doi: 10.1586/ERD.10.14.

[6] S. Nie and S. R. Emory, "Probing single molecules and single nanoparticles by surface-enhanced Raman scattering," *Science (1979)*, vol. 275, no. 5303, pp. 1102–1106, Feb. 1997, doi: 10.1126/SCIENCE.275.5303.1102.

[7] E. Betzig, G. H. Patterson, R. Sougrat, O. W. Lindwasser, S. Olenych, J. S. Bonifacino, M. W. Davidson, J. Lippincott-Schwartz, and H. F. Hess, "Imaging

intracellular fluorescent proteins at nanometer resolution," *Science (1979)*, vol. 313, no. 5793, pp. 1642–1645, Sep. 2006, doi: 10.1126/SCIENCE.1127344.

[8] S. W. Hell, and J. Wichmann, "Breaking the diffraction resolution limit by stimulated emission: stimulated-emission-depletion fluorescence microscopy.," *Optics letters*, 1994.

[9] C. Bohren and D. Huffman, "Absorption and scattering of light by small particles.," *John Wiley & Sons*, 2008.

[10] M. Kerker, "The scattering of light and other electromagnetic radiation.," *Elsevier*, 2016.

[11] U. Kaatze and V. Uhlendorf, "The dielectric properties of water at microwave frequencies," *Zeitschrift fur Physikalische Chemie*, vol. 126, no. 2, pp. 151–165, Feb. 1981, doi: 10.1524/ZPCH.1981.126.2.151/HTML.

[12] Y. A. Gezahegn, J. Tang, S. S. Sablani, P. D. Pedrow, Y. K. Hong, H. Lin, and Z. Tang, "Dielectric properties of water relevant to microwave assisted thermal pasteurization and sterilization of packaged foods," *Innovative Food Science and Emerging Technologies*, vol. 74, Dec. 2021, doi: 10.1016/j.ifset.2021.102837.

[13] M. Vollmer, "Physics of the microwave oven," *Phys Educ*, vol. 39, no. 1, pp. 74–81, Jan. 2004, doi: 10.1088/0031-9120/39/1/006.

[14] E. Palik, "Handbook of optical constants of solids.," *Academic press*, vol. 3, 1998.

[15] J. D. Joannopoulos, S. G. Johnson, J. N. Winn, and R. D. Meade, "*Photonic crystals: Molding the flow of light*," Second edition, physics.mit.edu, (*Princeton Univ Pr*., 2008).

[16] A. Catenaccio, Y. Daruich, and C. Magallanes, "Temperature dependence of the permittivity of water," *Chem Phys Lett*, vol. 367, no. 5–6, pp. 669–671, Jan. 2003, doi: 10.1016/S0009-2614(02)01735-9.

[17] C. Matzler and U. Wegmuller, "Dielectric properties of freshwater ice at microwave frequencies," *Journal of Physics D: Applied Physics*, Dec.1987.

[18] R. Pethig, "Dielectric Properties of Biological Materials: Biophysical and Medical Applications," *IEEE Transactions on Electrical Insulation*, no. 5, Oct. 1984.

[19] Z. F. Meng, Z. Tao, J. F. Ruan, R. Z. Zou, and S. W. Ji, "Broadband-absorption mechanism in a water-based metamaterial absorber," *Physics Letters, Section A: General, Atomic and Solid-State Physics*, vol. 445, Sep. 2022, doi: 10.1016/J.PHYSLETA.2022.128269.

[20] Y. Yin, M. Zeng, J. Liu, W. Tang, H. Dong, R. Xia, and R. Yu, "Enhanced high-frequency absorption of anisotropic Fe3O4/graphene nanocomposites," *Sci Rep*, vol. 6, no. 1, May. 2016, doi: 10.1038/srep25075.

[21] S. C. Hill and R. E. Benner, "Morphology-Dependent Resonances," *Scientific reports* 6, no. 1. pp. 1–61, Mar. 1988, doi: 10.1142/9789814415804_0001.

[22] D. Morrish, "Morphology dependent resonance of a microsphere and its application in near field scanning optical microscopy," *PhD diss., PhD Thesis, Faculty of Engineering and Industrial Science, Swinburne University of Technology*, 2005.

[23] J. Eversole, H. Lin, A. Huston, A. J. Campillo, P. T. Leung, and K. Young, "High-precision identification of morphology-dependent resonances in optical processes in microdroplets," *JOSA B* 10, no. 10, Oct. 1993.

[24] G. Adamovsky and M. V. Ötügen, "Morphology-dependent resonances and their applications to sensing in aerospace environments," *Journal of Aerospace Computing, Information and Communication*, vol. 5, no. 10, pp. 409–424, Oct. 2008, doi: 10.2514/1.35775.

[25] B. Vennes and T. C. Preston, "Morphology-dependent resonances in homogeneous and core-shell nonspherical particles," *APSB Vennes, TC Preston Physical Review A, 2021•APS*, vol. 104, no. 3, p. 33512, Sep. 2021, doi: 10.1103/PhysRevA.104.033512.

[26] A. Rahman, R. C. Eze, and S. Kumar, "Novel optical sensor based on morphology-dependent resonances for measuring thermal deformation in microelectromechanical systems devices," *Journal of Micro/Nanolithography, MEMS, and MOEMS*, vol. 8, no. 3, p. 033071, Jul. 2009, doi: 10.1117/1.3222918.

[27] P. G. Kik and M. L. Brongersma, "Surface Plasmon Nanophononics," *Springer*, 2007.

[28] W.L. Barnes, “Surface plasmon–polariton length scales: a route to sub-wavelength optics,” *Journal of optics A: pure and applied optics*, Mar. 2006, doi: 10.1088/1464-4258/8/4/S06.

[29] M. I. Mishchenko and A. Lacis., “Morphology-dependent resonances of nearly spherical particles in random orientation,” *Applied Optics* 42, no. 27. Sep. 2003.

[30] A. Taflove and S. C. Hagness, “Computational electrodynamics: The finite-difference time-domain method,” in *The Electrical Engineering Handbook*, 3rd ed. *13*, pp.199-315. Jan. 2005. doi: 10.1016/S1570-8659(04)13003-2

[31] J. Jianming, “*The finite element method in electromagnetics.,”* (John Wiley & Sons, Feb. 2015).

[32] S. A. Maier, “*Plasmonics: Fundamentals and applications*.,” *Springer*, Vol. 1, p. 245 New York, May. 2007. doi: 10.1007/0-387-37825-1.

[33] Z. Zheng, A. Bindra, H. Jin, Q. Sun, and S. Liu, “Morphology-dependent resonance enhanced nonlinear photoacoustic effect in nanoparticle suspension: a temporal-spatial model,” *Biomed Opt Express* 12, no. 12. pp.7280-7296. Dec. 2021.

[34] E. Hao and G. C. Schatz, “Electromagnetic fields around silver nanoparticles and dimers.,” *J Chem Phys* 120, no. 1. pp.357-366. Jan. 2004.

[35] J. A. Schuller, E. S. Barnard, W. Cai, Y. C. Jun, J. S. White, and M. L. Brongersma, “Plasmonics for extreme light concentration and manipulation,” *Nature Materials*, vol. 9, no. 3. Nature Publishing Group, pp. 193–204, Mar. 2010. doi: 10.1038/nmat2630.

[36] L. Shen, Q. Ran, and X. Zhang, "Inhibition effects of the applied dielectric on dimer-induced microwave plasma and focused hotspots," *Appl. Phys. Lett.*, 122, no. 22. May. 2023.

[37] M. S. Lin, L. C. Liu, L. R. Barnett, Y. F. Tsai, and K. R. Chu, "On electromagnetic wave ignited sparks in aqueous dimers.," *Phys Plasmas* 28, no. 10, Oct. 2021.

[38] J. N. Anker, W. P. Hall, O. Lyandres, N. C. Shah, J. Zhao, and R. P. Van Duyne, "Biosensing with plasmonic nanosensors.," *Nat Mat* 7, no. 6, pp.442-453. Jun. 2008.

[39] L. Wang, M. Hasanzadeh Kafshgari, and M. Meunier, "Optical Properties and Applications of Plasmonic-Metal Nanoparticles," *Adv Funct Mater*, vol. 30, no. 51, Dec. 2020, doi: 10.1002/ADFM.202005400.

[40] L. Novotny and B. Hecht, "Principles of nano-optics," *Cambridge University Press*, vol. 9780521832243. Sep. 2012. doi: 10.1017/CBO9780511813535.

[41] K. Kneipp, H. Kneipp, I. Itzkan, R. R. Dasari, and M. S. Feld, "Ultrasensitive Chemical Analysis by Raman Spectroscopy," *Chem Rev*, vol. 99, no. 10, pp. 2957–2975, Oct. 1999, doi: 10.1021/CR980133R.

[42] M. W. Knight, Y. Wu, J. B. Lassiter, P. Nordlander, and N. J. Halas, "Substrates matter: influence of an adjacent dielectric on an individual plasmonic nanoparticle," *Nano Lett*, vol. 9, no. 5, pp. 2188–2192, May. 2009, doi: 10.1021/NL900945Q/ASSET/IMAGES/LARGE/NL-2009-00945Q_0003.JPEG.

[43] R. F. Oulton, V. J. Sorger, T. Zentgraf, R. M. Ma, C. Gladden, L. Dai, G. Bartal, and X. Zhang, "Plasmon lasers at deep subwavelength scale," *Nature* 461, no. 7264, Oct. 2009, doi: 10.1038/nature08364.

[44] H. A. Atwater and A. Polman, "Plasmonics for improved photovoltaic devices," *Nature Publishing Group* 9, no. 3. pp.205-213. Mar. 2010, doi: 10.1038/nmat2629.

[45] K. Catchpole, A. Polman, J. Müller, B. Rech, J. Springer, and M. Vanecek, "Plasmonic solar cells," *Optics Express, Vol. 16, Issue 26, pp. 21793-21800*, vol. 16, no. 26, pp. 21793–21800, Dec. 2008, doi: 10.1364/OE.16.021793.

[46] C. Sönnichsen, B. M. Reinhard, J. Liphardt, and A. P. Alivisatos, "A molecular ruler based on plasmon coupling of single gold and silver nanoparticles.," *Nat Biotechnol*, 23, no. 6. pp.741-745. Jun. 2005.

[47] COMSOL Multiphysics, "The Wave Optics Module User's Guide.," 2018.

[48] D. J. Griffiths, "*Introduction to electrodynamics.,"* 574-574 5th edition , (2005).

[49] F. T. Ulaby, "*Electromagnetics for engineers.*," 8th edition, (Pearson, 2005).

[50] Y. Song, J. Shafe-Purcell, and A. D. Slepkov, "Linking microwave heating of aqueous spheres to morphology-dependent resonances," *AIP Adv*, vol. 12, no. 11, Nov. 2022, doi: 10.1063/5.0122773.